Received XX Month, XXXX; revised XX Month, XXXX; accepted XX Month, XXXX; Date of publication XX Month, XXXX; date of current version XX Month, XXXX.

Digital Object Identifier 10.1109/XXXX. 2022.1234567

A Survey on Wearable Inertial Sensing for Indoor Positioning

Yinqi Zhang, Xu Feng, Zhiyuan Luo, Khuong An Nguyen

[1]Department of Computer Science, Royal Holloway University of London, Surrey, TW20 0EX, United Kingdom

Corresponding author: Yinqi Zhang (E-mail: Yinqi.Zhang.2025@live.rhul.ac.uk).

ABSTRACT Despite two decades of research, ubiquitous infrastructure-free indoor positioning remains a major challenge. In recent years, the emergence of wearable devices equipped with multiple sensors has presented an opportunity to address this problem. However, despite the popularity of wearable inertial positioning research, the field still lacks a comprehensive review that consolidates progress and helps guide further work. Thus, this paper presents the first systematic review of this field, analysing over 120 studies using novel taxonomies. We propose four key analytical perspectives: sensor types, body placement, positioning algorithms, and performance evaluation. We also propose a new taxonomy that categorises positioning algorithms into inertial measurement unit based methods, classical stochastic frameworks, multi-sensor fusion, and Machine Learning techniques. We provide detailed comparisons of the studies across body parts, signal types, IMU types, algorithms, path characteristics, testbed types, 2D/3D dimensions, and error metrics. Our findings reveal that multi-location IMU configurations significantly outperform single-location setups, with upper body and whole body placements achieving the best results. When evaluated using relative pose error to account for differences in trajectory length, ML based methods achieve the lowest per-unit-distance drift, suggesting that their apparent underperformance in some benchmarks is substantially influenced by the longer paths over which they are typically tested. While IMU only systems dominate due to their cost-effectiveness, ultra-wideband (UWB) fusion delivers superior stability and accuracy. Our findings indicate that strategic multi-sensor integration offers the best balance between performance and complexity for real-world deployment.

INDEX TERMS Wearable sensors, inertial measurement unit, indoor positioning, sensor fusion

I. INTRODUCTION

ALTHOUGH Global Positioning System (GPS) provides reliable positioning in open outdoor environments, its signals attenuate rapidly indoors due to walls, floors, and other obstacles [1]. As a result, a wide range of sensor-based indoor positioning systems has been proposed, leveraging technologies such as WiFi [2], [3], Bluetooth Low Energy (BLE) [4], [5], ultra-wideband (UWB) [6]–[8], ultrasonic/acoustic [9], [10], visible light and LED [11], [12], and pressure sensor [13], among others. However, many of these approaches require dense infrastructure, careful calibration, or controlled environments, which limit their scalability and robustness in real-world deployments. In light of these limitations, and driven by the rapid growth of wearable and mobile devices, inertial measurement units (IMU)-based indoor positioning on wearable devices has attracted increasing attention [14]–[16].

In wearable indoor positioning systems, the positioning estimation of the user is performed directly on the user's body or personal device, using IMU sensors that are inherently self-contained and relatively insensitive to environmental changes [17]. Modern IMUs typically include accelerometers, gyroscopes, magnetometers, and sometimes barometers [18]. They provide three-dimensional measurements of specific force and angular velocity, and, when available, three-dimensional magnetic field readings and air pressure, which can be used to estimate altitude [19]. These signals form the basis for estimating position, velocity, and orientation through inertial navigation algorithms, without relying on external infrastructure or being affected by signal blockage and multipath [20], [21]. When embedded in ubiquitous wearable platforms such as smartphones, smartwatches, smartglasses, smart shoes, and dedicated body-worn sensor nodes, wearable inertial indoor positioning enables continuous monitoring across heterogeneous challenging indoor environments [22].

Whilst existing surveys on indoor positioning predominantly examine infrastructure-dependent technologies or pro-

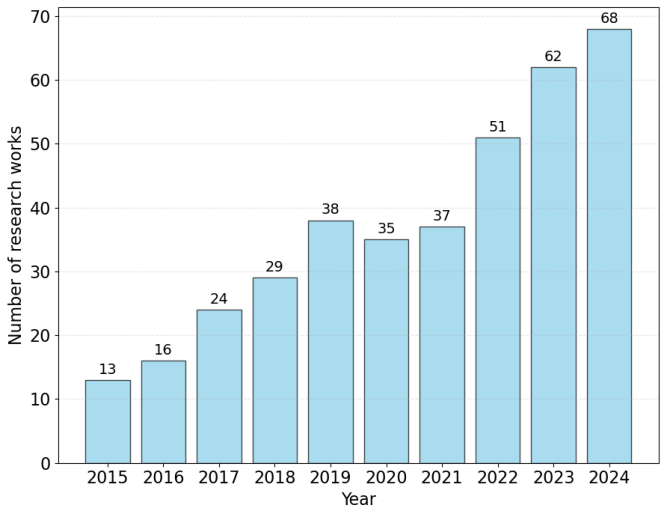

FIGURE 1. The number of research works on wearable inertial navigation for indoor positioning published each year.

vide broad overviews of inertial navigation and pedestrian dead-reckoning, there remains a notable absence of systematic analysis specifically addressing wearable inertial systems for human indoor positioning. Moreover, as the number of studies on positioning methods and wearable sensor placements continues to grow (Figure 1), there is a pressing need for large-scale, structured analyses that compare the advantages, limitations, and relative performance of wearable inertial indoor positioning systems.

To address this gap, this work systematically surveys, categorises, and critically compares over 120 recent publications on wearable inertial navigation for indoor human positioning. It provides comprehensive performance comparisons grounded in an extensive body of studies, identifies the most commonly used on-body sensor locations and IMU types, highlights top-performing indoor positioning approaches, and offers the most thorough performance analysis currently available. In addition, it discusses prevailing trends, unresolved challenges, and future research directions for developing more efficient and robust wearable indoor positioning systems.

In summary, the contributions of this paper are as follows:

- We perform a thorough review of over 120 studies on wearable inertial navigation system for indoor positioning, delivering an extensive survey of the current landscape.
- We propose a unified taxonomy for wearable inertial navigation systems structured based on the indoor positioning algorithm. We distinguish four main categories of methods: purely IMU-based algorithms, classical stochastic estimation frameworks, multi-sensor fusion approaches, and machine learning based positioning methods.
- We categorise wearable device configurations by both their body-worn location and their sensing modalities. For body location, we identify six categories: foot only, hand only, head only, lower body, upper body, and whole body setups. For sensor combinations, we consider five types: IMU only systems; IMU paired with cameras; IMU paired with Bluetooth; IMU paired with WiFi; and IMU paired with other complementary sensors such as UWB, LiDAR, or barometers.
- We provide a systematic comparison of current wearable inertial navigation systems, focusing on several key attributes. In particular, we offer a comprehensive comparison table covering sensor placement, sensor model and origin, path length and type, positioning methods, and performance metrics together with their associated parameters. For attributes not explicitly reported in the original studies, we manually derived, extracted, or collected the missing values, enabling a more complete and comparable overview across studies.
- We systematically assess the performance of state-of-the-art wearable inertial navigation systems, providing an in-depth analysis and structured comparison of wearable inertial indoor positioning methods reported in the literature. The impact of different signal measures, positioning algorithms and body-worn locations are quantitatively investigated.

A. SCOPE

This review aims to provide a comprehensive summary and analysis of current research on wearable inertial navigation for indoor positioning. The goal is to offer valuable and unique insights into the trends and challenges within this field. Our main focus is on research papers that explore indoor positioning methods for wearable inertial navigation, especially studies that investigate different sensor placements and types.

This review focuses specifically on systems that utilise wearable inertial sensing for indoor positioning. We exclude studies that rely solely on wireless infrastructure (WiFi, Bluetooth, UWB) or vision-based methods without IMU integration. However, we include hybrid approaches that combine inertial navigation with complementary sensing modalities, as these represent important developments in addressing the inherent drift limitations of pure inertial systems.

Following the PRISMA guidelines [23], we conducted a systematic review of current studies on wearable inertial indoor positioning systems. A comprehensive search was performed using the Web of Science, Google Scholar, and IEEE Xplore databases. Both journal articles and conference papers were included. The keywords used in all databases were: *“IMU”, “inertial”, “wearable”, “sensor”, “pedestrian”, “navigation”, “localisation”, “positioning” and “indoor”*.

Our inclusion criteria are:

- Peer-reviewed journal articles and conference papers published in English.

- Studies presenting quantitative evaluation of the indoor positioning performance.
- Research aimed at expanding pedestrian wearable IMU datasets or improving the accuracy of wearable inertial navigation for indoor positioning using existing datasets.
- Research employing body-worn, foot-mounted, or hand-held IMU configurations for human testers.
- Research proposing novel algorithms and sensor fusion techniques to demonstrate significant performance improvements.

Our exclusion criteria are:

- Studies focusing exclusively on activity recognition or gait analysis without positioning evaluation.
- Studies involving GPS signals.
- Reviews or non-research publications.
- Studies involving drones that perform positioning using IMU data.

A thorough literature search was carried out on major research platforms using the previously defined keywords, resulting in an initial pool of **1, 130 papers**. Duplicate entries and studies considered outdated or less relevant were first removed. Titles, abstracts, and keywords were then screened to exclude works unrelated to wearable inertial navigation for indoor positioning. Afterward, each remaining paper was manually examined in detail, with particular attention to its technical content, methodological approach, and experimental validation. Following this critical assessment, a total of 124 publications published between March 2015 and May 2025 were retained for detailed analysis.

B. PAPER ORGANISATION

The remainder of this paper is structured as follows: Section II provides a detailed overview of wearable inertial navigation systems, including the fundamental sensors, inertial navigation principles, and the main families of positioning algorithms. It also introduces our taxonomy of sensor configurations and fusion schemes used in wearable systems. Section III presents a comprehensive comparison and performance analysis of the reviewed methods. Finally, Section IV concludes the paper by summarising the key findings, highlighting current limitations in wearable inertial navigation, and outlining promising directions for future research.

II. WEARABLE INERTIAL NAVIGATION

This section first introduces the fundamental sensors integrated within an IMU and outlines the underlying principles of inertial navigation. Subsequently, the 124 collected studies are categorised according to sensor type and positioning algorithm. A detailed discussion is then provided for each category, including specific applications and the corresponding formula derivations.

A. Inertial Measurement Unit (IMU)

Wearable inertial navigation estimates a body position by processing motion data collected from wearable sensors. At the heart of such systems is the IMU sensor, which measures the motion state of the body segment to which it is attached. A typical IMU includes multiple sensing modalities most commonly accelerometers, gyroscopes, magnetometers, and, in some cases, barometers. This section introduces each sensing component of the IMU used in wearable systems, and outlines the basic principles of wearable inertial navigation.

1) Accelerometer

The accelerometer is a key component of the IMU, used to measure an object's linear acceleration in three-dimensional space. Its working principle is based on Newton's second law, which states that force is proportional to acceleration. By detecting the specific force, the accelerometer can determine the acceleration value. It usually outputs a three-dimensional vector representing the acceleration components in the body coordinate system. Mathematically, the measurement can be expressed as a vector $a = [a_x, a_y, a_z]^T$, where a_x, a_y, and a_z represent the acceleration components along the x-, y-, and z-axes, respectively, typically measured in metres per second squared (m/s^2). However, during the measurement process, the accelerometer output is often affected by bias and noise in addition to the actual coordinate changes. Therefore, the measured acceleration value can be modelled as $a^b = a^b_{true} + b_a + \mathcal{N}_{acc}$, where a^b_{true} represents the actual motion value of the IMU in the body frame, b_a is the accelerometer bias, and $\mathcal{N}_{acc}$ represents measurement noise which is often assumed to follow a Gaussian distribution, i. e. , $\mathcal{N}_{acc} \sim (0, \delta^2_{acc})$. According to Newton's second law, the specific force can be expressed as $f^b = a^b - g^b$, where f^b represents the specific force in the body frame and g^b is the gravitational acceleration expressed in the same frame. In practical navigation systems, the orientation of the IMU coordinate system generally differs from the actual navigation frame. Consequently, a rotation matrix R^n_b is needed to convert quantities such as a^b from the body frame into the navigation frame a^n (also known as the real world frame). The acceleration in the navigation frame can be calculated as $a^n = R^n_b(f^b) - g^n$, where g^n is the gravitational acceleration expressed in the navigation frame.

2) Gyroscope

A gyroscope is used to measure the body angular velocity, that is, the rate of its rotational motion. It outputs an angular velocity vector, which is used to calculate changes in the object's orientation. Mathematically, the measurement can be expressed as a vector $\omega = [\omega_x, \omega_y, \omega_z]^T$, where ω_x, ω_y, and ω_z represent the angular velocity components around the x-, y-, and z-axes, respectively. These quantities are typically measured in radians per second (rad/s). By integrating the angular velocity data over time, the system can estimate the

object's attitude angles. However, this integration process accumulates errors and introduces drift, so gyroscopes are often combined with other sensors to improve accuracy. As discussed earlier for the accelerometer, gyroscope measurements are also affected by bias and noise. so the gyroscope measurement can be written as $\omega = \omega_{true} + b_g + \mathcal{N}_{gyr}$, where ω_{true} is the true angular velocity, b_g represents the gyroscope bias, and $\mathcal{N}_{gyr}$ represents the measurement noise, which is commonly assumed to follow a Gaussian distribution, $\mathcal{N}_{gyr} \sim (0, \delta^2_{gyr})$.

There are several ways to compute the rotation matrix $R^n_b(k)$, which represents the transformation between the body frame and the navigation frame at time step k. Common methods include the Euler method, the rotation vector method, and the quaternion-based method. Here, we first introduce the Euler method, where the rotation matrix is updated as

$$R^n_b(k) = R^n_b(k-1) + [\omega(k-1)]_\times R^n_b(k-1)\Delta k \quad (1)$$

where $R^n_b(k)$ is the rotation matrix at the current time step k, $R^n_b(k-1)$ is the rotation matrix at the previous time step, $\omega(k-1)$ is the angular velocity measured by the gyroscope, Δk is the time interval, and $[\cdot]_\times$ denotes the skew-symmetric matrix corresponding to the cross-product operation.

Although the Euler method is simple to implement, it is not numerically stable. Errors and noise from the gyroscope accumulate in the rotation matrix over time, leading to drift. As a result, quaternion-based methods are more commonly used in practical navigation systems. These methods are more accurate but also more computationally complex than the Euler method. At the initial state, a quaternion $q = [q_0, q_1, q_2, q_3]^T$ is constructed from the alignment between the body frame and the navigation frame. When the two frames are aligned, the initial quaternion is $q = [1.0, 0.0, 0.0, 0.0]^T$. Next, the rotation vector $\varphi = \omega \cdot \delta t$ is computed, where ω is the gyroscope output and φ is the rotation vector. Then the quaternion increment is formed as

$$\delta q = \begin{bmatrix} cos(\varphi/2) \\ sin(\varphi/2)\varphi_x/\varphi \\ sin(\varphi/2)\varphi_y/\varphi \\ sin(\varphi/2)\varphi_z/\varphi \end{bmatrix} \quad (2)$$

where φ is the magnitude of the rotation vector, and φ_x, φ_y, φ_z are its components. When the rotation angle is very small, this can be approximated by $\delta q = [1, \varphi_x/2, \varphi_y/2, \varphi_z/2]^T$ The quaternion is then updated through quaternion multiplication $q = q \otimes \delta q$, where $\otimes$ denotes quaternion multiplication. After the update, the quaternion is normalised to ensure it remains a unit quaternion. Finally, the updated quaternion is converted into the rotation matrix R^n_b.

3) Magnetometer

A magnetometer in an IMU is used to measure the intensity of the Earth's magnetic field, providing crucial directional information, especially for determining the heading angle. It operates based on the Hall effect or magneto-motive principles, detecting the magnetic field components in three-dimensional space. The magnetometer outputs a magnetic field vector, which can be used to calculate the orientation relative to magnetic north. Mathematically, the measurement can be expressed as $B = [B_x, B_y, B_z]^T$, where B_x, B_y, and B_z represent the magnetic field components along the x-, y-, and z-axes, respectively. These quantities are usually measured in tesla (T) or gauss (G). In practical navigation systems, the magnetometer is rarely used alone; instead it is commonly fused with the gyroscope data to correct the heading estimates. When the gyroscope drift occurs due to accumulated noise, the magnetometer provides an absolute reference to compensate for this error.

4) Barometer

A barometer estimates changes in height by measuring air pressure. The basic idea is that air pressure decreases in a predictable way as altitude increases. Within the IMU, the barometer provides continuous relative altitude information and is widely used for height tracking in wearable inertial navigation systems. The operation of a barometer mainly includes the following steps. First, it measures the ambient air pressure at its current location in real time. Then, a standard atmospheric model, which describes how pressure and temperature change with altitude under ideal conditions, is applied. By comparing the measured pressure with the model's predicted value, the system computes the corresponding altitude. Variations in this estimated altitude can help the accelerometer and gyroscope correct the position estimate, leading to a more accurate navigation result. However, several factors can affect the barometer's altitude accuracy. Changes in environmental conditions such as temperature, humidity, and short-term pressure fluctuations may introduce errors. In addition, limitations in sensor precision and the absence of regular calibration can further reduce the reliability of the altitude measurements.

TABLE 1. IMU Degrees of Freedom (DoF) and Corresponding Sensor Sets.

Degree of Freedom	Sensors Included
3DoF IMU	Gyroscope / Accelerometer / Magnetometer
6 DoF IMU	Accelerometer Gyroscope
9 DoF IMU	Accelerometer Gyroscope Magnetometer
10 DoF IMU	Accelerometer Gyroscope Magnetometer Barometer

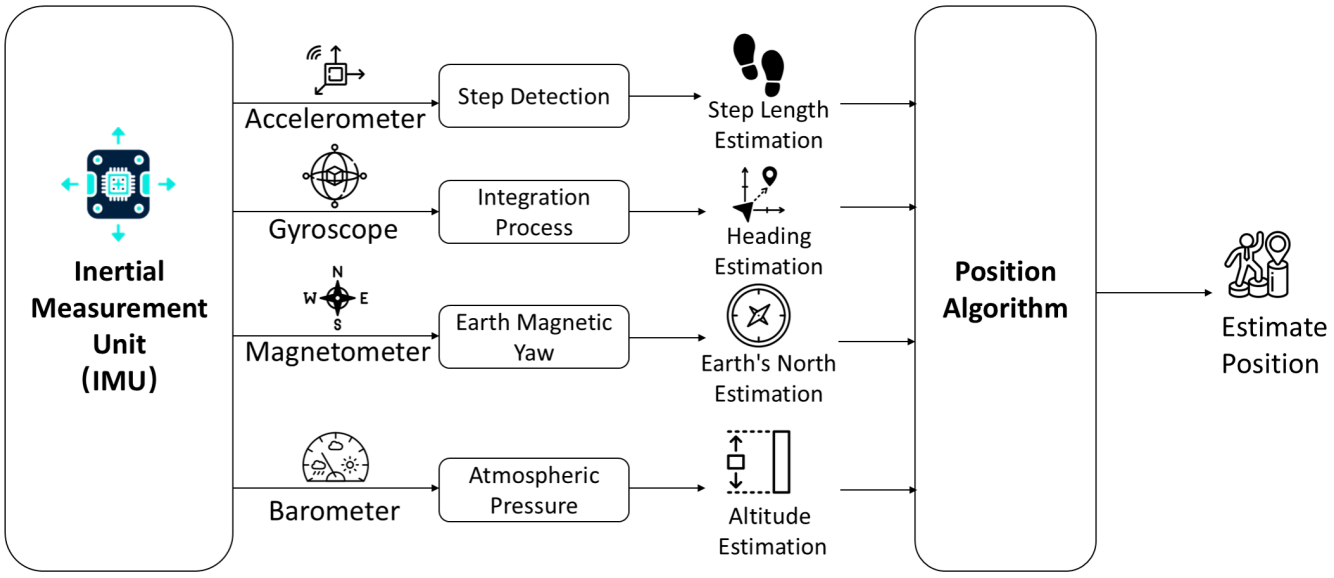

FIGURE 2. A processing diagram of the indoor positioning algorithm based on a 10 DoF IMU. The system fuses data from multiple sensors: the accelerometer captures dynamic motion and gait features; the gyroscope measures angular velocity to track orientation changes; the magnetometer provides geomagnetic field measurements to support heading estimation and magnetic declination compensation for a more accurate yaw angle; and the barometer estimates relative altitude by detecting changes in atmospheric pressure.

5) Degree of Freedom

The degree of freedom (DoF) refers to the number of independent parameters that a system can measure. A wide range of IMU sensors is available on the market, with DoF values typically ranging from 3 to 9 [18], [24], though more recent developments have extended this range to 10 DoF configurations. The specific DoF of an IMU depends on both the types of sensing elements it includes and the number of measurement axes provided by each sensor.

A 3-axis IMU usually contains only a three-axis gyroscope, which measures the carrier's rotational motion and enables estimation of the three attitude angles: roll, pitch, and yaw corresponding to three degrees of freedom. A 6 DoF IMU builds on this by adding a three-axis accelerometer, enabling it to detect linear accelerations along three additional axes, in addition to attitude estimation. Further expanding on this, a 9 DoF IMU adds a three-axis magnetometer to the 6 DoF configuration. Since the gyroscope only measures relative changes in orientation, integrating a magnetometer allows the IMU to obtain absolute attitude information with respect to the Earth's magnetic field. Although a 9 DoF IMU can provide relatively accurate pose estimation, vertical motion can still lead to errors, as gyroscopes and magnetometers are less effective in measuring altitude changes. To address this limitation, a single-axis barometer may be integrated with a 9 DoF IMU, yielding a 10 DoF configuration that significantly enhances vertical positioning accuracy through barometric pressure measurements.

In wearable inertial navigation, most studies employ either a 6 DoF IMU or a 9 DoF IMU (as shown in Figure 9), where the degrees of freedom correspond to the measurements captured along the x-, y-, and z- axes by each sensor (Table 1). A higher DoF configuration provides a richer information set by incorporating additional sensor modalities, thereby enabling the development of more sophisticated navigation systems capable of addressing complex motion patterns and environmental conditions.

B. Wearable sensing indoor positioning systems

To systematically categorise the included studies, the 124 papers were divided into five groups based on the combinations of wearable sensors used: IMU only, IMU with camera, IMU with Bluetooth, WiFi-assisted IMU positioning, and IMU combined with other sensors. By examining these different sensor configurations, this section explains how additional signals can support the wearable inertial indoor positioning and improve positioning accuracy.

1) IMU Only

The IMU is one of the most widely used core sensors in wearable inertial navigation systems. Its navigation principle is based on inertial navigation, where measurements from different IMU sensors are processed and integrated to estimate the navigation orientation, velocity, and position. A typical 6 DoF IMU includes an accelerometer and a gyroscope, which measure specific force and angular velocity, respectively. During navigation computation, rotation matrices are commonly used to describe the body attitude and its changes. These concepts were explained in Subsection A.

As shown in Figure 2, the navigation process begins with the gyroscope. As introduced in subsection A, the gyroscope measures the body angular velocity in the body frame. By integrating this angular velocity, the change in attitude relative to the navigation frame can be computed,

and the rotation matrix is updated. This step provides the transformation from the body frame to the navigation frame and forms the basis for converting accelerations. Next, the specific force measured by the accelerometer is converted to the navigation frame using the attitude information obtained from the gyroscope. The gravity component is then removed to obtain the true acceleration in the navigation frame. Integrating this acceleration gives the change in velocity, and integrating the velocity again produces the change in position.

For 10 DoF IMUs that incorporate additional sensors, the navigation workflow becomes more complex (see Figure 2). In the attitude-estimation stage, the magnetometer is used together with the gyroscope to estimate the body orientation relative to the Earth's magnetic field and update the rotation matrix. The accelerometer is processed in the same way as in a 6 DoF IMU: its measurements are transformed into the navigation frame, gravity is compensated, and the results are integrated to obtain velocity and position. However, the process does not end there. In a 10 DoF IMU, the magnetometer is used not only for initial attitude estimation but also for correcting the final position output. At the same time, the barometer provides height information that further refines the final position estimate, especially in the vertical direction. By combining data from these sensors, the system effectively reduces the accumulated error of inertial navigation. In the end, the corrected position, velocity, and attitude are produced as the navigation output at each time step, completing the full processing shown in Figure 2.

Even a 10 DoF IMU still suffers from noise, bias, and other types of measurement errors. These errors accumulate over time, causing the estimated position to gradually drift. As a result, it is difficult for the navigation system to maintain accurate positioning when relying solely on this method for an extended period. In practical applications, IMUs are often combined with external sensors such as cameras, WiFi, UWB, or Bluetooth. Alternatively, sensor fusion algorithms are applied to correct the IMUs measurements and outputs, helping to reduce drift and improve positioning accuracy.

2) IMU with camera

In wearable inertial navigation systems, miniature cameras provide optical information that helps estimate a device's position by analysing visual features in the scene, such as textures, landmarks, or custom LED light sources. With the development of lightweight and compact imaging devices, miniature cameras are distinguished by their small form factor while maintaining sufficient image resolution, making them ubiquitous components in smartphones, smart glasses, and other wearable platforms. These devices serve as essential tools for positioning and calibration within inertial navigation architectures. Their compact size and low weight make them particularly well-suited for integration into head-mounted wearable devices, such as smart glasses, where space and weight constraints are critical [25]–[27] (shown as Figure 3).

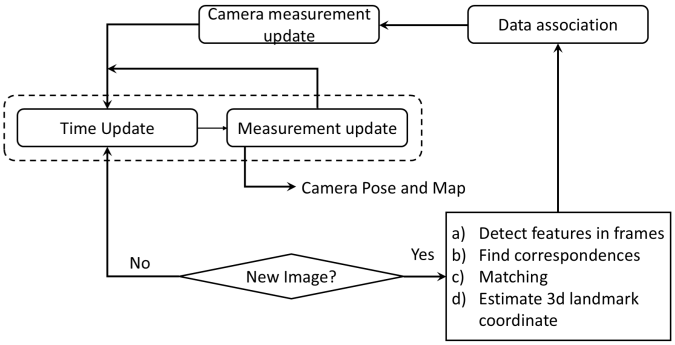

FIGURE 3. System architecture for wearable inertial indoor positioning via IMU and camera sensor fusion. The workflow commences with inertial measurements from the IMU (dashed box), which feed into the prediction correction cycle of the extended Kalman filter (EKF). Upon acquiring a new camera frame, the system performs feature detection, correspondence finding, matching, and 3D landmark estimation. Data association validates feature correspondences before integrating camera measurements, producing refined estimates of camera pose and environmental map.

The fusion of miniature cameras with IMUs enables more accurate navigation by using visual cues to correct the drift that naturally accumulates in IMU based estimation. In such systems, the IMU provides high frequency motion data, including step length and orientation, whilst the camera offers low frequency but absolute positional references, for example, by recognising landmarks or scene features. When the camera detects a known location, it can reset the accumulated IMU drift or align the estimated trajectory with the actual map structure.

The positioning system operates through a continuous prediction correction cycle, with inertial data from the IMU serving as the primary input to the Time Update and Measurement Update modules (indicated by the dashed box). When a new image frame becomes available, the camera processing pipeline executes four sequential operations: (a) detection of salient features within the frame; (b) identification of feature correspondences between consecutive frames; (c) matching of features against the existing map representation; and (d) estimation of three dimensional landmark coordinates. Prior to integration with the Measurement Update stage, the Data Association module plays a critical role in validating observed features against the current map. This validation step ensures measurement consistency by correctly identifying which mapped features correspond to newly observed camera measurements, thereby preventing erroneous updates from mismatched or ambiguous feature associations. The refined camera measurements subsequently update the system state estimates, producing improved camera pose and map outputs that feed back into the continuous localisation process, effectively mitigating IMU drift through visual constraints.

3) WiFi assisted IMU positioning

WiFi is a wireless communication technology based on electromagnetic waves, allowing devices to transmit data

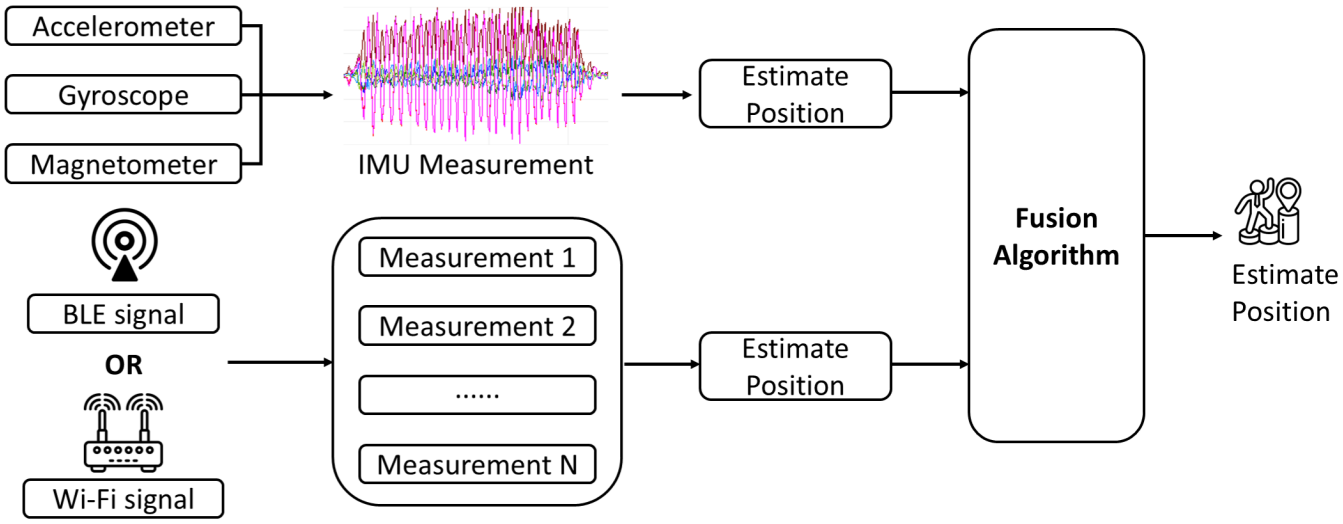

FIGURE 4. **Overview of the inertial navigation process in which IMU measurements comprising accelerometer, gyroscope and magnetometer data are combined with radio frequency signals such as BLE or WiFi. Each sensing modality provides an independent position estimate, and these estimates are subsequently integrated through a fusion algorithm to produce a refined and more robust final position estimation.**

through access points (APs) operating in the 2.4 GHz or 5 GHz frequency bands. In inertial navigation systems, WiFi serves as a complementary positioning modality due to its widespread availability in modern buildings. Specifically, WiFi based indoor positioning estimation can be employed to calibrate IMU based trajectory estimates, with specific APs functioning as spatial landmarks to constrain accumulated drift and improve overall localisation accuracy. This approach to inertial positioning is often applied to smart devices such as smartphones and smart glasses [28]–[30] (shown as Figure 4).

For instance, a smartphone can scan nearby WiFi access points to obtain their MAC addresses and received signal strength indicator (RSSI) values, which are subsequently employed to infer its position [28]. During user motion, two complementary fusion strategies can be employed. In the first strategy, WiFi-based indoor positioning periodically supplies absolute position estimates to calibrate the IMU-derived trajectory, thereby reducing the drift that accumulates in inertial measurements [30]. This calibration typically occurs every few seconds or at strategically selected locations where WiFi signals are sufficiently robust. In the second approach, specific WiFi access points are designated as spatial landmarks; when the device detects these APs, their known positions are used to recalibrate the estimated trajectory, effectively anchoring the IMU's relative motion estimates to fixed reference points in the environment [29]. Alternatively, filtering algorithms such as Kalman filters (KFs) or particle filters (PFs) can be employed to dynamically fuse the IMU's continuous relative motion trajectory with the discrete absolute position measurements derived from WiFi signals, thereby continuously correcting the estimated position and mitigating cumulative errors [31].

The stepwise process of sensor fusion for inertial navigation is clarified in Figure 4. Initially, raw inertial measurements are acquired from the accelerometer, gyroscope, and magnetometer embedded within the device. These measurements are integrated over time to estimate a preliminary position trajectory based solely on inertial data. Concurrently, radio frequency sources such as WiFi access points generate multiple signal measurements, including RSSI and time-of-flight data, which are independently processed to derive an additional position estimate grounded in absolute spatial references. Subsequently, both the IMU derived relative position estimate and the RF based absolute position estimate are fed into a fusion algorithm. This algorithm intelligently combines their complementary strengths: the high frequency continuity of IMU data and the drift free absolute positioning capability of RF signals.

4) IMU with Bluetooth

Bluetooth is a low-power wireless communication technology operating in the 2.4 GHz band and sharing the same frequency spectrum as WiFi. Originally conceived to facilitate short-range connectivity between smartphones and peripheral devices such as headphones or fitness trackers, Bluetooth has subsequently emerged as a valuable complement to inertial navigation systems. Given its operation within the same frequency band as WiFi, Bluetooth-based positioning employs fundamentally similar localisation methodologies. These include trilateration based on distance calculations derived from received signal strength (RSS) values [32], fingerprinting techniques that match observed signal patterns against pre-constructed radio maps [33]–[35], and beacon-based positioning that exploits known reference points to constrain position estimates [4], [36], [37], as illustrated in Figure 4. In this context, Bluetooth beacons are strategically deployed throughout the environment, and wearable devices

estimate their location by scanning for nearby beacons and processing their MAC addresses alongside RSS measurements.

However, a crucial distinction between Bluetooth and WiFi lies in their respective operational ranges and design philosophies. Whilst WiFi networks are designed for longer-range data transmission typically extending tens of metres Bluetooth operates over considerably shorter distances, generally within a 10 metre radius for most applications. This inherently limited range reflects Bluetooth's original design intention: proximity detection and local device pairing rather than wide-area network coverage. Consequently, Bluetooth positioning is particularly well-suited to fine-grained, localised tracking scenarios where detecting presence within specific zones or near particular reference points is paramount.

The fusion of IMU and Bluetooth data enables more accurate positioning by synergistically combining their complementary strengths [38]. The IMU provides continuous but drift-prone estimates of relative motion through step detection and heading estimation, whilst Bluetooth offers discrete absolute position references particularly when a user passes within proximity of a beacon. Specifically, when Bluetooth detects proximity to a deployed beacon, the system measures the distance from that beacon and exploits this known reference point to reset or correct accumulated IMU drift. Fusion algorithms such as particle filters subsequently integrate Bluetooth's absolute positional constraints with the IMU's continuous relative motion information, thereby mitigating the limitations inherent to each individual sensor modality.

5) IMU combined with other sensors

In inertial navigation systems, IMUs are frequently integrated with complementary sensors to address fundamental limitations inherent in standalone inertial positioning. Pure IMU-based navigation suffers from unbounded drift accumulation due to the double integration of accelerometer noise and gyroscope bias, resulting in positioning errors that grow quadratically over time [39]–[41]. To mitigate this drift and enhance long-term positioning accuracy, multi-sensor fusion architectures have emerged as essential methodologies, wherein external sensors provide periodic absolute position corrections that constrain the error propagation characteristic of dead reckoning systems.

The fusion of IMUs with UWB technology exemplifies this complementary approach, particularly in body-worn navigation applications. UWB systems excel at precise distance measurements between anchor nodes and mobile tags through time-of-flight calculations, thereby constraining the unbounded error growth inherent in dead reckoning IMU systems. The integration of UWB ranging measurements with wearable inertial measurement units, typically positioned at the foot, waist, or wrist, yields absolute positional constraints that mitigate the cumulative drift characteristic of inertial navigation systems. This complementary pairing leverages the high-bandwidth kinematic sensing of IMUs alongside the drift-resistant localization provided by UWB network infrastructure, demonstrating particular utility in GNSS-denied indoor settings.

Similarly, the integration of IMUs with LiDAR demonstrates robust positioning performance under various motion conditions [42]. LiDAR sensors generate dense three-dimensional point clouds of the surrounding environment, enabling accurate spatial mapping and feature extraction. Through iterative closest point (ICP) algorithms or other point cloud registration techniques, LiDAR data yields absolute position estimates that can be fused with IMU measurements. LiDAR systems are becoming smaller for wearable uses like head-mounted or backpack devices for pedestrian navigation, but understanding their deployment context remains essential. In certain experimental frameworks, LiDAR may serve exclusively as ground truth reference data rather than as an operational real-time positioning component, and this methodological distinction warrants careful consideration when interpreting reported accuracies.

These multi-sensor fusion approaches demonstrate that strategically combining IMUs with UWB, LiDAR sensors can substantially improve positioning accuracy across different body-worn locations and motion scenarios, thereby advancing the development of more reliable and robust indoor navigation systems.

C. Positioning Algorithm

Based on the positioning algorithms used in wearable inertial navigation systems, the 124 reviewed papers are classified into four categories: IMU-based algorithms, classical stochastic estimation frameworks, multi-sensor fusion methods, and machine learning-based positioning approaches. Correspondingly, different positioning algorithms require distinct parameters and data sources, which vary systematically according to their classification. IMU-based algorithms rely exclusively on inertial measurement unit signals as their data source. Classical stochastic estimation framework (CSEF) algorithms may utilize IMU signals alone or incorporate additional sensor inputs. Multi-sensor algorithms, by definition, simultaneously integrate IMU signals with data from complementary sensors. ML-based algorithms employ data sources comparable to those of CSEF algorithms, drawing upon either IMU signals independently or in conjunction with supplementary sensor information. This section provides a detailed overview of the fundamental implementation methods for each of these algorithm types.

1) IMU based algorithms

In this review, all positioning systems that rely solely on IMU sensors are classified as IMU based algorithms. The positioning algorithms leveraged include the Inertial Navigation System (INS), Pedestrian Dead Reckoning (PDR), and the Zero Velocity Update (ZUPT) and Zero Angular Rate Update (ZARU) techniques.

Inertial navigation system (INS)

An Inertial Navigation System (INS) is a self-contained positioning technology based on an IMU. It estimates position, velocity, and attitude by measuring the angular velocity and acceleration of the carrier and then integrating these measurements over time. The core idea of INS is to apply Newtons laws of motion, using accelerometers and gyroscopes to measure linear acceleration and angular velocity respectively, and then derive the relative position of the sensor [43], [44].

First, as discussed in Subsection A, the accelerometer and gyroscope can be used to obtain the acceleration $a_n(k)$ in the navigation frame. Starting from the initial state, the velocity at time k can be computed by integrating the acceleration over time. However, IMU measurements are usually discrete rather than continuous. Therefore, the IMU velocity in the navigation frame is calculated in a discrete form as:

$$v^n(k) = v^n(k-1) + a^n(k) \cdot \Delta k \tag{3}$$

Here, $v^n(k)$ represents the velocity in the navigation frame at time k, $v^n(k-1)$ is the velocity in the navigation frame one time stamp before k, $a^n(k)$ is the acceleration at time step k, and Δk represents one time stamp.

Then, by further integrating this velocity in the navigation frame, we can obtain the IMU position relative to the initial state:

$$P^n(k) = P^n(k-1) + v^n(k) \cdot \Delta k \tag{4}$$

where $P^n(k)$ denotes the position vector in the navigation frame at the current time step k, and $P^n(k-1)$ represents the last position vector in the same navigation frame at time step $k-1$.

However, due to drift and noise in IMU sensors, the integration process causes errors to accumulate over time. In particular, position and attitude errors tend to increase rapidly. Therefore, in practical navigation applications, an INS based solely on a single IMU is rarely used independently.

Pedestrian Dead Reckoning (PDR)

PDR is an indoor positioning technique based on IMU sensors. It is widely used in smartphones and wearable devices to estimate a pedestrian's movement trajectory [45]. The main idea is to use inertial sensors such as accelerometers and gyroscopes to detect walking steps, estimate step length, and determine heading, thereby calculating position changes. Unlike traditional inertial navigation systems, PDR avoids the double integration of IMU signals, which greatly reduces cumulative errors and makes it especially suitable for indoor environments without external signals [46], [47].

The basic principle of the PDR algorithm can be divided into four key steps: step detection, step length estimation, heading estimation, and position update [48], [49]. In the step detection stage, the system identifies each walking step by analysing acceleration signals. Common methods include peak detection, zero crossing detection, autocorrelation analysis, and frequency domain analysis. Among these, the peak detection method is the most popular, as it detects periodic peaks in the acceleration signal to determine the walking cycle.

Step length estimation is a critical part of the PDR process [50]. Common approaches include the constant model and empirical models based on acceleration data. The step length can be estimated using the difference between the maximum and minimum values of the acceleration magnitude during each step, which can be expressed as:

$$\begin{aligned} A(k) &= (a_x^2(k) + a_y^2(k) + a_z^2(k))^{1/2} \\ s(k) &= m[(A_{max}(k) - A_{min}(k))]^{1/4} \end{aligned} \tag{5}$$

where $s(k)$ represents the length of one step, m is a gain factor obtained through calibration, and $A_{max}(k)$ and $A_{min}(k)$ are the maximum and minimum values of the acceleration magnitude $A(k)$.

The heading estimation phase is the same as the heading estimation in INS discussed earlier, where the body frame is transformed into the navigation coordinate system using R_b^n:

$$\psi(k) = atan2(R_b^n(k)[1,0]/R_b^n(k)[0,0]) \tag{6}$$

Here, $\psi(k)$ represents the heading angle in the navigation frame at time k, and $R_b^n(k)[i,j]$ represents the element in the i-th row and j-th column of $R_b^n(k)$ (indexed starting from 0).

Finally, in the position update stage, the system computes the current position recursively based on step length and heading angle using the following equations:

$$\begin{bmatrix} x(k) \\ y(k) \end{bmatrix} = \begin{bmatrix} x(k-1) + s(k)\cos(\psi(k)) \\ y(k-1) + s(k)\sin(\psi(k)) \end{bmatrix} \tag{7}$$

This formula assumes a two dimensional plane, which fits most indoor walking scenarios. Overall, the PDR algorithm decomposes pedestrian movement into three measurable quantities step detection, step length, and heading and effectively reduces integration errors in inertial navigation. It has therefore become a practical and efficient solution for indoor positioning.

Zero Velocity Update (ZUPT) and Zero Angular Rate Update (ZARU)

ZUPT and ZARU are two key information aided techniques commonly used to enhance the accuracy of foot mounted PDR systems [51]. They also serve as effective mechanisms to suppress the accumulation of inertial navigation errors. These methods make full use of the periodic foot contact pattern during walking, using the detected stationary moments of the foot as anchor points to correct the drift accumulated in PDR calculations.

Specifically, when a person walks, the foot experiences short stationary periods during the stance phase of each step. The main function of a zero velocity detector is to identify these moments. Common detection methods are based on

multi-condition logic, including checking whether the specific force magnitude is within a reasonable range, whether the local acceleration variance is below a threshold, and whether the angular rate magnitude is close to zero. When all three conditions are satisfied, the system determines that the foot is stationary.

The core idea of zero velocity update is that the foot's velocity in the reference frame should theoretically be zero when it is stationary. However, due to sensor noise and drift, the computed velocity from inertial navigation is not exactly zero. The ZUPT algorithm exploits this discrepancy by constructing a measurement residual, which is formulated as the difference between the velocity vector derived from inertial navigation and a zero velocity vector. This residual can be established by comparing the velocity vector from inertial navigation with a zero vector:

$$\delta v_{zvu} = v^n(k) - \mathbf{0}_{(3\times1)} \tag{8}$$

where the term δv_{zvu} notes the ZUPT measurement residual, representing the difference between the INS estimated velocity and the assumed zero velocity. The vector $v^n(k)$ is the three dimensional velocity estimated by the inertial navigation system at discrete time step k, while $\mathbf{0}_{(3\times1)}$ is a 3×1 zero vector expressing the zero velocity condition imposed during stance.

The error state variables Δx include motion drift state and instrument error state. Position error δP, velocity error δv, and attitude error $\delta\psi$ are selected as motion error state variables, while gyroscope and accelerometer biases b_g and b_a are selected as instrument error state variables, expressed as: $\Delta x = \begin{bmatrix}\delta P & \delta v & \delta\psi & b_g & b_a\end{bmatrix}$. Because the ZUPT only consider the velocity error, so the corresponding measurement matrix clearly shows that this update only relates to the velocity error state:

$$H_{zvu} = \begin{bmatrix}\mathbf{0}_{(3\times3)} & \mathbf{I}_{(3\times3)} & \mathbf{0}_{(3\times3)} & \mathbf{0}_{(3\times3)} & \mathbf{0}_{(3\times3)}\end{bmatrix} \tag{9}$$

Here, the matrix H_{zvu} is the ZUPT measurement matrix that maps the error state vector Δx to the velocity measurement domain. Meanwhile, similar with ZUPT, the ZARU means that the angular velocity of the foot should theoretically be zero, during the static stage. The measurement residual is expressed as:

$$\delta\omega_{zar} = \omega(k) - \mathbf{0}_{(3\times1)} \tag{10}$$

where $\omega(k)$ denotes the 3-axis gyroscope measurement at time step k, while $\mathbf{0}_{(3\times1)}$ is a zero vector representing the assumed true angular rate under the zero-motion condition. The left-hand side, $\delta\omega_{zar}$ is thus the residual between the measured and expected (zero) angular rate.

According to the error state variables, the associated measurement matrix shows that this update mainly contributes to the estimation of gyroscope bias:

$$H_{zar} = \begin{bmatrix}\mathbf{0}_{(3\times3)} & \mathbf{0}_{(3\times3)} & \mathbf{0}_{(3\times3)} & \mathbf{0}_{(3\times3)} & \mathbf{I}_{(3\times3)}\end{bmatrix} \tag{11}$$

Here, H_{zar} is the ZARU measurement matrix that maps the state error vector Δx to the measurement space, typically selecting the gyroscope-bias error components b_g. When the zero-velocity condition is triggered, the system performs ZUPT and ZARU sequentially. Through Kalman filtering, the measurement residuals are converted into corrections for the error state vector. This periodic correction mechanism causes the velocity error to form a sawtooth pattern instead of the continuously growing drift seen in traditional inertial navigation [52]. As a result, the accumulated position drift can be effectively reduced, providing more accurate localisation.

However, this calibration method is limited by the cyclic nature of walking motion. When the sensor movement does not follow a repetitive pattern, such as in non-periodic or free-form motion, this auxiliary localisation approach cannot be applied. Therefore, in the following sections, researchers have introduced alternative techniques to assist wearable navigation systems in achieving accurate positioning.

2) Classical stochastic estimation framework

In this review, positioning systems that depend exclusively on IMU sensors are categorised within the classical stochastic estimation framework. The principal positioning algorithms employed in these systems including Kalman filter (KFs), particle filter (PFs), and simultaneous localisation and mapping (SLAM).

Kalman Filter

The Kalman Filter (KF) is an optimal state estimation algorithm designed for linear dynamic systems. Its main concept is to recursively estimate the system state by combining a mathematical system model with measurement data, while explicitly accounting for estimation uncertainty. In inertial navigation systems, the KF is widely used to estimate and correct errors introduced by inertial sensors, thereby improving overall navigation accuracy [53]–[55].

Before applying the KF, the system state and measurement signals must be defined in advance, since different measurements correspond to different observation matrices $H(k)$. In this section, a simple form of the Kalman filter is introduced, which assumes that the user walks in a straight line at a constant velocity. The system state vector is defined as $\mathbf{x}(k) = [P(k), v(k), \omega(k)]^T$, while the measurement vector is defined as $z(k) = [P_{meas}(k), \omega_{meas}(k)]^T$. During the state transition, the position is updated as $P(k) = P(k-1) + v(k-1)\cdot\Delta k$. Based on this relationship, the state transition matrix $F(k)$ and the state evolution equation can be written as

$$\begin{aligned} F(k) &= \begin{bmatrix}1 & \Delta k & 0\\ 0 & 1 & 0\\ 0 & 0 & 1\end{bmatrix} \\ \mathbf{x}(k) &= F(k)\cdot\mathbf{x}(k-1) + n(k) \end{aligned} \tag{12}$$

where $n(k)$ represents process noise originating from IMU uncertainties. Since the measurement vector does not include

velocity, the measurement transition matrix $H(k)$ and the measurement vector $z(k)$ (ignoring measurement noise) are defined as

$$\begin{aligned} H(k) &= \begin{bmatrix} 1 & 0 & 0 \\ 0 & 0 & 1 \end{bmatrix} \\ z(k) &= H(k) \cdot \mathbf{x}(k-1) \end{aligned} \tag{13}$$

In the prediction stage, the system uses the previous state estimate and the dynamic model to predict the current state and its associated covariance, while temporarily ignoring measurement noise. The predicted state is denoted as $\hat{\mathbf{x}}_{pre}(k)$, and the predicted covariance $\hat{Q}_{pre}(k)$ is given by

$$\begin{aligned} \hat{\mathbf{x}}_{pre}(k) &= F(k) \cdot \hat{\mathbf{x}}(k-1) \\ \hat{Q}_{pre}(k) &= F(k) \cdot Q(k-1) \cdot F^T(k). \end{aligned} \tag{14}$$

where $\hat{\mathbf{x}}_{pre}(k)$ is the predicted state, $\hat{\mathbf{x}}(k-1)$ is the previous optimal estimate, and $\hat{Q}_{pre}(k)$ is the predicted covariance (ignoring noise).

In the update stage, the Kalman filter refines the predicted state using the available measurements. By taking the derivative of the optimal state estimation equation, the Kalman gain $K(k)$ is defined as

$$K(k) = \hat{Q}_{pre}(k) H^T(k) [H(k) \hat{Q}_{pre}(k) H^T(k)]^{-1} \tag{15}$$

Using this gain, the state estimate is

$$\hat{\mathbf{x}}(k) = \hat{\mathbf{x}}_{pre}(k) + K(k)[z(k) - H(k)\hat{\mathbf{x}}_{pre}(k)] \tag{16}$$

and the covariance estimate is

$$\hat{Q}(k) = (\boldsymbol{I} - K(k)H(k))\hat{Q}_{pre}(k) \tag{17}$$

The above process describes a simplified application of the Kalman filter in indoor inertial navigation. When different sensors are used, the structure of the state vector and the corresponding transition matrices may change, but the fundamental prediction and update steps remain largely the same. For this reason, the Kalman filter is widely applied in multi-sensor fusion-based indoor inertial navigation systems. In addition, several variants of the Kalman filter, such as the Extended Kalman Filter (EKF) and the Unscented Kalman Filter (UKF), have been developed to handle nonlinear system dynamics that often arise in practical indoor inertial navigation scenarios.

Particle Filter

Particle filtering is a Bayesian filtering method designed to handle non-linear and non-Gaussian systems. It is widely used for state estimation problems, such as PDR. The core idea is to represent the posterior probability distribution of a system's state using a set of random samples, called particles. By performing iterative prediction and update steps, the algorithm gradually approximates the true state of the system.

In particle filtering, the system state is represented by a state vector. For pedestrian navigation, it can be defined as:

$$\mathbf{x}(k) = [P(k), v(k), \omega(k)]^T \tag{18}$$

where $P(k)$ is the position vector, $v(k)$ represents velocity vector, and $\omega(k)$ is attitude angle.

The process begins by initialising a set of particles, where each particle represents a possible state of the system. At the initial time $k = 0$, the initial particle set $\{\mathbf{x}^i(k)\}_{i=1}^N$ is obtained by sampling from the distribution $p(k)$, and the number of particles is set, for example, to $N = 100$, with the initial weight of each particle being $1/N$.

In the prediction step, importance sampling updates particles and weights based on the observation $\mathbf{y}^i(k)$. An importance probability density function $q(\mathbf{x}^i(k)|\mathbf{y}^i(k))$ is constructed, and the weight $w^i(k)$ corresponding to each particle $\mathbf{x}^i(k)$ is calculated according to Formula 19.

$$w^i(k) \propto \frac{p(\mathbf{x}^i(k)|\mathbf{y}^i(k))}{q(\mathbf{x}^i(k)|\mathbf{y}^i(k))} \tag{19}$$

where $p(\mathbf{x}^i(k)|\mathbf{y}^i(k))$ is the posterior probability density function, and $q(\mathbf{x}^i(k)|\mathbf{y}^i(k))$ is the importance probability density function.

Normalise the previous formula, so that $\tilde{w}^i(k)$ can be estimated as:

$$\tilde{w}^i(k) = \frac{w^i(k)}{\sum_{i=1}^N w^i(k)} \tag{20}$$

After normalising, calculate the filtered value. Based on the normalised particle set, the value at time k can be obtained from the state value at time $k-1$, the optimal estimate. The state estimate $\hat{\mathbf{x}}(k)$ is:

$$\hat{\mathbf{x}}(k) = \sum_{i=1}^{N} \tilde{w}^i(k) \cdot \mathbf{x}^i(k) \tag{21}$$

Finally, a resampling step is performed to discard low-weight particles and replicate high-weight ones. This allows the particle set to gradually concentrate around regions of high probability, leading to more accurate estimation of the system state.

The main advantage of particle filtering is its flexibility in integrating multiple sensor inputs and prior knowledge (e. g. , maps). It also maintains strong estimation performance even in environments with non-linear dynamics and non-Gaussian noise.

Simultaneous Localisation and Mapping (SLAM)

SLAM is a core topic in navigation system. Its goal is to enable a moving device to build a map of an unknown environment in real time while estimating its own position. The development of SLAM has supported many applications, including indoor navigation, and mobile mapping [56], [57].

The basic idea of SLAM is to use sensor data such as images, LiDAR point clouds, or inertial measurements to estimate both the motion trajectory of the device (localisation) and the structure of its surroundings (mapping). The main challenge lies in the coupling between mapping and localisation: an accurate map depends on precise localisation, while localisation itself relies on a consistent map. SLAM is usually formulated in a probabilistic framework, where

prediction and update steps are performed iteratively to optimise the state estimation.

Similar to the definition used in the Kalman filter, the system state is defined as $\mathbf{x}(k) = [P(k), v(k), \omega(k)]^T$. However, SLAM introduces an additional and essential element for mapping, called a landmark. As a result, the predicted SLAM state becomes $\mathbf{x}_{SLAM}(k) = [\hat{\mathbf{x}}(k), m_i]^T$, where m_i represents the current landmark. The measurement vector describes the relative relationship between the current state and the corresponding landmark (ignoring the noise in the process), denoted as $z_i(k)$

$$z_i(k) = \begin{bmatrix} ||P(k) - m_i|| \\ atan2(m_i - P(k)) - \omega(k) \end{bmatrix} \tag{22}$$

where $||P(k) - m_i||$ represents the Euclidean distance between the estimated navigation location and the landmark, and $atan2(m_i - P(k)) - \omega(k)$ represents the bearing angle.

Following the Jacobian, the measurement matrix $H_i(k)$ is defined as

$$H_i(k) = \frac{\partial z_i(k)}{\partial \mathbf{x}_{SLAM}(k)} \tag{23}$$

By applying Kalman filtering or other sensor fusion algorithms (see Formula 16), SLAM can further help correct drift introduced by the IMU.

3) Multiple Sensor Fusion

Visual-Inertial Odometry (VIO)

VIO is a technique that estimates a device's position and orientation in real time by fusing data from a camera and an IMU. Its main idea is to combine the high-accuracy environmental features captured by the camera with the high-frequency motion data provided by the IMU. By leveraging the complementary strengths of these sensors, VIO can achieve stable and accurate pose estimation even in complex environments.

VIO methods are commonly divided into two main categories: loosely coupled and tightly coupled approaches. In loosely coupled visual-IMU systems, the IMU and the camera estimate their poses independently, and the resulting pose estimates are then fused. This design helps keep the processing time constant and relatively low. In contrast, tightly coupled methods integrate measurements at a deeper level and are further classified into filter-based and optimisation-based approaches [58].

Filter-based methods typically use Kalman filters or particle filters to predict the system state from IMU measurements and then correct this prediction using visual observations [59]. Optimisation-based methods, on the other hand, apply batch non-linear optimisation to minimise the error between integrated inertial measurements and visual reprojection errors, thereby estimating the camera motion more accurately [60].

When camera observations are available, the visual measurement vector $z_v(k)$ is defined as

$$z_v(k) = \begin{bmatrix} P_v(k) \\ R_v^n(k) \end{bmatrix} \tag{24}$$

In a loosely coupled framework, the IMU and the camera estimate their positions independently, and the camera cannot measure their velocities and angular velocities. So the rotation matrix was omitted. In this case, the visual observation vector is usually treated as the camera position itself

$$z_v(k) = P_v(k) = P(k) + n_v \tag{25}$$

Where n_v representing the measurement noise in the process.

Following this, the IMU and the camera compute their own residuals, denoted as r_{imu} and r_v

$$r_{imu}(k) = \begin{bmatrix} P(k+1) - \hat{P}(k+1) \\ v(k+1) - \hat{v}(k+1) \\ \omega(k+1) - \omega_{meas}(k) \end{bmatrix} \tag{26}$$

$$r_v(k) = P(k) - P_v(k)$$

where $\omega_{meas}(k)$ is the gyroscope measurement. These residuals describe the difference between each sensors estimated position and the true position, calculated within their own coordinate systems.

Given time step Δk, velocity update and position update can be carried out using Formulas 3 and 4.

Based on the Jacobian formulation, a weighting matrix w_{imu} and w_v are assigned to each sensor to reflect its contribution and reliability. It is defined as

$$||r||^2 \cdot w = r^T \cdot w \cdot r \tag{27}$$

Finally, the system searches for the state $\mathbf{x}(k)$ that minimises the total cost function:

$$\min_{\mathbf{x}(0:N)} \sum_k (||r_{imu}(k)||^2 \cdot w_{imu} + ||r_v(k)||^2 \cdot w_v) \tag{28}$$

where N represents the last time step. This optimal state $\mathbf{x}(k)$ is taken as the estimated pose of the system.

WiFi-Inertial Odometry (WIO)-EKF

Combining WiFi and IMU data is a common approach used by researchers to improve positioning accuracy in inertial navigation. The main idea of this fusion method is to use IMU sensors to perform PDR, which estimates position by detecting steps, estimating step length, and calculating heading. At the same time, WiFi signals are used to correct the accumulated errors in PDR, helping to prevent position drift.

In the previous introduction, several WiFi-based positioning methods were mentioned, such as AP, RSS, and Round Trip Time (RTT). Among these methods, the most widely used approach is positioning assisted by WiFi Access Points (APs). In this method, the observation vector $z_{ap}(k)$ can be defined as

$$z_{ap}(k) = P(0) - 10t \log_{10}(\frac{||P(k) - P_{ap}(k)||}{d(0)}) + n_{ap}(k) \tag{29}$$

Here, $P(0)$ denotes the initial position, and t is the path-loss exponent. In free space, $t = 2$; in office or building environments, typically t ranges from 3 to 4; and in dense

indoor environments, t usually ranges from 4 to 6. $P_{ap}(k)$ represents the known position of the i-th WiFi AP in the same coordinate system as the IMU navigation state $P(k)$. $d(0)$ denotes the Euclidean distance between $P_{ap}(0)$ and $P(0)$, and $n_{ap}(k)$ represents process noise.

Next, the Jacobian matrix is used to compute $H_{AP}(k)$, which is given by

$$\begin{aligned} H_{AP}(k) &= \frac{\partial z_{ap}(k)}{\partial P(k)} \\ &= -\frac{10t}{\ln(10)} \frac{P(k) - P_{ap}(k)}{||P(k) - P_{ap}(k)||^2} \end{aligned} \tag{30}$$

This avoids the need to explicitly compute the actual WiFi state $\mathbf{x}_{AP}(k)$. The KF or another fusion algorithm can then be used to perform optimal fusion and obtain the final estimated state.

When using WiFi signals for assisted positioning, a key difference from camera-based methods is that WiFi positioning is usually performed independently from the IMU. The resulting position estimate is then treated as a measurement vector and fused with the IMU-based position estimate using fusion algorithms such as the Kalman filter or particle filter. This approach greatly reduces computational complexity. However, independent position estimation can lead to significant drift between the two estimates. Therefore, additional constraints, such as map information, are required to further correct and refine the estimated position.

BLE-PDR

To improve dynamic positioning accuracy in inertial navigation, data fusion between BLE and an IMU is commonly employed. BLE provides low-frequency absolute position references through RSSI, but it is easily affected by multipath effects. The IMU delivers high-frequency relative displacement and attitude changes, but suffers from integration drift. By fusing BLE and IMU data using algorithms such as the Kalman filter, the IMU can compensate for BLE update delays, while BLE measurements can correct IMU drift.

In Bluetooth-assisted positioning, the RSSI-based method is one of the simplest approaches and is widely favoured by researchers. Since RSSI measurements provide only signal strength, the receiver position $P(k)$ can be roughly estimated using the known locations of Bluetooth beacons. Therefore, the measurement vector is defined as

$$z_{BLE}(k) = P_{BLE}(k) + n_{BLE}(k) \tag{31}$$

where $n_{BLE}(k)$ represents measurement noise. From this formulation, the measurement state vector is related only to position. Based on the previously defined state vector $\mathbf{x}(k) = [P(k), v(k), \omega(k)]$, the measurement matrix $H_{BLE}(k)$ can be derived as

$$H_{BLE}(k) = \begin{bmatrix} \mathbf{I}_{3\times3} & 0 & 0 \end{bmatrix} \tag{32}$$

Then, as with other fusion algorithms such as the Kalman filter or particle filter are applied to obtain a more accurate final position estimate.

4) Machine Learning based Algorithm

In studies on machine-learning-based IMU positioning, sensor data fusion methods have become increasingly diverse to enhance the accuracy and robustness of trajectory estimation. As a subset of machine learning, deep learning approaches including convolutional neural networks (CNNs) [61], [62], and multilayer perceptrons (MLPs) [63] have been widely adopted in this domain. One prevalent approach integrates attention mechanisms to augment the capability of hybrid convolutional and recurrent architectures in extracting salient temporal features [11], [64]. Certain methods employ regression models that integrate depth-wise separable convolutions with residual connections, thereby reducing computational complexity whilst preserving accuracy, which renders them particularly suitable for edge deployment [65]. Furthermore, several studies have merged extended Kalman filter (EKF) with residual networks to investigate the synergy between traditional filtering methodologies and contemporary deep learning techniques [66].

In terms of sensor data modelling, some work integrates convolutional networks, recurrent networks (e.g., Long short-term memory (LSTM)), and multilayer perceptron, or incorporates temporal attention mechanisms to improve the processing of inertial sequences. Other approaches use residual structures with random direction initialisation to enhance position estimation accuracy or develop recurrent-network-based gravity estimation modules to improve 3D trajectory reconstruction. Furthermore, certain studies propose deep neural network-based weighted fusion models to achieve high-precision positioning in industrial settings, while others combine densely connected networks with particle filtering strategies to handle continuous tracking tasks in complex human machine interaction scenarios.

D. Taxonomy

The field of wearable inertial navigation presents a uniquely complex landscape that necessitates multifaceted taxonomic frameworks for meaningful analysis. Unlike conventional navigation systems that typically employ standardised configurations, wearable inertial measurement systems operate at the intersection of multiple design dimensions, each offering distinct trade-offs between accuracy, practicality, and computational efficiency. Researchers and practitioners must navigate critical decisions across three principal domains: sensor fusion, where data from IMUs are integrated with complementary modalities such as camera, WiFi, BLE or UWB; The choice of body placement whether foot, wrist, or head fundamentally influences measurement characteristics; and algorithmic approaches, spanning from classical stochastic filtering techniques to contemporary machine learning architectures. This multidimensional design space renders any single classificatory scheme insufficient for capturing the field's inherent heterogeneity. Consequently, the present review adopts multiple complementary taxonomies organised around sensor configurations, sensors placement,

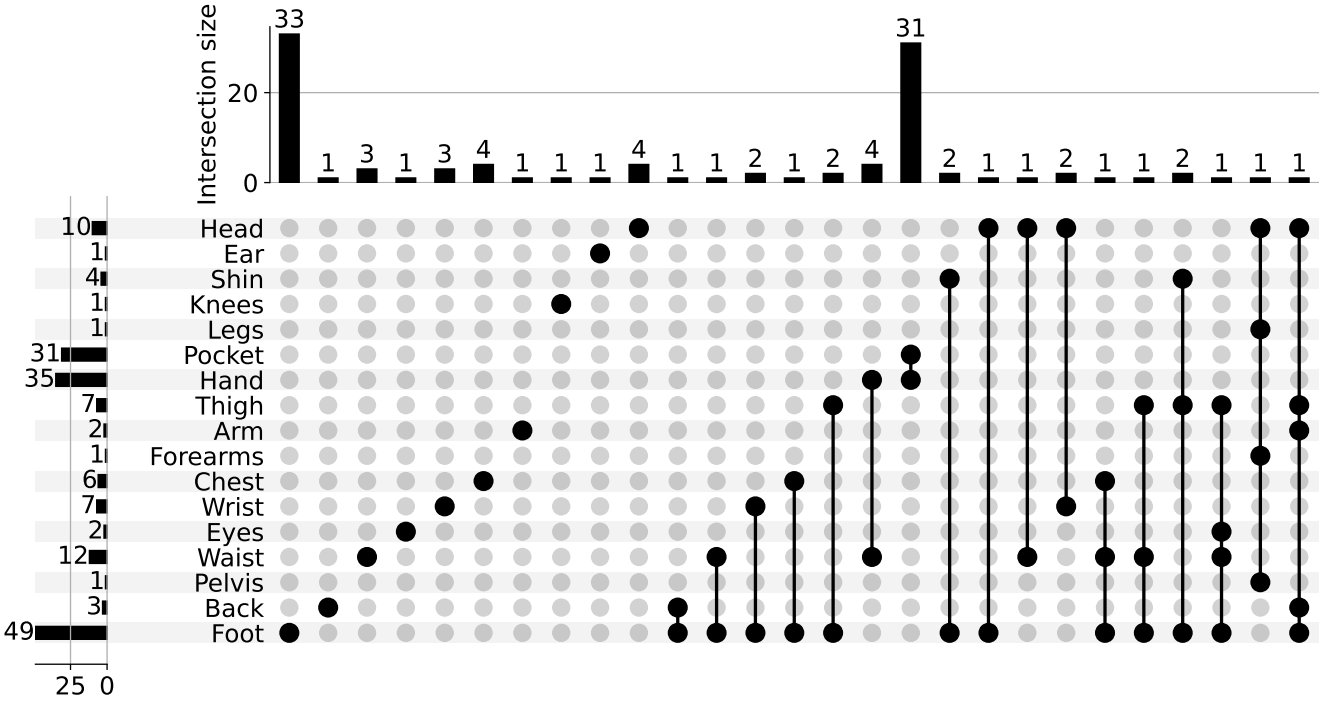

FIGURE 5. **Distribution and co-occurrence of IMU sensor placements on different human body parts across 124 reviewed studies. The plot illustrates the frequency and combination patterns of sensor deployment across 17 distinct anatomical locations. The vertical bar chart (left) displays the frequency with which each body part was utilised for sensor placement across all reviewed studies. The dot matrix in the centre indicates which body parts were employed in individual studies, with connecting lines representing instances where two or more body parts were instrumented simultaneously within the same investigation. The horizontal bar chart (top) quantifies the number of studies employing each specific combination of body parts. This visualisation enables systematic examination of both the individual popularity of sensor locations and the prevalence of multi-site sensor configurations in current research practice.**

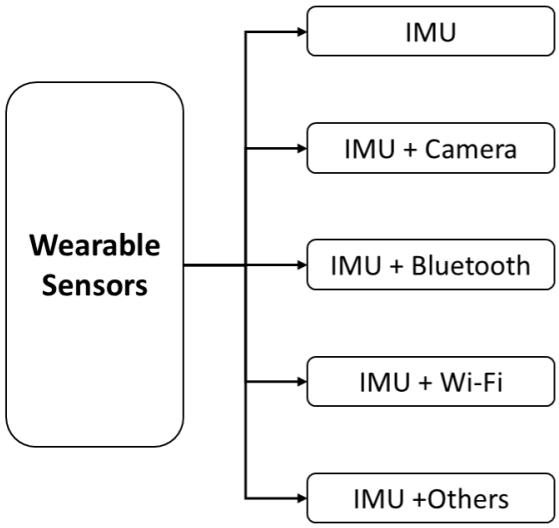

FIGURE 6. **The taxonomy of the included studies for wearable inertial navigation systems for indoor positioning based on signal types.**

and computational frameworks, thereby providing a comprehensive analytical lens through which to examine the diverse methodological approaches that characterise contemporary wearable inertial navigation research.

In the reviewed literature, researchers provided detailed information about the body locations where wearable sensors were placed (as shown in Figure 5). The Upset plot reveals that sensor placements varied considerably across studies, with certain body locations being employed more frequently than others. Notably, the wrist emerged as the most commonly utilised placement site, appearing in over 60 studies, followed by the chest and ankle. The upset figure demonstrated that whilst some studies deployed sensors on a single body region, others adopted multi-site configurations combining two or more placements simultaneously. These findings informed the development of our body location taxonomy, which categorises the 17 identified body parts into six primary groupings. This classification scheme was derived systematically based on the frequency of usage and practical co-occurrence patterns observed in the literature, with the six categories representing the most prevalent sensor deployment strategies amongst researchers.

The taxonomy clusters the 17 identified body locations into six categories according to anatomical proximity and functional similarity. Three categories correspond to single anatomical regions hand only, foot only, and head only where all sensors, irrespective of their number, were positioned exclusively within one such region. The remaining three categories span multiple anatomical areas and are therefore

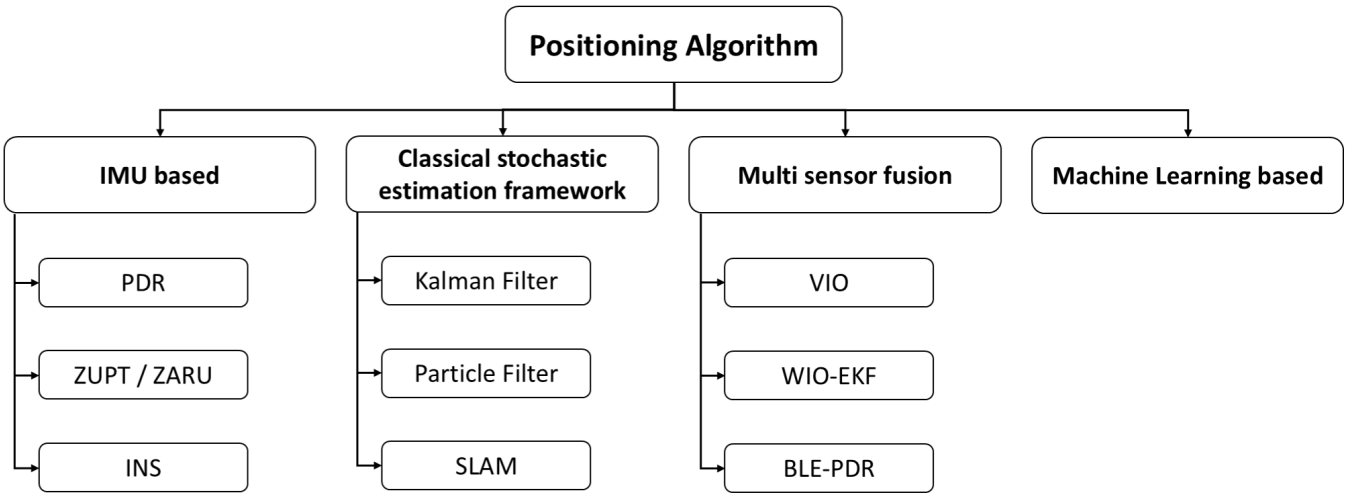

FIGURE 7. **The taxonomy of the included studies for wearable inertial navigation systems for indoor positioning based on positioning algorithm. The four categories are mainly distinguished by the level of their primary algorithmic contribution which makes these categories not mutually exclusive.**

classified as upper body, lower body, and whole body. The upper body category comprises sensor placements at or above the waist, typically involving multiple sensors mounted at different upper body sites, for example, one IMU on the head and another on the waist in the same experiment [67]. Notably, the wrist is excluded from this category, as empirical analysis indicates that wrist-worn sensors are commonly evaluated when the arm rests naturally at the side, which does not constitute an above-waist position. The lower body category includes sensors placed below but not directly on the waist, again requiring multiple sensors distributed across distinct lower-limb locations; for instance, an IMU may be positioned on the thigh while another is attached to the shoe [66]. Finally, the whole body category encompasses configurations in which sensors are distributed across several body parts simultaneously; for example, [68] deployed sensors on the foot, thigh, wrist, and head.

Based on the types of wearable sensors and positioning algorithms employed, the included wearable inertial navigation studies are classified from two complementary perspectives. From the sensor perspective, the studies are categorised into six distinct groups: IMU only systems, which rely exclusively on inertial measurement unit sensors for navigation; IMU fusion with camera systems, which combine IMU signals with RGB or RGB-D visual data; IMU fusion with Bluetooth systems, which integrate IMU measurements with BLE signals; IMU fusion with WiFi systems, which synthesise IMU data with WiFi positioning information; and IMU fusion with other sensors, encompassing systems that incorporate additional sensing modalities such as UWB or radar signals technologies. This taxonomic framework enables a systematic examination of how different sensor configurations contribute to enhanced positioning accuracy and robustness in wearable navigation systems (see Figure 6).

According to the positioning algorithm used (see Figure 7), the reviewed studies are grouped into four categories: IMU-based positioning algorithms, multi-sensor fusion algorithms, classical stochastic estimation frameworks, and machine learning based positioning algorithms. From the algorithm perspective (noting that most studies use multiple techniques, but only the core algorithm is considered here), IMU-based positioning algorithms directly compute position from IMU data without modelling or training; these include PDR, ZUPT, and INS methods. Classical stochastic estimation frameworks refer to traditional approaches such as the Kalman filter, particle filter, and SLAM. Multi-sensor fusion algorithms are distinguished from the other three categories not merely by the use of additional sensors, but by the fact that their core algorithmic contribution centres on the fusion architecture and the strategy for integrating heterogeneous sensing modalities. Finally, machine learning based positioning algorithms build on the previous three methods by using trained models to learn and predict drift behaviour, thereby reducing final positioning errors. However, it's worth emphasizing here that these four categories differ not only in their data sources but, more fundamentally, in the level at which their primary algorithmic innovation operates. IMU-based algorithms process only inertial measurement unit signals and contribute at the signal-processing level (e.g., step detection, heading estimation). CSEF algorithms contribute at the state-estimation level, designing probabilistic models and filter structures; they may accept IMU signals alone or incorporate additional sensor inputs as supplementary measurements. Multi-sensor fusion algorithms contribute at the fusion-architecture level, designing how heterogeneous sensor streams are jointly modelled, weighted, and integrated; by definition, they always combine IMU signals with data from at least one additional modality. ML-based algorithms contribute at the learning level, training models to capture complex motion patterns or predict drift; like

CSEF methods, they may operate on IMU signals alone or in conjunction with supplementary sensor inputs. Therefore, it is important to acknowledge that these four categories are not strictly mutually exclusive. A single study may combine elements from multiple paradigms. In such cases, each study is assigned to the category that best represents its primary algorithmic contribution, which also depicts commonly occurring cross-category combinations.

For the 124 papers included in this review, we employed a dual-taxonomy framework that integrates body location with algorithm sensor pairings to provide sufficient granularity for meaningful methodological comparison whilst preserving conceptual coherence and clarity. Although body location, algorithm type, and sensor modality represent three distinct dimensions, our analytical approach treats the latter two as a unified classification axis. This decision reflects the inherent interdependence between algorithmic approaches and sensor technologies: specific algorithms are frequently designed to exploit particular sensor characteristics, and conversely, sensor selection is often dictated by algorithmic requirements. For instance, convolutional neural networks typically operate on image data from cameras [11], whilst decision trees and support vector machines predominantly process feature vectors extracted from IMUs [65]. By representing algorithm and sensor as an integrated taxonomy rather than as independent dimensions, we avoid artificially fragmenting methodologically coherent approaches and instead capture the natural coupling observed in the empirical literature. Although additional dimensions such as individual sensor models or detailed algorithmic subtypes could, in principle, be incorporated, our analysis demonstrates that these finer distinctions seldom influence the core methodological patterns reported across the literature. Consequently, the figure presents only these two taxonomies body location as one dimension, and algorithm sensor combinations as the other as they capture the most consequential sources of variation in experimental design without over complicating the classification scheme. This focused framework provides a stable foundation for robust statistical analysis of methodological trends, enabling comparisons that are both systematic and interpretable.

TABLE 2: Comparison of Wearable Inertial Navigation Systems for Indoor Positioning

No.	Body parts	Signal type	IMU Type	IMU From	Algorithm	Path length	Testbed Type ⋆	2D/3D	Path type	Performance metric (value)
[69]	Foot+ Wrist	IMU	6 DoF IMU	Xsens MTw	ZUPT+ EKF	740 m	School Road	2D	Complex	Rate Error: 0.12 m/s
[53]	Foot	IMU	6 DoF IMU	-	ZUPT+ Informer+ KF	2000 m	Stadium	3D	Complex	Cumulative Error: 19.77 m
[66]	Foot+ Thigh	IMU	6 DoF IMU	Xsens MTi-300	ZUPT+ GRU-SVR	360 m, 500 m	School Road	3D	Complex	Percentage Error: 1.14 %, 1.68 %
[6]	Foot	IMU+ UWB	6 DoF IMU	ADXL345+ ITG-3200	PDR+ ZUPT+ HDR+ EKF	55 m	office room, Corridor	2D	Loop	Percentage Error: 0.59 %
[70]	Head	IMU+ RGB	6 DoF IMU	Google Glass	VINS+ IKS	127 m	office room	3D	Straight+ Turn	Percentage Error: 0.32 m
[71]	Foot+ Shin+ Thigh	IMU	6 DoF IMU	BMX055	PDR+ Neural Networks	$\sim$ 1400 m	Road	3D	Straight	Mean Error: 0.33 m/s
[72]	Waist+ Chest+ Foot	IMU	9 DoF IMU	sbg IG-500N	ZGT+ EKF	$\sim$ 230 m	office room	3D	Loop	Percentage Error: 0.8 %
[73]	Foot+ Waist	IMU	6 DoF IMU	POS-1200+ YDL-602	PDR+ ZUPT+ INS+ KF	$\sim$ 1900 m	office room, Road	3D	Loop	Cumulative Error: 2.66 m
[74]	Foot	IMU	9 DoF IMU	SparkFun Ultimate	NZUPT+ CGN+ HDE+ PF	$\sim$ 800 m	Urban Road	3D	-	Cumulative Error: 10 m
[75]	Hand+ Waist	IMU	6 DoF IMU	C8051F500 MCU, InvenSense sensors	Fuzzy PDR+ Complementary filter	45 m	Exhibition hall	2D	Straight	Cumulative Error: 0.14 m
[76]	Head	IMU+ RGB-D	9 DoF IMU	Phidgets Spatial 3/3/3	SLAM+ PF	$\sim$ 120 m	Corridor	2D	Straight+ Turn	ATE: 0.2 m
[77]	Foot	IMU	6 DoF IMU	-	ZUPT+ EKF	-	Laboratory	3D	Straight+ Loop+ Stair	Cumulative Error: 0.209 m
[78]	Foot	IMU	6 DoF IMU	Memsense nIMU	PDR+ ZUPT+ HDR	$\sim$ 1800 m	Urban Road	2D	Straight	End Error: 9.6 %
[79]	Foot+ Shin	IMU	6 DoF IMU	WHU-i2Nav	INS+ ZUPT+ EKF	$\sim$ 100 m	Stadium	3D	Straight+ Loop	ATE: 2.24 m
[80]	Foot	IMU	9 DoF IMU	ADIS16480	PDR+ ZUPT+ ESKF	30.5 m	Office Room	2D	Loop	Cumulative Error: 0.11 m
[81]	Foot	IMU	9 DoF IMU	MicroStrain 3DM-GX3-25	ZVU+ HDR+ EKF	$\sim$ 120 m	Hallway	3D	Straight+ Loop	Cumulative Error: 0.45 m
[82]	Foot+ Head	IMU	6 DoF IMU+ Barometer	Xsens MTi-G-700	ZUPT+ KF	-	Office room	3D	Jumping	Cumulative Error: $\sim$ 0.27 m
[83]	Foot+ Shin+ Thigh	IMU	9 DoF IMU	MPU9250	HDR+ ZUPT+ SEC+ EKF	$\sim$ 56 m	Laboratory	3D	Loop	Cumulative Error: 0.15 m

⋆ In test type, straight walking is labelled as straight, studies focusing on turning are labelled as turning, looping experiments are labelled as looping, experiments involving going up and down stair are labelled as stairs, and finally, if all of the above situations appear in one experiment, it is labelled as complex.

TABLE 2 – Comparison of Wearable Inertial Navigation Systems for Indoor Positioning

No.	Body parts	Signal type	IMU Type	IMU From	Algorithm	Path length	Testbed Type ⋆	2D/3D	Path type	Performance metric (value)
[84]	Foot	IMU	9 DoF IMU	Casio	SEC+ LD	∼ 20 m	Office room	3D	Straight	End-pose Error: 0.02 m
[54]	Chest	IMU	6 DoF IMU	Smart Phone	INS+ PDR+ KF	193 m	Corridor	2D	Loop	ATE: 1.534 m
[13]	Wrist	IMU+ Pressure sensor	9 DoF IMU+ Barometer	ARM Cortex-M4F, 10 DoF	PDR+ Random Forest for gait ID+ EKF	190 m	Hall, Urban Road	3D	Straight+ Loop	Cumulative Error: 0.855 m
[85]	Head	IMU	6 DoF IMU	Xsens Dot	LSTM (HINNet)+ SLAM (HeadSLAM)+ PF	∼ 750 m	Urban Road	2D	Loop	ATE: 2.69 m
[68]	Foot+ Eyes+ Thigh+ Waist	IMU	6 DoF IMU	Xsens MTw	foot INS+ PDR	∼ 20,000 m	Large outdoor area	2D	Complex	Rate Error: 0.25 m/s
[86]	Foot	IMU	6 DoF IMU	MPU-9250	SINS+ ZUPT+ EKF	10.14 m, 11.70 m	Office room	3D	Straight+ Stair	Cumulative Error: 0.22 m, 0.26 m
[87]	Foot+ Back	IMU	9 DoF IMU	Xsens Mtw	ZUPT+ ZARU+ AFM	4,196 m	School Road	2D	Loop	Percentage Error: 1.3 %
[88]	Foot	IMU+ UWB	6 DoF IMU	ADXL345, ITG-3200	ZUPT+ EKF	∼ 12 m, ∼ 55 m	Office room	3D	Loop	Percentage Error: 0.5 %, 1 %
[89]	Foot	IMU	6 DoF IMU	Google Glass	PDR+ EKF	∼ 172 m	Corridor	2D	Straight+ Turn	Percentage Error: 2.5 %
[56]	Knees	IMU+ LiDAR+ RGB-D	6 DoF IMU	JY901S	VIO/ SLAM/ Geometric localisation	∼ 50 m	Office room	2D	Straight	Cumulative Error: ∼ 1.5 m
[39]	Head+ Wrist	IMU+ UWB	9 DoF IMU	Xsens MTI-300	PDR+ FGO+ DTW	-	Parking Garage	2D	Straight	Mean Error: 1.74 m
[42]	Chest	IMU+ LiDAR	9 DoF IMU	Xsens	SLAM	∼ 183 m	Office room	3D	Loop	Percentage Error: 0.08 %
[90]	Foot	IMU	6 DoF IMU	APDM Opal	PDR+ ZUPT+ ESKF	∼ 4200 m	Level Ground	3D	Straight+ Stair	Cumulative Error: 0.03 cm
[91]	Foot	IMU	6 DoF IMU	ICM20948	ZUPT+ KF	∼ 54 m	Ramp	3D	Stair	Cumulative Error: 0.02 m
[92]	Foot	IMU	6 DoF IMU	Xsens MTI-G	ZUPT+ KF	∼ 147 m	Uphill	2D	Straight+ Loop	Percentage Error: 0.89 %
[93]	Foot	IMU	6 DoF IMU	MicroStrain 3DM-GX2	ZUPT+ KF	∼ 100 m	Office room	2D	Loop	Percentage Error: 0.44 %
[28]	Hand+ Waist	IMU+ WiFi	9 DoF IMU	Smart Phone	PDR+ EKF	180 m	Office room	2D	Straight	Cumulative Error: 2.5 m
[94]	Foot	IMU	9 DoF IMU	MPU9250+ STM32F405	PDR+ Complementary Filtering	50 m	Library	2D	Loop	Percentage Error: 1.32 %
[4]	Hand+ Waist	IMU+ BLE	6 DoF IMU	Smart Phone	DNN (Bi-LSTM)+ PF	-	Corridor	2D	Loop	Cumulative Error: ∼ 1.76 m

⋆ In test type, straight walking is labelled as straight, studies focusing on turning are labelled as turning, looping experiments are labelled as looping, experiments involving going up and down stair are labelled as stairs, and finally, if all of the above situations appear in one experiment, it is labelled as complex.

TABLE 2 – Comparison of Wearable Inertial Navigation Systems for Indoor Positioning

No.	Body parts	Signal type	IMU Type	IMU From	Algorithm	Path length	Testbed Type ⋆	2D/3D	Path type	Performance metric (value)
[95]	Ear	IMU	9 DoF IMU	-	PDR+ Complementary filter / PF	750 m	Urban Road	2D	Straight+ Loop	Rate Error: 0.15 m/s, 0.11 m/s
[96]	Foot	IMU	9 DoF IMU	Xsens MTx	ZUPT+ EKF	-	Office Room	2D	Loop	Percentage Error: 0.91 %
[97]	Foot	IMU	6 DoF IMU	Crista	ECEF+ ZUPT+ KF	270 m	Office Room	3D	Loop	Cumulative Error: 3.3 m
[98]	Foot	IMU	6 DoF IMU	Xsens MTI-300	ZUPT+ KF	$\sim$ 240 m	Corridor	2D	Straight	Cumulative Error: 4.8 m
[29]	Hand / Pocket	IMU+ WiFi	9 DoF IMU	Smart Phone	WiFi Fingerprinting+ PDR+ Weighted Fusion	$\sim$ 112 m	Corridor	3D	Straight	Percentage Error: $\sim$ 0.98 %
[99]	Waist+ Foot+ Thigh	IMU	6 DoF IMU+ Barometer	Xsens MTW	ZUPT+ WF	$\sim$ 207.72 m	Corridor	3D	Loop	End-pose Error: 2.50 m
[45]	Thigh+ Foot	IMU	6 DoF IMU	-	PDR	$\sim$ 70 m	Corridor	2D	Straight	Mean Error: 0.3$\pm$1.8 m
[100]	Foot+ Wrist	IMU	9 DoF IMU	Xsens Mti	PDR+ EKF	$\sim$ 45 m	Office Room	2D	Loop	End-pose Error: 1.1 m
[101]	Foot	IMU	6 DoF IMU	MPU9250	PDR+ EFK+ modle based correction	$\sim$ 50.34 m	Office Room	3D	Straight+ Stair	Percentage Error: 1.52 %
[40]	Eyes	IMU+ UWB	6 DoF IMU	Bosch BMI263	D-iSAM2 / iSAM2	$\sim$ 170 m	Corridor	3D	Straight+ Turn	Mean Error: 0.3 m
[102]	Foot	IMU	9 DoF IMU+ Barometer	Xsens MTI-100	HMM+ ZUPT+ ZARU+ HDR+ compass algorithm+ EKF	$\sim$ 310 m	Corridor	3D	Stair+ Loop	Percentage Error: 0.207
[103]	Chest+ Foot	IMU	9 DoF IMU	Adafruit BNO055	Azimuth+ PDR	$\sim$ 19 m	Office Room	2D	Straight	Mean Error: 2 m
[57]	Head	IMU+ RGB	6 DoF IMU	InertiaCube2	SLAM+ KF	-	Corridor	3D	Loop	End-pose Error: 1-2 pixels*
[104]	Wrist	IMU	6 DoF IMU	SH3001 MEMS	PDR+ QEKF	$\sim$ 1000 m	School Road	2D	Loop	Percentage Error: 0.5 %
[105]	Hand / Pocket	IMU	6 DoF IMU	Smart Phone	HNNTA(Hybrid CNN-LSTM with Temporal Attention)	21,910 m	Office Room	2D	Loop	ATE: 4.99 m
[106]	Hand / Pocket	IMU	6 DoF IMU	Smart Phone	ResNet-based DNN	$\sim$ 3,000 m	Office Room	2D	Loop	ATE: 0.3 m
[55]	Hand / Pocket	IMU	6 DoF IMU	Smart Phone	IEKF	$\sim$ 200 m	Office Room	3D	Straight	ATE: 1.28 m

⋆ In test type, straight walking is labelled as straight, studies focusing on turning are labelled as turning, looping experiments are labelled as looping, experiments involving going up and down stair are labelled as stairs, and finally, if all of the above situations appear in one experiment, it is labelled as complex.

TABLE 2 – Comparison of Wearable Inertial Navigation Systems for Indoor Positioning

No.	Body parts	Signal type	IMU Type	IMU From	Algorithm	Path length	Testbed Type ⋆	2D/3D	Path type	Performance metric (value)
∗ Study [57] involved mounting a camera on a hat and placing some targets on the walls and ceiling. The position was determined by the offset of the camera's centre crosshair relative to the target's centre crosshair. The performance data here recorded the offset in pixels between the camera's centre crosshair and the target's centre crosshair.										
[64]	Hand / Pocket	IMU	6 DoF IMU	Smart Phone	A2DIO(CNN+ LSTM+ Attention)	21,910 m	Office Room	2D	Loop	ATE: 4.98 m
[61]	Hand / Pocket	IMU	6 DoF IMU	Smart Phone	SSHNN (CNN+ LSTM+ MLP)	21,910 m	Office Room	2D	Straight	ATE: 1.71 m
[107]	Hand / Pocket	IMU	6 DoF IMU	Smart Phone	FDIO (EKF+ ResNet)+ EKF	21,910 m	Office Room	2D	Straight	ATE: 5.60 m
[65]	Hand / Pocket	IMU	6 DoF IMU	Smart Phone	RIDI (SVM+ SVR regression)	-	Office Room	2D	Loop	Mean Error: 1.12 m
[108]	Hand / Pocket	IMU	6 DoF IMU	Smart Phone	RGNet (LSTM-based gravity estimation+ projection+ integration)	$\sim$ 800 m	Corridor	3D	Straight	ATE: 3.96 m
[109]	Hand / Pocket	IMU	6 DoF IMU	Smart Phone	IMUNet (CNN-based regression)	$\sim$ 320 m	Corridor	2D	Straight	ATE: 1.5 m
[110]	Hand / Pocket	IMU	6 DoF IMU	Smart Phone	RoNIN (Neural network)	21,912 m	Office Room	3D	Straight	ATE: 1.63 m
[111]	Chest	IMU+ + RGB-D	6 DoF IMU	XSENS MT-100, Microstrain 3DM-GX-25	MSCKF+ EKF	185 m	Vicon Warehouse	3D	Straight+ Turn	ATE: 0.193 m
[112]	Foot+ Shin	IMU	6 DoF IMU	WHU-i2Nav	LA-ZPIU+ ZUPT+ ZIHR+ EKF	50 m	Office Room	3D	Complex	End-pose Error: 0.60 m
[113]	Foot	IMU	6 DoF IMU	VectorNav VN-200	ZUPT+ KF	$\sim$ 251 m	School Road	2D	Loop	CEP: 0.96 m
[114]	Foot	IMU	6 DoF IMU	Xsens MTi-G-710	ZUPT+ KF	$\sim$ 100 m	Office Room	3D	Straight	End-pose Error: 0.43 m
[115]	Foot	IMU	6 DoF IMU	RazorIMU	ZUPT+ EKF	300 m	Office Room	3D	Straight+ Turn	Percentage Error: 0.5 %
[116]	Foot	IMU	6 DoF IMU	MicroStrain 3DM-GX3-25	ZUPT+ KF	$\sim$ 97.3 m	Around building	3D	Loop	End Error: $0.05^\circ/s$
[117]	Hand / Pocket	IMU+ RGB-D	9 DoF IMU	Smart Phone	SLAM+ SURF+ RANSAC	-	Office Room	2D	Straight	Mean Error: 2.32 m

⋆ In test type, straight walking is labelled as straight, studies focusing on turning are labelled as turning, looping experiments are labelled as looping, experiments involving going up and down stair are labelled as stairs, and finally, if all of the above situations appear in one experiment, it is labelled as complex.

TABLE 2 – Comparison of Wearable Inertial Navigation Systems for Indoor Positioning

No.	Body parts	Signal type	IMU Type	IMU From	Algorithm	Path length	Testbed Type ⋆	2D/3D	Path type	Performance metric (value)
[62]	Foot	IMU	6 DoF IMU	ICM-20948, ICM-20649, ADXL375	ZUPT+ EKF	87.8 m	Office Room	3D	Straight	Percentage Error: 8.8 %
[118]	Foot	IMU	6 DoF IMU	ICM20948	FB-RTS+ ESKF+ RTS smoother	2,760 m	School	3D	Straight	ATE: 4.77 m
[119]	Foot	IMU	9 DoF IMU	Bosch BM1270	SINS+ ZUPT-KF	1,400 m	School	3D	Loop	Percentage Error: 0.36 %
[120]	Hand+ Waist	IMU	9 DoF IMU	Smart Phone	SHS+ PF	$\sim$ 234 m	Office Room	2D	Straight+ Turn	ATE: 2.5 m
[121]	Toe+ Heel+ Shank	IMU	9 DoF IMU	ICM20948 MIMU	ZUPT+ MAHONY+ Linear KF	340 m	Office Room	3D	Loop	Mean Error: 2.252 m
[122]	Hand / Pocket	IMU	9 DoF IMU	Sysnav MIMU	VINS	$\sim$ 380 m	Building	3D	Loop+ Stair	Percentage Error: 0.76 %
[123]	Head+ + Wrist	IMU+ RGB-D	6 DoF IMU	CH6 DoF IMU	FSS+ Visuo-inertial fusion+ ZNCC	$\sim$ 10 m	Office Room	2D	Straight	Cumulative Error: 0.15 m
[124]	Forearms+ Lower legs+ Head+ Pelvis	IMU+ RGB	6 DoF IMU	Xsens Dot	EgoLocate+ KF	143 m	Office Room	3D	Loop+ Stair	ATE: 0.22 m, 0.26 m
[30]	Hand / Pocket	IMU+ + WiFi	9 DoF IMU	Smart Phone	PDR+ WPL+ LKF	168 m	Office Room	2D	Loop	ATE: 1.45 m
[125]	Waist	IMU	6 DoF IMU+ Barometer	-	Bayesian Network	$\sim$ 15 m	Stairs	3D	Stair	Percentage Error: 0.41 %
[126]	Hand / Pocket	IMU+ WiFi	9 DoF IMU	Smart Phone	PDR+ Trilateration+ KF	$\sim$ 127 m	Corridor	2D	Loop	Mean Error: 1.6 m
[127]	Hand / Pocket	IMU	9 DoF IMU	Smart Phone	PDR+ KF	$\sim$ 127 m	Corridor	2D	Loop	Mean Error: 0.94 m
[46]	Hand / Pocket	IMU	6 DoF IMU	-	PDR	$\sim$ 20 m	Office Room	2D	Loop	ATE: 0.474 m
[128]	Hand / Pocket	IMU	9 DoF IMU+ Barometer	Smart Phone	PDR+ KNN+ LSTM+ KF+ CF	600 m	University Building	3D	Stair	ATE: 0.64 m
[63]	Chest	IMU+ WiFi	9 DoF IMU	Smart Phone	MLP+ PDR+ AEKF	22.4 m	University corridor	2D	Straight	ATE: 0.763 m
[129]	Foot	IMU	6 DoF IMU	X-SENS DOT	ZUPT+ ESFIR	$\sim$ 34 m	School Road	2D	Straight	ATE: 1.217 m
[130]	Lower back	IMU	6 DoF IMU	Xsens MTi-G-710	SHS+ Dempster-Shafer Theory	363.87 m	Office Room	2D	Straight	Percentage Error: 8 %

⋆ In test type, straight walking is labelled as straight, studies focusing on turning are labelled as turning, looping experiments are labelled as looping, experiments involving going up and down stair are labelled as stairs, and finally, if all of the above situations appear in one experiment, it is labelled as complex.

TABLE 2 – Comparison of Wearable Inertial Navigation Systems for Indoor Positioning

No.	Body parts	Signal type	IMU Type	IMU From	Algorithm	Path length	Testbed Type ⋆	2D/3D	Path type	Performance metric (value)
[32]	Hand / Pocket	IMU+ BLE	9 DoF IMU	Smart Phone	PDR+ BLE Ranging+ OMPF	202.50 m	Office Room	2D	Loop	Mean Error: 0.76 m
[131]	Hand / Pocket	IMU	9 DoF IMU	Smart Phone	PDR+ + KF	84 m	Office Room	2D	Straight	Mean Error: 0.67 m
[132]	Foot	IMU	9 DoF IMU	MTi-G-710	PINS-ZUPT+ ICCP+ KF	140 m	Stadium	2D	Loop	Mean Error: 0.25 m
[133]	Hand / Pocket	IMU	6 DoF IMU	Smart Phone	PDR+ LOESS+ BOCD	650 m	Office Room	2D	Loop	Mean Error: 2.28 m
[134]	Wrist	IMU	3DOF	MPU9250	Geomagnetic Positioning+ KF	-	Office Room	2D	Straight	ATE: 0.32 m
[5]	Hand / Pocket	IMU+ BLE	9 DoF IMU	Smart Phone	IPDR+ Multipoint Positioning+ KF	$\sim$ 160 m	Parking Garage	2D	Straight+ Turn	Real-time Error: 2.66 m
[135]	Hand / Pocket	IMU+ WiFi	9 DoF IMU	Google Pixel 2	PDR+ FF+ Smoothing	$\sim$ 18 m	Corridor	2D	Straight+ Turn	Mean Error: 0.719 m
[31]	Hand / Pocket	IMU+ WiFi	9 DoF IMU	Smart Phone	AWFP+ PDR+ Tightly-coupled EKF	$\sim$ 20 m	Office Room	2D	Straight+ Turn	ATE: 1.10 m
[34]	Hand / Pocket	IMU+ BLE	9 DoF IMU	Smart Phone	AoA+ RSS-based ranging+ PDR+ KF	$\sim$ 30 m	Office Room	2D	Loop	Mean Error: 0.48 m
[136]	Hand / Pocket	IMU+ WiFi	9 DoF IMU	STMicroelectronics LSM6DS3	DNN+ Weight Fusion	$\sim$ 87 m	Office Room	2D	Loop	Mean Error: 0.18 m
[137]	Foot	IMU+ UWB	9 DoF IMU	BNO055	ZUPT+ ILCKF	110 m	Office Room	3D	-	ATE: 0.29 m
[138]	Arm	IMU	6 DoF IMU	-	Projection Estimate+ ECF	-	Class Room	2D	Straight	ATE: 0.03 m
[139]	Foot	IMU	6 DoF IMU	XSENS MTI-1s-DEV	ZUPT+ KF	1,274 m	Class Room	2D	Straight	ATE: 0.05 m
[11]	Head+ Arm+ Back+ Foot+ Thigh	IMU+ RGB-D	6 DoF IMU	Movella IMU	IMUNet (Deep Learning)+ Cross-Attention	-	Office Room	2D	Straight	End Error: 1.3 %
[140]	Hand / Pocket	IMU+ RGB	6 DoF IMU	Smart Phone	Sliding-window filter+ Square-root inverse filter	200 m	Office Room	3D	Straight	ATE: 0.2 m
[141]	Hand / Pocket	IMU	6 DoF IMU	Smart Phone	TAFI	21,910 m	Office Room	3D	-	ATE: 1.47 m

⋆ In test type, straight walking is labelled as straight, studies focusing on turning are labelled as turning, looping experiments are labelled as looping, experiments involving going up and down stair are labelled as stairs, and finally, if all of the above situations appear in one experiment, it is labelled as complex.

TABLE 2 – Comparison of Wearable Inertial Navigation Systems for Indoor Positioning

No.	Body parts	Signal type	IMU Type	IMU From	Algorithm	Path length	Testbed Type ⋆	2D/3D	Path type	Performance metric (value)
[36]	Waist	IMU+ BLE	6 DoF IMU	Yost 3-Space Data Logger	Adaptive Trilateration+ PDR+ Average Fusion	$\sim$ 120 m	Corridor	2D	Straight	ATE: 3.9 m
[142]	Hand / Pocket	IMU	6 DoF IMU	Smart Phone	Neural Network (Linear Layers)	$\sim$ 200 m	Office Room	2D	Loop	ATE: 0.47 m
[143]	Waist	IMU	6 DoF IMU	Xsens MTi-G-700	PDR+ KF	1300 m	School Building	2D	Straight	Rate Error: 0.41 %
[67]	Head+ Waist	IMU+ RGB	9 DoF IMU	VectorNav	OpenVSLAM	966 m	Urban Road	3D	Straight	End Error: 2.3°
[144]	Hand / Pocket	IMU+ RGB-D	9 DoF IMU	VN100	DVIO+ Graph optimisation	110 m	Hall	2D	Straight	ATE: 0.17 m
[12]	Hand / Pocket	IMU+ RGB-D	9 DoF IMU	VN100	DVIO+ PFL+ Graph optimisation	180 m	Office Room	3D	Straight	ATE: 0.12 m
[145]	-	IMU+ TWR+ WiFi	6 DoF IMU	MPU6050	ZUPT+ UWB+ ILCKF	$\sim$ 14 m	office room	2D	Loop	ATE: 0.24 m
[146]	-	IMU+ WiFi	6 DoF IMU	Smart Phone	WIO-EKF	-	Office room	2D	Straight+ Turn	Mean Error: 2.53 m
[147]	-	IMU	6 DoF IMU	Smart Phone+ Xsens MTi-G	PDR	$\sim$ 550 m	Office room	2D	Straight+ Loop	Percentage Error: 0.9 %
[148]	-	IMU	6 DoF IMU	Xsens Dot	ROCIP (DenseNet+ RBPF)+ RBPF	-	Corridor	3D	Complex	ATE: 4.36 m
[149]	-	IMU+ BLE	9 DoF IMU	Smart Phone	MCPD+ PDR+ Madgwick filter	8 m	School Road, Roof	2D	Complex	Percentage Error: 9 %
[7]	-	IMU+ UWB	9 DoF IMU	STM32	AUM+ DOP+ EKF/UKF	-	Office room	2D	Straight + Turn	Cumulative Error: 0.05 m
[150]	-	IMU+ RGB-D+ WiFi	9 DoF IMU	Smart Phone	SfM	$\sim$ 10 m	Supermarket	3D	-	Cumulative Error: $\sim$ 2.69 m
[151]	-	IMU+ RGB-D	6 DoF IMU	XSENS MTI-100, MTI-g710, ADIS16448 IMU	MSCKF+ EKF	143 m	Office Room	3D	-	End-pose Error: 0.35 m
[9]	-	IMU+ UWB	6 DoF IMU	ICM-40607 (IMU)	WNLS+ TDOA/AOA+ TC ESKF	-	Office Room	3D	Complex	ATE: 0.132 m

⋆ In test type, straight walking is labelled as straight, studies focusing on turning are labelled as turning, looping experiments are labelled as looping, experiments involving going up and down stair are labelled as stairs, and finally, if all of the above situations appear in one experiment, it is labelled as complex.

TABLE 2 – Comparison of Wearable Inertial Navigation Systems for Indoor Positioning

No.	Body parts	Signal type	IMU Type	IMU From	Algorithm	Path length	Testbed Type ⋆	2D/3D	Path type	Performance metric (value)
[152]	-	IMU+ UWB	9 DoF IMU	ICM-20948	ZUPT+ PDR+ DS-TWR+ Trilateral position+ EKF+ UKF	275.8 m	Office Room	3D	Complex	ATE: 0.136 m
[153]	-	IMU+ RGB-D	9 DoF IMU	-	AA-DP+ MLE-HP	$\sim$ 1.2 m	Office Room	2D	Complex	Mean Error: $\sim$ 0.02 m
[154]	-	IMU+ UWB	9 DoF IMU	-	DAPA-EKF+ LS-AEKF+ EKF	-	Office Room	2D	Straight	ATE: $\sim$ 0.01 m
[155]	-	IMU+ RGB	6 DoF IMU	ADIS16448	UKF+ UKF-VIN	75.9 m	Machine hall	3D	Complex	ATE: $\sim$ 0.25 m
[156]	-	IMU	9 DoF IMU	Smart Phone	PDR+ PDRSV	$\sim$ 12.5 m	School Road	2D	Straight+ Turn	Mean Error: 1.25 m
[157]	-	IMU+ UWB+ MAG	6 DoF IMU	MPU9250	TOA+ PDR+ GA-based matching+ GA+ IREKF	-	Parking Garage	2D	Straight	ATE: 0.55 m
[158]	-	IMU+ UWB	6 DoF IMU	-	Resettable Residual Weighted PF+ Hybrid EKF/WUFIR	$\sim$ 220 m	Office Room	3D	Straight	ATE: 0.322 m
[159]	-	IMU+ UWB	9 DoF IMU	DETA10	PF-SI / ESKF-SI+ Bayesian Fusion	-	Office Room	2D	Straight	ATE: 0.18 m
[10]	-	IMU+ UWB	9 DoF IMU	MPU_6050	NLOS+ Weighted Fusion	-	Office Room	2D	Straight	ATE: 0.1 m

⋆ In path type, straight walking is labelled as straight, studies focusing on turning are labelled as turning, looping experiments are labelled as looping, experiments involving going up and down stair are labelled as stairs, and finally, if all of the above situations appear in one experiment, it is labelled as complex.

III. Performance Analysis

To enable a detailed and systematic comparison of existing wearable inertial navigation systems, this study provides a comprehensive tabular overview of relevant devices and methods (see Table 2). The review is based on a broad and carefully conducted manual extraction process that consolidates key information reported in the literature. Each study is categorised using a unified set of criteria, including body parts, signal type, IMU type, IMU from, algorithm, path length, testbed types, dimensionality (2D/3D), path types, performance, and error types. Here, body parts refer to the specific area of the body where the IMU is worn. Organising the evidence in this way enables transparent cross-study comparison and highlights methodological trends, sensor configuration differences, and variations in reported performance.

This extraction and synthesis process also faces several methodological challenges. These include incomplete reporting of experimental parameters, difficulty in extracting quantitative values from figures, and inconsistent reporting standards across studies.

This section first introduce the most commonly used evaluation metrics utilised in the literature. It then analyses the literature from five key perspectives: IMU type, sensor modality, body location, algorithm method, and other influencing factors. The goal is to identify current trends in wearable inertial navigation research (shown in Fig. 8). These dimensions are chosen because they have a fundamental impact on system performance and design feasibility. Specifically, different body placements experience varying levels of motion complexity, sensor drift, and biomechanical interference. These factors directly affect positioning accuracy. The choice of IMU type and sensor modality further influences measurement precision. In addition, positioning algorithms directly determine the accuracy and robustness of trajectory estimation. Algorithm comparison is essential for understanding performance differences among implementations. Other environmental factors also affect the final positioning accuracy. Finally, this chapter summarises how these factors jointly influence localisation performance.

A. Evaluation metric

This section introduces the most common used evaluation metrics applied to wearable inertial navigation performance, including ATE (Absolute Trajectory Error), cumulative error, end-pose error, heading error, mean error, percentage error, rate, real time error, circular error and RPE (Relative Pose Error).

1) Absolute Trajectory Error (ATE)

For positioning and navigation systems, evaluating the accuracy of trajectory estimation is of paramount importance. Absolute Trajectory Error (ATE) represents a widely adopted metric for measuring the global consistency between estimated and ground truth trajectories, emphasising the absolute positional deviations across the entire path rather than relative motion errors between consecutive poses. In essence, ATE quantifies the overall system performance within a global coordinate frame by computing the mean Euclidean distance of positional errors at each temporal sample, thereby facilitating the identification of systematic drift or accumulated errors over time. Its mathematical formulation is expressed as:

$$ATE = \frac{1}{k}\sum_{t=0}^{k} ||P^{GT}(t) - P^{n}(t)|| \tag{33}$$

where $P^{GT}(t)$ represents the ground truth position, $P^{n}(t)$ represents the navigation position. Because the ATE uses the point to record position, the time is equal to the total number of trajectory points, represented by k, and is from 1. Its unit usually is metres (m).

In practical positioning and navigation applications, such as indoor localisation systems, ATE serves as a standard benchmark for comparing trajectory estimation accuracy across disparate algorithmic approaches including vision-based, laser-based, or inertial measurement unit (IMU)-based methods thereby informing optimal system design. However, a significant methodological challenge arises: directly computing ATE may introduce substantial bias owing to potential inconsistencies in the initial position, orientation, and scale between the estimated and reference trajectories. Consequently, it is typically necessary to first register the estimated trajectory to the ground truth coordinate system through least-squares alignment techniques, such as SE(3) transformation (rigid body transformation in three-dimensional space). This standardised evaluation procedure ensures equitable comparison of diverse positioning systems' performance characteristics and enables the derivation of generalised analytical expressions that guide systematic algorithm refinement and enhancement.

2) Cumulative Error

Accumulated error represents a fundamental challenge in navigation and positioning systems, arising primarily from sensor measurement noise and bias that compound progressively during the integration process. Over extended operational periods, these errors propagate systematically, causing the estimated trajectory to diverge increasingly from the true path. To quantify this divergence, the accumulated error is conventionally computed by summing the Euclidean distance between the ground truth position and the estimated position at each discrete time step, expressed as:

$$\text{Cumulative Error} = \sum_{t=0}^{k} ||P^{GT}(t) - P^{n}(t)|| \tag{34}$$

and basically its unit is metres (m).

This cumulative metric effectively captures the temporal growth of positional drift, thereby providing critical insight into long-term navigation stability. The principal technical challenge lies in mitigating this unbounded error growth

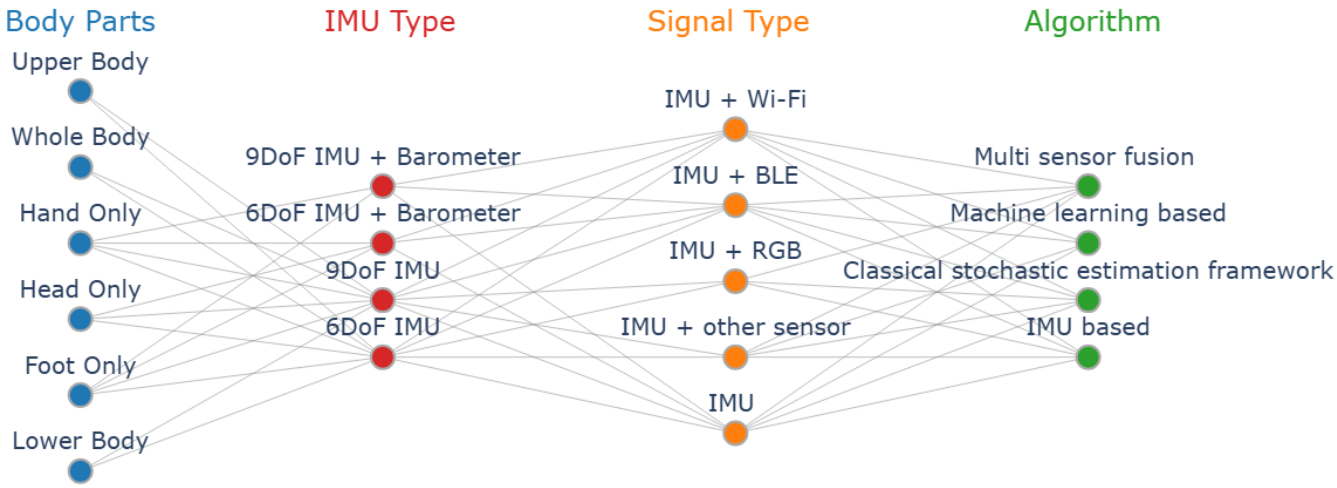

FIGURE 8. **In this review, the included studies are organised according to four analytical dimensions: body part, IMU type, signal type, and algorithmic approach. These dimensions are not newly proposed taxonomies; rather, they represent the most commonly reported methodological descriptors across the literature and thus provide a coherent basis for comparison. Body part refers to the anatomical location where IMUs are mounted, encompassing both single-region and multi-region configurations. IMU type denotes the specific sensing hardware used in each study, including accelerometers, gyroscopes, magnetometers, or their combinations within an IMU. Signal type captures the modality or combination of modalities extracted from the IMU such as raw acceleration, angular velocity, orientation estimates, or derived features. Finally, algorithm refers to the computational method applied to these signals, ranging from classical machine-learning techniques to deep-learning architectures.**

through sophisticated sensor fusion architectures or periodic measurement updates.

In contemporary navigation research, accumulated error serves as the paramount evaluation criterion, as it directly reflects both the stability and reliability of positioning systems under realistic operational conditions. To facilitate rigorous comparative analysis amongst competing navigation methodologies, accumulated error is typically adopted as the key performance indicator, with particular attention devoted to characterising its temporal behaviour across both short-term and extended operational intervals. This evaluation framework not only enables objective benchmarking of algorithmic performance but also illuminates systematic pathways for optimisation in navigation algorithm design and system architecture development.

3) End-pose Error

In navigation systems, the primary objective is to continuously estimate an object's motion using sensor measurements. However, sensor drift and the accumulation of systematic errors inevitably cause the estimated trajectory to deviate progressively from the ground truth over time. To quantify the absolute accuracy of a loop-based navigation system at a specific temporal instant or upon completion of a task, researchers conventionally employ the end-pose error as a principal evaluation metric.

The rationale underpinning this metric is conceptually straightforward: it establishes a direct comparison between the system's estimated pose $P^n(k)$ and the ground-truth pose $P^{GT}(k)$ at the identical time step k. Mathematically, the end-pose error is expressed as:

$$\text{End-pose Error} = ||P^{GT}(k) - P^n(k)|| \tag{35}$$

Usually its unit is metres (m). However, there is a special case, in [57] the unit is pixel.

The resulting scalar value quantifies the instantaneous accuracy of the system at that particular moment. Within navigation research and practical applications, the end-pose error serves a critical function. The fundamental challenge lies in the fact that disparate navigation algorithms or sensor-fusion methodologies accumulate errors through distinct temporal patterns: certain approaches may exhibit stability during initial phases whilst manifesting pronounced drift towards completion, whereas others may demonstrate oscillatory behaviour along the trajectory yet converge closer to the true terminal position. By establishing a common reference point such as the terminus of a planned route or the completion of a designated mission the end-pose error furnishes a unified and objective criterion for comparing the terminal accuracy of competing systems.

Consequently, numerous investigations adopt the end-pose error as a primary performance indicator. Cross-method comparisons of this metric facilitate the identification of navigation approaches that deliver superior final accuracy, thereby enabling informed selection amongst alternative algorithmic implementations.

4) Heading Error

In inertial navigation systems, heading error constitutes a critical metric for evaluating the accuracy of directional estimation and enhancing overall system reliability. Defined as the angular deviation between the estimated heading and the true heading, this parameter serves as a fundamental performance indicator for directional sensors, including gyroscopes and magnetometers. The heading error is quantified

through the following expression:

$$\text{Heading Error} = \sqrt{2 \cdot (1 - \cos(\Delta\varphi))} \tag{36}$$

where $\Delta\varphi$ represents the angular difference in radians. The unit of Heading Error typically is degree($^\circ$) or degree per second ($^\circ/s$), and sometimes it will be the percentage ($\%$). This formulation, derived from the cosine rule in vector geometry, effectively captures the magnitude of directional deviation and provides a geometrically intuitive measure of orientation discrepancy.

Within navigation applications, heading error analysis plays a pivotal role in several key areas, including INS calibration and multi-sensor integration frameworks. These implementations aim to mitigate accumulated drift and enhance trajectory precision. However, significant challenges persist, as heading error exhibits temporal drift characteristics attributable to sensor noise, environmental perturbations most notably magnetic disturbances and complex motion dynamics. Such factors collectively compromise system stability and necessitate robust error compensation strategies. The error norm serves as the primary evaluation metric in contemporary research, with the aforementioned formula providing a standardised framework for assessing directional estimation performance across heterogeneous navigation systems. To ensure methodological rigour and facilitate meaningful inter-system comparisons, the standard evaluation protocol involves initial characterisation under static conditions, followed by comprehensive testing in dynamic scenarios. This two-stage approach enables systematic verification of algorithm robustness and ensures reliable performance across diverse operational environments.

5) Mean Error

In navigation systems, the evaluation of localisation algorithms predominantly centres on the average accuracy of overall position estimates. Mean Error, which quantifies the average absolute difference between the estimated position and the ground truth position, serves as a fundamental metric for assessing the performance of positioning models and filtering methods across entire trajectories. This metric is formally defined as:

$$\text{Mean Error} = \frac{1}{N}\sum_{n=1}^{N}\frac{1}{k_{\max}}\sum_{k=0}^{k_{\max}}||y_{n,k} - f_n(X_{n,k})|| \tag{37}$$

where N denotes the number of trajectories, k_{max} represents the number of time steps in each trajectory, $y_{(n,k)}$ indicates the true position of the n-th trajectory at time k, and $f_n(X_{n,k})$ corresponds to the model prediction. Basically mean error unit is metres (m) or metres per second (m/s). By averaging the absolute errors across all trajectories and temporal steps, this formulation yields a stable and comprehensive measure of the system's overall error magnitude.

The application of Mean Error is widespread across diverse navigation technologies, including WiFi and Bluetooth fingerprinting, visual SLAM, and INS trajectory estimation. It constitutes one of the principal indicators for evaluating algorithm robustness and reliability. Nevertheless, a significant limitation emerges from the averaging nature of this metric: it may obscure substantial localised errors within trajectories, such as abrupt large deviations at specific way points. Consequently, Mean Error is typically employed in conjunction with complementary metrics such as maximum error or root-mean-square error to furnish a comprehensive performance assessment. In related studies, mean absolute error remains the predominant evaluation metric, and this standardised formulation facilitates unified comparisons across disparate positioning systems. To ensure rigorous and equitable comparisons, standard practice involves evaluating Mean Error against known reference trajectories, followed by systematic analysis of algorithmic behaviour under varying movement velocities and environmental conditions, thereby confirming the algorithm's applicability across diverse operational scenarios.

6) Percentage Error

In navigation systems, Percentage Error serves as a fundamental metric for evaluating the overall accuracy of position estimates, proving particularly valuable in long-distance trajectory tracking applications. This metric quantifies the extent to which accumulated positional error grows relative to the total distance travelled, thereby providing insight into the drift characteristics of inertial navigation systems over extended operational periods. By normalising the absolute positional error against a reference displacement quantity, Percentage Error effectively eliminates the influence of trajectory scale variations, thereby enabling meaningful performance comparisons across disparate operational scenarios and test conditions. The mathematical formulation of Percentage Error is expressed as:

$$\text{Percentage Error} = \frac{\sum_0^k ||P^{GT}(k) - P^n(k)||}{||P^{GT}(k) - P^{GT}(0)||} \tag{38}$$

This formulation yields a dimensionless quantity that characterises the average positional deviation per unit of travelled distance, thus establishing a scale-independent accuracy measure that facilitates cross-scenario performance assessment. Therefore, its unit normally is percentage ($\%$).

Despite its utility, this metric presents notable computational challenges that warrant careful consideration. The primary limitation concerns the zero-denominator problem: when the object remains stationary or traverses only minimal distances, the reference displacement approaches zero, rendering the error calculation mathematically undefined or numerically unstable. Furthermore, the cumulative summation structure in the numerator implies that positioning errors incurred during early trajectory segments continue to influence subsequent evaluation results, potentially obscuring performance variations over time. To ensure valid and meaningful assessment, experimental trajectories must therefore incorporate sufficient displacement distances. Advanced computational strategies, such as sliding-window implementations, may be employed to mitigate cumulative error

effects and provide more localised accuracy characterisation. In practical applications, researchers typically establish minimum threshold criteria for denominator displacement values and subsequently compare the Percentage Error of competing algorithms under standardised trajectory conditions, thereby enabling objective evaluation of navigation system stability and reliability throughout prolonged operational missions.

7) Rate Error

In positioning and navigation systems, accurate rate estimation is essential for characterising motion states and predicting trajectories. Rate Error quantifies the discrepancy between the estimated rate and the true rate, serving as a fundamental metric for evaluating the velocity-measurement performance of an INS. The mathematical formulation is expressed as

$$\text{Rate Error} = \frac{||P^{GT}(k) - P^{n}(k)||}{\Delta k} \tag{39}$$

where Δk represents the time from the last time stamp to next one. For most research, the unit of Rate Error is metres per seconds (m/s). This metric quantifies the displacement deviation per unit time, thereby characterising the temporal propagation of position error.

Within navigation applications, Rate Error plays a pivotal role in INS velocity calibration and in refining the dynamic models of mobile platforms. By continuously monitoring variations in Rate Error, the system can adapt sensor-fusion weights in real time, thereby mitigating the long-term effects of velocity drift on positioning accuracy. Nevertheless, this metric confronts several fundamental challenges: inherent bias instability in inertial sensors, coupled noise from accelerometers and gyroscopes, and dynamic errors induced by platform manoeuvres. These issues become particularly pronounced during extended navigation operations, where accumulating Rate Error can directly precipitate divergence in position estimation.

Contemporary research commonly employs Rate Error as a principal indicator of navigation stability, with this formulation providing a standardised framework for comparing velocity-estimation performance across different algorithmic approaches. To comprehensively assess system robustness, Rate Error is typically evaluated initially under idealised conditions such as constant-velocity or rectilinear motion before being analysed under dynamic scenarios involving acceleration or turning manoeuvres, thereby ensuring reliable rate estimation across diverse motion states.

8) Real-time Error

In positioning and navigation systems, research on real time error typically focuses on the instantaneous accuracy of position estimates to enhance real time performance and system reliability. Real-time error quantifies the two-dimensional Euclidean distance between the estimated position and the ground truth position at a specific time instant k, thereby directly characterising the absolute positional deviation of the algorithm or sensor at that moment. The metric is formally defined as:

$$\text{Real-time Error} = \sqrt{(x(k) - \hat{x}(k))^2 + (y(k) - \hat{y}(k))^2} \tag{40}$$

where $(x(k), y(k))$ denotes the true coordinates at time k, and $(\hat{x}(k), \hat{y}(k))$ represents the navigation coordinates. Generally, its unit is metres (m). By computing the straight-line distance between these two points, this formulation provides a clear and direct measure of positional deviation magnitude.

Within navigation applications, real time error serves multiple critical functions: it facilitates online performance evaluation, supports loop-closure validation in SLAM frameworks, and informs the update step in recursive filtering schemes such as the Kalman filter. By providing immediate feedback, it enables dynamic adjustment of positioning estimates. Nevertheless, a fundamental challenge persists: the ground truth position ($(x(k), y(k))$ is typically unavailable in operational scenarios and must be approximated using high-precision reference systems, such as real time kinematic global positioning systems or motion-capture configurations. These approximations may themselves introduce additional uncertainties that must be carefully considered.

The error norm constitutes the principal evaluation metric in related studies, and this formulation permits direct measurement of positioning accuracy at any given instant. For comprehensive system assessment, it is essential to first analyse the instantaneous distribution and peak values of real time error, and subsequently examine its statistical characteristics across the entire trajectory including mean, variance, and temporal trends to evaluate both the real time performance and the stability of the navigation system over extended operation.

9) Circular Error Probable (CEP)

In navigation systems, research on positioning accuracy typically concentrates on quantifying the proximity between estimated positions and true locations, thereby facilitating comprehensive performance evaluation. The CEP serves as a fundamental metric for characterising two-dimensional positioning accuracy. Formally, CEP defines the radius of a circle centred on either the true or estimated position within which 50 % of all position estimates are expected to lie. The relationship between positioning error and probability level is expressed as:

$$\text{CEP} = \sigma \cdot \sqrt{2 \cdot \ln\left(\frac{1}{C}\right)} \tag{41}$$

where σ represents the standard deviation of positioning error along two orthogonal directions (typically assuming independent and identically distributed errors), and C denotes the desired probability level (conventionally set to 0.5 for CEP). Typically, the unit of CEP is metres (m). This formulation derives from the properties of the Rayleigh

distribution and provides an intuitive transformation from the error standard deviation to an accuracy radius with probabilistic interpretation.

Within navigation applications, CEP is extensively employed to benchmark the accuracy performance of different IMUs and serves as an optimisation objective in multi-sensor fusion filters, thereby enhancing the reliability of position estimates. Nevertheless, a principal limitation arises from the metric's dependence on idealised assumptions specifically, that positioning errors adhere to a normal, isotropic distribution. In practical environments characterised by urban canyons or pronounced multi-path propagation, the error distribution frequently deviates from these assumptions, rendering CEP an incomplete representation of actual positioning performance. The primary evaluation methodology in related literature centres on statistical characterisation of positioning error distributions, with this formula providing a standardised framework for expressing accuracy at specified confidence levels. To ensure rigorous comparative analysis, researchers typically conduct initial CEP assessments in minimally obstructed environments with negligible interference, subsequently examining performance degradation in increasingly challenging scenarios such as regions with significant obstacles or electromagnetic disturbances to comprehensively evaluate the applicability and robustness of navigation solutions across diverse operational conditions.

10) Relative Pose Error (RPE)

In addition to the metrics described above, Relative Pose Error (RPE) provides a complementary perspective that is particularly relevant when comparing systems evaluated over trajectories of substantially different lengths. Whilst ATE captures the global deviation of an estimated trajectory from the ground truth, it does not account for the distance over which that error accumulates; longer paths naturally produce greater absolute drift, which can bias cross-study comparisons. Relative Pose Error (RPE) addresses this limitation by quantifying the translational drift as a proportion of the distance travelled over fixed-length sub-trajectories, thereby providing a scale-independent measure of local navigation consistency. To define RPE, let $\mathbf{e}(t)$ denote the relative translational error over a sub-trajectory of length δ starting at time step t:

$$\mathbf{e}(t) = \big(P_{GT}(t+\delta) - P_{GT}(t)\big) - \big(P_n(t+\delta) - P_n(t)\big) \quad (42)$$

where $P_{GT}(t)$ and $P_n(t)$ denote the ground truth and estimated positions at time step t, respectively. The parameter δ represents a fixed sub-trajectory interval measured in time steps. RPE is then defined as the mean of the normalised translational errors across all M sub-trajectory segments:

$$RPE = \frac{1}{M}\sum_{t=1}^{M} \frac{\|\mathbf{e}(t)\|}{\|P_{GT}(t+\delta) - P_{GT}(t)\|} \quad (43)$$

The denominator normalises each segment's error by the corresponding ground truth displacement. By evaluating drift over fixed-length segments rather than across the entire trajectory, RPE effectively decouples positioning accuracy from path length, thereby enabling equitable comparison of systems tested under differing trajectory scales. This property renders RPE particularly suitable for benchmarking inertial navigation systems, where drift accumulation is the predominant error source and path lengths vary considerably across experimental configurations.

It is worth noting the relationship between RPE and the Percentage Error. Both metrics normalise positional error by the distance travelled; however, they differ in granularity. Percentage Error computes a single cumulative ratio over the entire trajectory, making it sensitive to early-stage errors that propagate into later evaluations. RPE, by contrast, averages over M fixed-length sub-trajectory windows of size δ, providing a more localised and robust characterisation of drift behaviour that is less susceptible to error accumulation artefacts. When δ equals the full trajectory length and only a single segment is evaluated ($M = 1$), RPE reduces to a form analogous to Percentage Error.

It should also be noted that the RPE values presented in the analysis were manually derived from data reported in the original studies, as the majority of papers do not explicitly provide this metric.

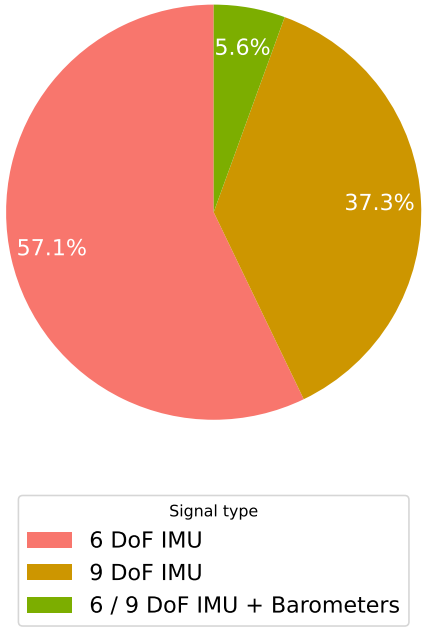

FIGURE 9. Distribution of different types of IMU used in the included studies. It is observed that the 6 DoF IMU is the most commonly used type in the literature.

B. The impact of IMU sensor types

This section reviews the impact of distinct IMU sensor configurations specifically 6 DoF, 9 DoF, and barometer-augmented systems on positioning accuracy. By analysing the relationship between sensor complexity and performance,

this review elucidates the trade-offs between hardware complexity, computational demand, and localisation precision to inform sensor selection for pedestrian navigation applications.

Systems employing 6 DoF IMUs represent the most widely adopted configuration, accounting for 57.1 % of reported applications (shown as Figure 9). This ubiquity stems from their low cost and minimal computational requirements, which allow for sufficient accuracy across various scenarios. In controlled environments, 6 DoF systems demonstrate submeter precision: for instance, achieving an ATE of 0.193 m over a 185 m warehouse trajectory [111], a cumulative error of 0.209 m in a multi-story laboratory route [77], and an ATE of 0.47 m on a 200 m office loop [142]. However, error increases significantly in longer and less structured environments; a complex 2,000 m stadium path resulted in a cumulative error of 19.77 m [53], while a straight office path exhibited a drift of 2.5 m [28]. Across all reviewed studies, systems relying solely on 6 DoF sensors exhibited an average ATE of 1.80 m, the highest among the three configurations (shown as Figure 10). This deficiency primarily arises from the lack of an absolute heading reference, as reliance on gyroscope integration inevitably leads to accumulated rotational drift. Nevertheless, in indoor environments with severe magnetic interference, 6 DoF configurations may outperform 9 DoF alternatives by avoiding the performance degradation associated with unreliable magnetometer readings.

9 DoF configurations incorporate tri-axis magnetometers to provide absolute heading information, theoretically mitigating the impact of rotational drift on position estimation. Representing 37.3 % of reported applications, this configuration achieves an ATE of 0.77 m, a reduction of approximately 57 % compared to 6 DoF systems (shown as Figure 10). Performance is particularly prominent in magnetically stable environments: research reported an error of 0.36 % over a 1,400 m school loop [119], and error rates of 0.15 m/s and 0.11 m/s in 750 m urban road tests [95]. Similarly, favourable results are observed indoors where magnetic interference is minimal, with errors of 0.8 % on a 230 m office loop [72] and an ATE of 0.17 m along a 110 m corridor [144]. However, magnetometers are susceptible to interference from ferromagnetic materials and electrical equipment, which can degrade accuracy in complex indoor magnetic fields. Furthermore, 9 DoF systems entail higher hardware costs, greater computational complexity, and more stringent calibration requirements. Consequently, this configuration is more suitable for outdoor settings or stable indoor environments, whereas its advantages are limited and potentially detrimental in magnetically complex scenarios.

Beyond purely inertial configurations, a limited number of studies explored the integration of barometric sensors. Among the 124 papers reviewed in this study, only six use IMUs that include a barometer for inertial navigation. Systems equipped with barometers whether combined with 6 DoF or 9 DoF IMUs demonstrated an average ATE of 0.48 m, significantly lower than both 6 DoF (1.80 m) and 9 DoF (0.77 m) systems (shown as Figure 10). It is crucial to note, however, that this advantage is context-dependent: evaluations were predominantly conducted on short trajectories involving significant vertical motion, such as jumping, stair climbing, and multi-story navigation. Barometers provide direct altitude information to effectively suppress vertical drift. Research by [82] reported a cumulative error of 0.269 m in jump tracking, whilst [125] achieved 0.41 % error on a 15 m stair trajectory, and [128] reported an ATE of 0.64 m over a 600 m path involving stairs and elevators. Although [13] reported cumulative errors of 0.855 m over 190 m trajectories respectively, the focus remained on scenarios with distinct altitude changes. The limitation of these studies lies in the restricted scope of trajectory lengths and scenarios: while pure IMU systems suffer from drift accumulation due to the double integration of vertical acceleration, barometric sensing directly addresses this error source in height-dominant scenarios. However, for long-distance trajectories dominated by horizontal motion with minimal vertical displacement, the benefits of barometric augmentation remain ambiguous. The observed performance enhancement likely reflects task-specific advantages, necessitating further validation of its universal effectiveness across broader environments and extended trajectories.

In summary, the distribution of IMU configurations (57.1 % for 6 DoF, 37.3 % for 9 DoF, and 5.6 % for others) reflects practical considerations regarding sensor selection (shown as Figure 9). Although the average error of 9 DoF systems (0.77 m) is notably lower than that of 6 DoF systems (1.80 m) (shown as Figure 10), the latter is often prioritised due to low cost, computational simplicity, ease of calibration, and immunity to magnetic interference. In complex indoor environments common to pedestrian navigation, the theoretical benefits of magnetometer correction may not materialise or could even negatively impact performance. The present review of 124 articles reveals that only 6 with barometer inertial measurement units for navigation. While IMU with the barometer systems excel in scenarios with significant vertical motion, their limited application scope reflects their task-specific nature and practical deployment constraints. Therefore, optimal sensor configuration depends on the specific environment: 6 DoF IMUs suffice for magnetically complex or cost-sensitive scenarios; 9 DoF systems offer significant performance gains where magnetic fields are stable and heading accuracy is critical; and systems that incorporate barometers are best suited for applications that involve multi-floor navigation or large height changes. However, the surprisingly strong performance of barometric-augmented systems is based on a limited body of evidence, with only six studies included in this paper, all of which employ comparatively small testbeds. In practice, researchers must carefully balance performance requirements with practical factors such as real time capability, ease of deployment, environmental adaptability, and cost.

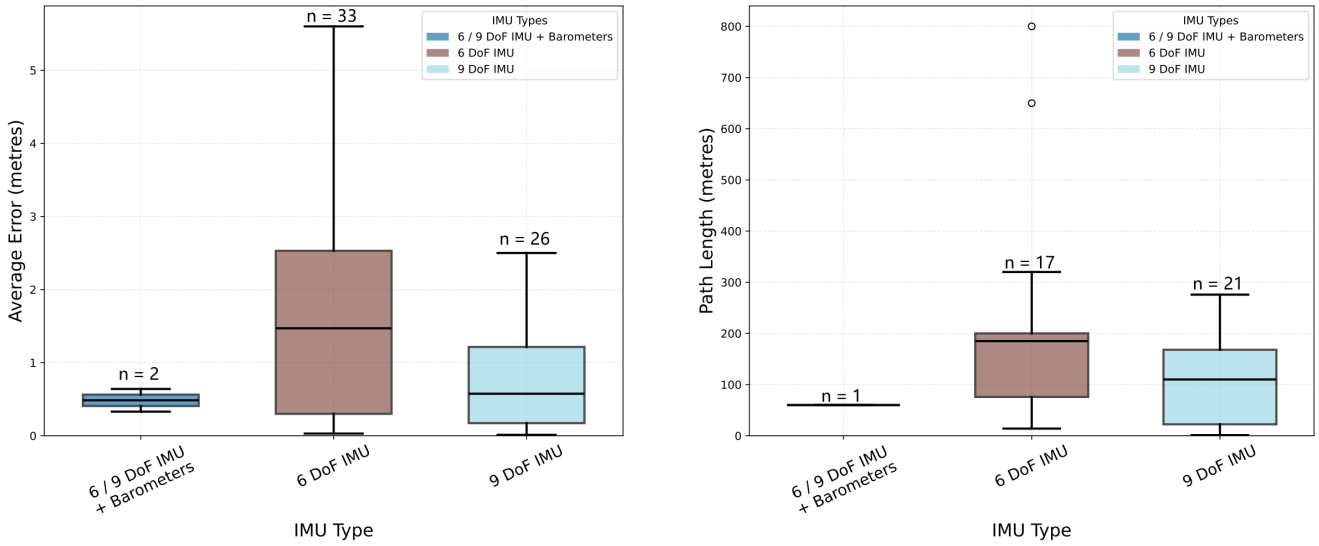

(a) Average Error by IMU Type

(b) Path Length by IMU Type

FIGURE 10. **The two box plots comparing (a) average positional error and (b) reconstructed path length for three IMU configurations: 6 DoF IMU, 6 / 9 DoF IMU with barometers, and 9 DoF IMU. The number above each box indicates the number of included studies (n). The boxes represent the interquartile range (IQR), the central line indicates the median, and whiskers denote the spread of the data, with individual points showing outliers where present. Due to substantial discrepancies in the data, we excluded data points with path lengths exceeding 1000 from the analysis. Overall, the 6 / 9 DoF IMU with barometers exhibits the lowest and most consistent error and path-length estimates, while the 6 DoF and 9 DoF IMUs show greater variability.**

C. Impact of IMU sensor placement on different body parts

The placement of wearable IMUs fundamentally influences system performance in indoor inertial navigation, as different anatomical locations exhibit distinct motion characteristics, signal quality, and susceptibility to disturbances. Consequently, this section systematically examines how sensor placement affects positioning accuracy by first establishing the distribution of mounting locations adopted in existing literature, then comparing representative studies across different body parts, and finally evaluating aggregated accuracy results to identify which placement strategies yield superior performance.

Analysis of the body placement distribution (see Figure 11) reveals that research efforts concentrate predominantly on hand-mounted sensors (35.5 %) and foot-mounted sensors (29.9 %), reflecting their accessibility and potential for practical deployment. Upper body and whole body configurations represent 14.0 % and 5.6 % of studies respectively, indicating growing interest in multi-sensor integration strategies. This distribution suggests that researchers prioritise body parts offering high-frequency motion patterns and robust signal characteristics to maximise the practical utility of inertial navigation systems.

Foot-mounted sensor systems demonstrate considerable variability in algorithmic performance across different path lengths and evaluation metrics. Research by [89] achieved a percentage error of 2.5 % over approximately 172 m, establishing a baseline for single-foot configurations. Build-

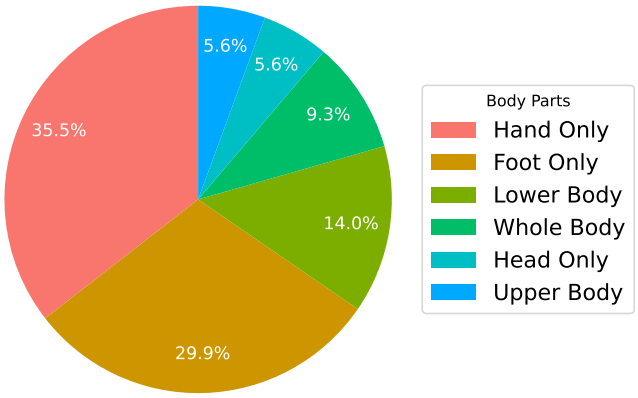

FIGURE 11. **The pie chart shows the proportion of different body parts used in localisation and motion estimation algorithm research. It illustrates the percentage of literature on sensor or method deployment on the hand, foot, lower body, whole body, head, and upper body. It can be seen that "hand only" and "foot only" account for the highest proportions, approximately 35.5 % and 29.9 % respectively, indicating that related research focuses more on motion capture of the hand and foot; while applications of the whole body, lower body, head, and upper body are relatively less common.**

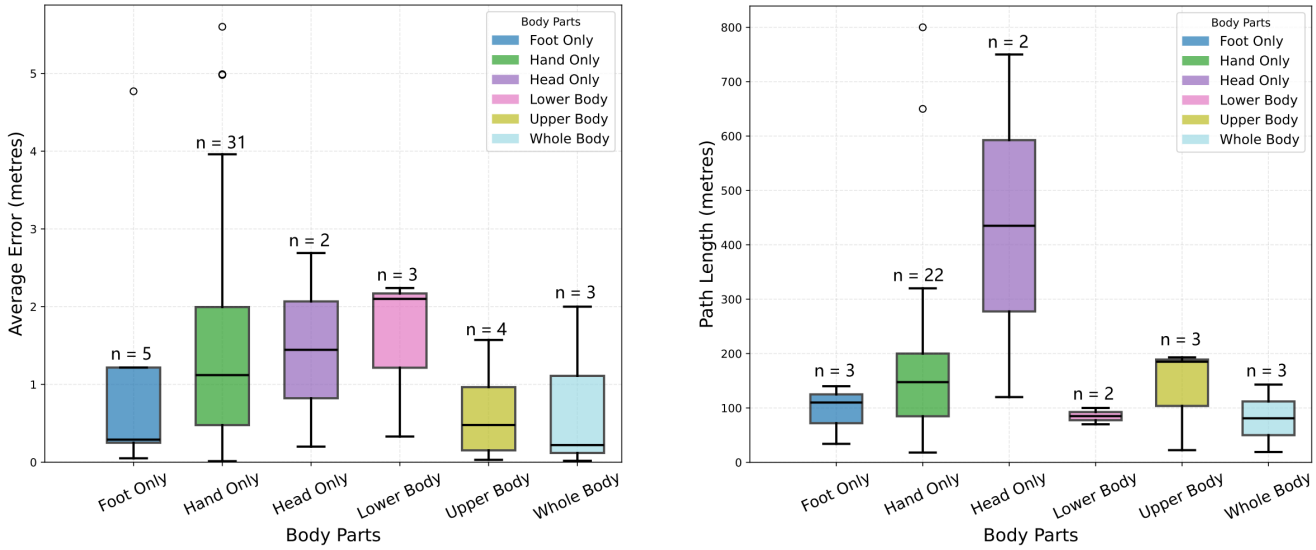

(a) Average Error by body placement

(b) Path Length by body placement

FIGURE 12. **The box plots show the average position error (a) and reconstructed path length (b) for different body parts (foot only, hand only, head only, lower body, upper body, and full body) under different sensor placement configurations. The number above each box indicates the number of included studies (n). Note that n varies across subfigures and categories, as not all studies reported sufficient information to compute every metric. Given the significant variation in the data, data points with a path length above 1000 were filtered out for the analysis.**

ing upon this foundation, [92] demonstrated improved performance through enhanced algorithmic design, attaining a lower percentage error of 0.89 % over a comparable path length (∼ 147 m). For shorter trajectories, [101] achieved 1.52 % error over approximately 50.34 m, demonstrating high accuracy over limited distances. Although [113] employed a longer path (∼ 251 m), it adopted the CEP metric and reported 0.96 m error, reflecting a different analytical focus on statistical accuracy. Notably, [119] reported an exceptionally low percentage error of 0.36 % over a 1, 400 m path, highlighting the maturity and robustness of foot-mounted sensor algorithms for large-scale deployment scenarios.

In contrast, hand-mounted sensor studies reveal substantial variation in error metrics and adaptability to diverse path configurations, reflecting the inherent challenges posed by upper-limb motion dynamics. The work in [75], which combined hand- and waist-mounted sensors, produced a cumulative error of merely 0.14 m over a 45 m trajectory. Conversely, [55] employed ATE over a trajectory of approximately 200 m and reported an error of 1.28 m, illustrating how performance can vary considerably across different sensor-fusion architectures. Furthermore, [117] and [126] reported mean errors of 2.32 m and 1.6 m respectively, although their path information was either missing or relatively short (∼ 127 m), suggesting divergent strategies for handling measurement noise and signal processing. Research by [128] achieved an ATE of 0.64 m over 600 m, whilst [31] reported 1.10 m ATE over a notably short path (∼ 20 m), further demonstrating how algorithms respond variably to changes in trajectory length and underscoring the complexities inherent in hand-mounted configurations where gestures and daily activities introduce significant perturbations.

Head-mounted sensor studies employed diverse evaluation metrics and demonstrated distinct performance characteristics influenced by mounting height and orientation. The study by [70] reported a percentage error of 0.32 m over 127 m, whilst [85], despite not providing specific path length information, revealed an ATE of 2.69 m, indicating challenges in maintaining overall trajectory accuracy. Meanwhile, [40] employed an eye-level sensor configuration and reported a mean error of 0.3 m over approximately 170 m, demonstrating that sensor placement height significantly influences performance and suggesting that head-mounted systems require careful consideration of mounting position and angular alignment to optimise signal quality.

Lower body studies exhibit considerable algorithmic diversity through varied anatomical combinations and error characterisations, reflecting the biomechanical complexity of lower-limb motion patterns. Research by [69] utilised foot and wrist sensors over 740 m, with performance measured through velocity error (0.12 m/s), offering an alternative perspective on navigation accuracy beyond conventional position-based metrics. The work by [83] applied sensors across foot, shin, and thigh over approximately 56 m, producing a cumulative error of merely 0.15 m and demonstrating the advantages of distributed sensing throughout the lower limbs. Additionally, [99] introduced a terminal pose error of 2.50 m for approximately 207.72 m. Both [104] and [134] focused on wrist sensors; however, [104] achieved 0.5 % error over an extended path (∼ 1, 000 m), whilst [134] reported 0.32 m ATE without providing path information,

reflecting differing priorities in experimental design and error modelling philosophies.

Studies examining upper body and whole body configurations demonstrate broader application scenarios and reveal the considerable potential advantages of multi-sensor fusion strategies. Research by [111] employed a chest-mounted sensor and achieved 0.193 m ATE over 185 m, demonstrating the effectiveness of trunk-mounted configurations where motion is relatively constrained. The work by [138] utilised an arm sensor and attained 0.03 m ATE, though path information was not provided, indicating substantial potential for upper-limb tracking applications. Regarding whole body sensing configurations, [72] combined waist, chest, and foot sensors to achieve 0.8 % error over 230 m, demonstrating effective integration across multiple anatomical regions. Similarly, [87] employed foot and back sensors and achieved 1.3 % error over an exceptionally long path (4,196 m), highlighting robustness in extended navigation scenarios. Furthermore, [124] integrated sensors across forearm, lower leg, head, and pelvis, reporting ATE values of 0.22 m and 0.26 m over 143 m, illustrating both the advantages and implementation challenges of comprehensive multi-sensor fusion in complex environments requiring detailed body motion capture.

To systematically examine how IMU placement affects overall system performance, we compared positioning accuracy across various anatomical locations, as illustrated in Figure 12. In addition to accuracy, the analysis highlights a clear relationship between navigation performance and the effective path length associated with each sensor configuration. Systems employing upper body or whole body sensor configurations substantially outperform single-location implementations, achieving both lower average errors and more consistent path lengths. Specifically, upper body placements achieve an average navigation error of 0.64 m, whilst whole body configurations attain 0.75 m. In contrast, single-location systems exhibit considerably higher errors and greater variability in path length. Foot-mounted sensors average 1.32 m, whilst hand-mounted sensors demonstrate the poorest performance at 1.60 m average error, accompanied by longer and more erratic paths. This degradation likely stems from significant disturbances introduced by natural hand movements during ambulation, including gesturing, mobile phone use, and arm swinging, which inflate the estimated trajectory and substantially compromise signal quality. Lower body configurations achieve a 1.25 m average error with comparatively stable path lengths, whilst head-mounted systems, despite combining IMUs with cameras and other sensing modalities, exhibit longer path lengths and attain a 1.45 m average error. These findings collectively demonstrate that navigation accuracy is closely coupled with path length stability. Multi-location systems benefit from complementary signal acquisition across diverse anatomical positions, enabling mutual verification, suppressing spurious

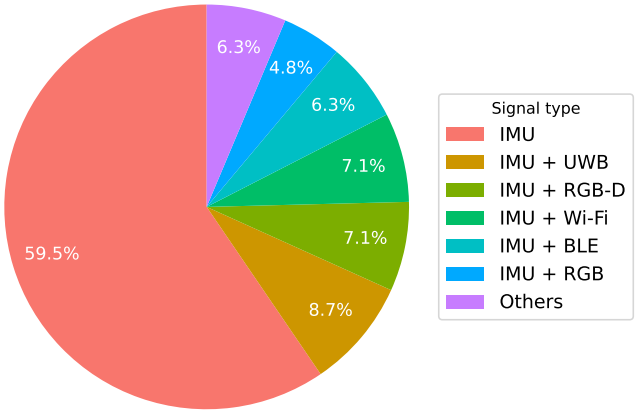

FIGURE 13. A comparative analysis of performance across wearable inertial navigation systems employing various sensor configurations. The IMU represents the most extensively utilised sensor in the literature, offering the advantages of minimal susceptibility to environmental perturbations whilst maintaining a reasonable degree of positioning accuracy.

motion-induced drift, and yielding shorter, more reliable trajectories through effective sensor fusion.

In contrast, configurations relying solely on a single sensor (e.g., hand-mounted or foot-mounted) typically face greater challenges (shown in Figure 12). Specifically, hand-held devices often exhibit degraded performance due to the noise introduced by common daily hand movements and activities. Other anatomical placements, such as lower body or head-mounted configurations, exhibit an accuracy performance that generally falls between that of the multi-sensor systems and the single-location systems. In summary, to achieve higher navigation accuracy and robustness, adopting a strategy that involves acquiring and fusing information from multiple anatomical locations proves considerably more effective than relying on a single body segment.

D. The impact of sensor configurations

This section provides a comprehensive review of existing sensor configurations used in IMU-based wearable positioning systems and evaluates their corresponding performance across a wide range of studies. We first outline the overall distribution of sensor modalities in the literature, highlighting of IMU only approaches and multiple modals fusion strategies such as IMU combined with UWB, RGB-D, WiFi, and BLE. Building on this overview, the section then examines the implementation details and reported accuracy of each sensor configuration, identifying how factors such as

path length, environmental complexity, and fusion algorithms influence positioning outcomes. Finally, a comparative performance analysis is presented to quantify the benefits of integrating complementary signals with inertial data.

Figure 13 illustrates the proportion of different sensor configurations employed in existing studies, clearly reflecting overall preferences and the distribution of various signal combinations. Methods relying exclusively on IMUs account for the largest share, approximately 59.5 %, indicating that inertial measurement units remain the most commonly adopted fundamental solution owing to their low cost, straightforward architecture, and ease of deployment. In contrast, fusion-based methods exhibit a more balanced distribution across multiple categories. Among these, IMU + UWB (8.7 %) and IMU + RGB-D (7.1 %) command slightly higher proportions, suggesting substantial potential for enhancing positioning accuracy and consequently attracting greater research attention. The combinations of IMU with WiFi, BLE, and RGB account for 7.1 %, 6.3 %, and 4.8 % respectively, demonstrating how wireless signals and visual cues can effectively complement inertial navigation. Finally, the 'Others' category constitutes 6.3 %, representing less prevalent or emerging multi-source fusion strategies. Overall, whilst single-IMU methods continue to dominate the field, the diverse distribution of multiple modals fusion approaches indicates that researchers are actively exploring effective methodologies to improve positioning performance in complex environments. The following analysis examines the specific implementations and performance characteristics of these different sensor configurations, beginning with IMU only approaches before progressing to various multi-sensor fusion strategies.

Among studies employing IMUs exclusively for positioning, most methods utilise inertial navigation, though the specific algorithmic implementations vary considerably. For instance, the work presented in [71] employed a velocity-error metric on a straight path of approximately 1400 m, yielding an average error of 0.33 m/s. The study described in [75], by contrast, computed cumulative error on a 45 m straight path and reported 0.14 m, demonstrating that cumulative drift can be effectively controlled over short distances. Similarly, research documented in [81] reported a cumulative error of 0.45 m on a 120 m straight path combined with a loop trajectory, whilst the investigation in [86] evaluated stairway paths across multiple segments and obtained errors of 0.22 m and 0.26 m, thereby highlighting how path complexity influences algorithmic performance. Furthermore, the approach in [45] utilised mean error on a 70 m straight path and reported 0.3 ± 1.8 m, whereas studies in [55] and [61] applied absolute trajectory error on extended straight paths and achieved 1.28 m and 1.71 m respectively, suggesting significant drift accumulation over longer distances. In contrast, investigations in [46] and [142] applied ATE on loop paths and both achieved approximately 0.47 m, implying that loop closures can effectively mitigate accumulated error. These results collectively indicate that whilst IMU only systems exhibit varying performance depending on path length and complexity, they remain viable for applications where acceptable error thresholds are moderately relaxed.

Regarding studies that integrate IMUs with RGB-D sensors, these systems predominantly rely on VIO, though their implementations differ in feature extraction and sensor fusion strategies. The RGB-D sensor provides both colour information and depth measurements, which are fused with IMU data through tight or loose coupling mechanisms to constrain inertial drift. For example, research in [76] reported an ATE below 0.2 m on a 120 m path incorporating turns, whilst the work in [111] achieved an ATE of 0.193 m on a comparable 185 m path, demonstrating the effectiveness of combining visual feature matching with IMU data. Concurrently, the study in [123] evaluated cumulative error on a 10 m straight path and obtained 0.15 m, whereas the investigation in [12] reported an ATE of 0.12 m on a 180 m straight path, indicating that RGB-D depth information can substantially improve positioning accuracy in structured environments. The fusion process typically involves using visual features for pose estimation whilst IMU measurements provide motion constraints and bridge gaps during visual occlusions. These results suggest that IMU-RGB-D fusion achieves superior performance compared to IMU only systems, with the visual modality effectively constraining inertial drift through feature-based corrections.

In studies examining IMU with WiFi fusion, the emphasis typically centres on wireless signal processing and radio-map construction methodologies. WiFi signals are fused with IMU data through fingerprinting approaches or RSSI measurements, which provide position constraints to correct inertial drift. The research presented in [28] reported a cumulative error of 2.5 m on a 180 m straight path, potentially attributable to interpolation-based radio-map construction. By comparison, the work in [30] employed ATE on a 168 m loop and reported 1.45 m, whilst the study in [135] achieved a mean error of 0.719 m on an 18 m path with turns, illustrating the adaptability of WiFi fingerprinting in geometrically complex routes. Additionally, the investigation in [145] combined two-way ranging (TWR) with WiFi and reported an ATE of 0.24 m on a 14 m loop, underscoring the advantage of multiple modals fusion approaches that leverage both ranging and fingerprinting techniques. These findings demonstrate that IMU-WiFi fusion performance is highly dependent on radio-map quality and signal processing algorithms, with ranging-based methods generally outperforming fingerprinting approaches.

For IMU-BLE fusion configurations, the majority of studies utilise BLE beacons for position correction, though their algorithmic designs exhibit notable variations in beacon placement strategies and signal filtering techniques. The BLE signals are typically fused with IMU through proximity detection or RSSI-based trilateration, providing periodic posi-

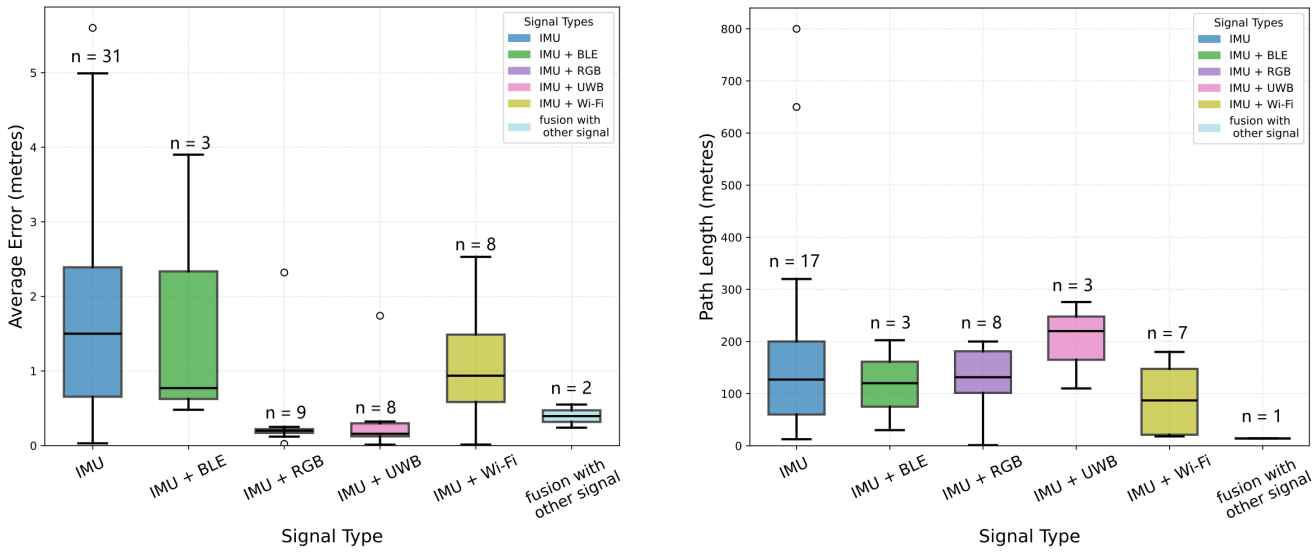

(a) Average Error by signal type

(b) Path Length by signal type

FIGURE 14. Box plots showing distribution of average positioning error (a) and path length (b) in positioning tasks using different signal type combinations. The number above each box indicates the number of included studies (n). Note that n varies across subfigures and categories, as not all studies reported sufficient information to compute every metric. Since there were major differences in the data, we excluded all data points with path lengths over 1000 from our analysis. The plots illustrate the positioning error distribution when using an IMU alone, when fusing an IMU with RGB, BLE, WiFi, UWB and other signal types. Boxes represent the quartile range, the black horizontal line indicates the median, the whisker line represents the overall data distribution, and outliers are marked with dots. The results show that the error fluctuation of using an IMU alone or IMU + BLE is relatively large, while IMU + RGB and IMU + UWB achieves the lowest error and highest stability; IMU + WiFi and the fusion with other signals provide moderate improvements, with corresponding variations reflected in both error and path length distributions.

tion updates to correct accumulated inertial errors. Research documented in [32] reported a mean error of 0.76 m on a 202.5 m loop, whereas the work in [34] achieved 0.48 m on a 30 m loop, suggesting that shorter paths may benefit from higher beacon density and more frequent correction opportunities. However, the investigation in [36] employed ATE on a 120 m straight path and obtained 3.9 m, indicating that BLE signal attenuation and environmental interference can substantially degrade performance, particularly when different filtering or calibration methods are applied. These results reveal that whilst BLE-based corrections can enhance IMU performance in beacon-rich environments, signal propagation characteristics remain a limiting factor for accuracy.

Finally, alternative fusion approaches encompassing IMU-UWB, IMU-pressure sensors, and IMU-LiDAR employ increasingly specialised algorithms tailored to their respective sensing modalities. The study in [6] demonstrated that IMU-UWB fusion, which leverages ultra-wideband ranging for precise distance measurements fused with inertial data, achieved a percentage error of merely 0.59 % on a 55 m loop, showcasing the exceptional accuracy afforded by UWB ranging technology. Research in [13] examined IMU-pressure fusion, wherein barometric pressure sensors provide altitude corrections to complement inertial measurements, reporting cumulative errors of 0.855 m on a 190 m path; whilst the pressure sensor aided vertical positioning, substantial horizontal drift persisted over extended trajectories. The investigation in [42] explored IMU-LiDAR fusion, integrating light detection and ranging point clouds with inertial data through SLAM frameworks, and achieved a percentage error of 0.08 % on a 183 m loop, demonstrating that LiDAR-based SLAM can dramatically reduce cumulative drift through geometric feature matching. These diverse sensor-fusion methodologies exhibit varying performance characteristics contingent upon path conditions, sensor modalities, and fusion algorithms, thereby providing valuable empirical guidance for the development and optimisation of indoor positioning systems.

To facilitate systematic comparison across these diverse sensor configurations, Figure 14 presents box plots illustrating positioning performance as measured by average error. As the data reveal, systems integrating IMU and RGB achieve the most accurate and stable performance, which is accompanied by relatively consistent path lengths, indicating robust trajectory estimation over extended motion. In contrast, configurations with larger positioning errors, most notably IMU only and IMU fusion with BLE systems, also exhibit greater variability in path length, suggesting accumulated drift and less reliable motion reconstruction over time. On average, systems relying solely on IMU inputs exhibit an ATE of 1.92 metres, whereas those fusing IMU and RGB signals achieve 0.41 metres, and IMU combined with WiFi signals reach 1.19 metres. This trend highlights a strong correlation between lower positioning error and more stable path length, demonstrating that effective sensor fusion improves point wise accuracy. These quantitative findings conclusively demonstrate that whilst IMU only systems can

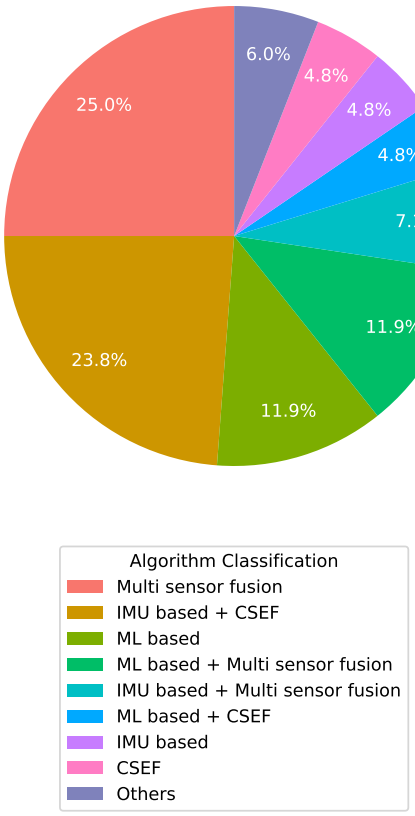

FIGURE 15. The pie chart shows the proportion of different algorithm combinations in the research literature. It illustrates the distribution of various localisation algorithms and their combinations with classical stochastic estimation frameworks (CSEF), IMU based, machine learning (ML) based, and multi-sensor fusion methods in the overall research. It can be seen that "IMU based + CSEF" has the highest proportion, followed by standalone CSEF methods and methods combining IMU with multi-sensor fusion and CSEF. Other combinations and independent methods have a smaller proportion, reflecting that current research tends to favor hybrid frameworks that integrate IMU with traditional estimation algorithms.

deliver acceptable navigation accuracy, multi-sensor fusion substantially enhances positioning precision and trajectory reliability in IMU based wearable systems.

In summary, standalone IMU implementations remain prevalent due to their cost-effectiveness and ease of deployment, yet they are fundamentally limited by inherent drift accumulation. Strategies integrating RGB significantly enhance positioning precision. Conversely, WiFi and BLE technologies exhibit greater susceptibility to environmental interference. Collectively, while multi-sensor fusion architectures generally outperform single-modality approaches, the selection of optimal configurations necessitates careful consideration tailored to specific operational scenarios.

E. The impact of positioning algorithm

This section provides a comparative analysis of the four algorithmic paradigms defined in Section D: IMU based methods, classical stochastic estimation frameworks (CSEF), multi-sensor fusion strategies, and machine learning-based approaches. As discussed previously, these categories are distinguished primarily by the level at which their core algorithmic contribution operatessignal processing, state estimation, fusion architecture, or learned representations, respectivelyrather than solely by their sensor inputs. However, because the fusion-architecture category inherently requires multiple sensor modalities, whereas the other three categories may or may not employ additional sensors, a direct aggregate comparison across all four paradigms inevitably conflates algorithmic and sensor-configuration effects. To disentangle these factors, the analysis below first presents the overall algorithm-level comparison, then examines each paradigms performance broken down by sensor modality, and finally provides cross-paradigm comparisons under matched sensor configurations. To facilitate a detailed comparison of system performance across the different categories, we present the absolute errors reported by each study alongside the corresponding path lengths. Furthermore, we compare the relative pose errors (RPE) across studies, enabling a more objective and accurate assessment of performance across different algorithms and device configurations. It should be noted that the RPE values presented herein were manually derived from data reported in the original studies, as the majority of papers do not explicitly provide this metric.

IMU-based algorithms often incorporate zero-velocity updates and sensor corrections to enhance positioning accuracy. A differential layout multi-IMU array approach has been demonstrated by [119], who apply ZUPT combined with Kalman filter to achieve a percentage error of merely 0.36 % over a path length of 1,400 m. Similarly, [147] rely solely on PDR with frequency self-synchronisation, attaining a percentage error of 0.9 % over 550 m, whilst [46] employs basic PDR for an ATE of 0.474 m over a shorter 20 m trajectory. In a more complex implementation, [53] merge ZUPT with the Informer model and Kalman filtering, yielding a cumulative error of 19.77 m over an extended 2,000 m path. These variations in algorithm complexity and performance demonstrate how IMU-based methods can be tailored to specific application requirements, from simple PDR implementations to sophisticated multi-sensor arrays.

Classical stochastic estimation frameworks, which predominantly rely on Kalman filters and their variants, represent another major category of navigation solutions. The work of [86] exemplifies the integration of strap-down INS with ZUPT and extended KF, limiting cumulative error to 0.22 m and 0.26 m on short paths. A standard Kalman filter combined with ZUPT has been employed by [114], yielding an end-pose error of 0.43 m over 100 m, illustrating how slight modifications in filter design can impact accuracy. For long-term navigation scenarios, [141] apply a transformer-based architecture with in-situ calibration (TAFI) to achieve an ATE of 1.47 m over an extensive 21,910 m path, emphasising the role of adaptive filtering in maintaining performance over extended distances. Furthermore, [125] extend

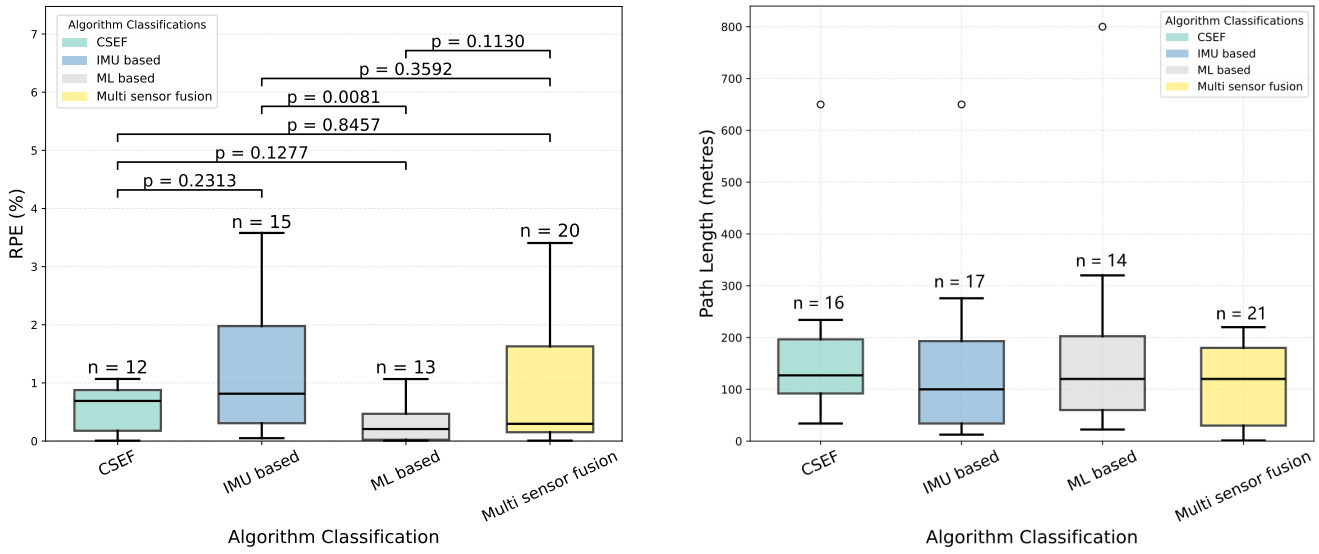

(a) RPE by positioning algorithm.

(b) Path Length by positioning algorithms.

FIGURE 16. A comprehensive comparison of various positioning algorithms based on both (a) RPE and (b) testbed path length. The number above each box indicates the number of included studies (n). Please note that n varies across subfigures and categories, as not all studies reported sufficient information to calculate the corresponding metric. Outliers are marked as individual points. Owing to pronounced data deviations, we omitted samples with path lengths greater than 1000 when conducting the analysis. Statistical significance between positioning algorithms groups is indicated by horizontal bars. The results indicate a statistically significant difference between IMU based and ML based approaches, with p-values of 0.0081 (Mann-Whitney U test), well below the conventional threshold 0.05. No significant differences are found among the other compared pairs.

stochastic methods to probabilistic modelling by employing a Bayesian network for floor localisation using inertial and barometer data, achieving a remarkably low percentage error of 0.41 %. These studies collectively demonstrate the versatility and robustness of classical estimation frameworks across diverse navigation scenarios.

Within machine learning-based methods (ML based), deep neural network architectures have been explored to learn complex patterns from inertial data. The research by [106] employs a ResNet-based deep neural network with random orientation initialisation for pose-invariant inertial odometry, achieving a low ATE of 0.3 m over an impressive path length of 3,000 m. In contrast, [142] utilise a simpler neural network architecture with linear layers, resulting in an ATE of 0.47 m over 200 m, demonstrating the versatility of deep learning architectures in handling inertial data. Additionally, [66] integrate a gated recurrent unit with support vector regression (GRU-SVR) alongside ZUPT to reduce percentage error to 1.14 % and 1.68 % on different paths, highlighting how recurrent networks can enhance traditional IMU-based techniques. Whilst these machine learning approaches represent a growing trend towards data-driven navigation solutions, their performance and computational requirements vary considerably with network architecture and training data availability. Neural networks trained on specific datasets may struggle to generalise across different environments, sensor configurations, or motion patterns, leading to degraded performance when deployment conditions deviate from training scenarios. Furthermore, the limited availability of diverse, high-quality labelled inertial datasets constrains the robustness of learned models, whilst variations in sensor noise characteristics and sampling rates between training and inference can significantly impact accuracy. These challenges underscore the necessity for more generalised training frameworks and domain adaptation techniques to improve the reliability of ML based inertial navigation systems.

Multi-sensor fusion approaches combine IMU data with complementary sensing modalities to improve robustness and accuracy in challenging environments. The integration of IMU with LiDAR and RGB-D sensors through visual-inertial odometry and SLAM has been investigated by [56], achieving approximately 1.5 m cumulative error over 50 m. Wireless signal integration represents another fusion strategy, as demonstrated by [29], who integrate WiFi fingerprinting with PDR and weighted fusion, reducing error to a percentage of 0.98 % over 112 m. The visual INS approach utilised by [122] achieves a percentage error of 0.76 % over 380 m, whilst [34] blend BLE angle-of-arrival and received signal strength with PDR and a Kalman filter, resulting in a mean error of 0.48 m. This diversity in fusion strategies underscores the potential for combining multiple sensing modalities to compensate for individual sensor limitations, albeit at the cost of increased system complexity.

The comparative performance of these different positioning algorithms in wearable inertial navigation is illustrated in Figure 16. It is observed that ML based studies yield the most reliable performance, achieving an average RPE of 0.35%, indicating the most stable trajectory estimation. The

average RPEs for CSEF, IMU based, and Multi sensor fusion studies are 0.69%, 1.22%, and 1.00%, respectively. Statistical significance tests, namely the Mann-Whitney U tests, were conducted to evaluate pairwise differences between the three methodological categories. The results indicate a statistically significant difference between IMU based and ML based approaches, with p-values of 0.0081 (Mann-Whitney U test), well below the conventional threshold 0.05. No significant differences are found among the other compared pairs.

It is also observed that ML based studies in the surveyed literature tend to be evaluated over considerably longer trajectories, during which absolute error naturally accumulates. The low RPE suggests that, per unit distance travelled, the error growth rate of ML based systems is relatively well controlled, potentially reflecting the capacity of learned models to capture complex motion patterns and suppress systematic drift over extended periods. Conversely, IMU-based algorithms exhibit a steeper proportional error growth, indicating that their reliance on deterministic corrections such as ZUPT may become less effective as trajectory length increases.

The influence of sensor modality on CSEF-based localisation is described in Figure 17 based on RPE and testbed path length. When the CSEF-based system relies solely on IMU signals, it exhibits a median RPE of 0.69%, with a wide interquartile range spanning from 0.01% to 1.07% and a mean of 0.58%. The breadth of this distribution, together with the proximity of the median to the upper quartile, indicates that RPE performances are not only highly variable but also skewed towards larger frame-to-frame deviations. This result is consistent with the fact that IMU drift gradually builds up between frames, which makes the local motion estimates less stable along the trajectory. The presented path length distribution also supports this interpretation. It is reported that testbed path length for IMU-only studies span a broad range (median = 135 m, IQR = 90200 m) with an extreme outlier at 650 m, indicating that unstable relative pose estimation is often accompanied by uncontrolled trajectory drift and unreliable path reconstruction. By contrast, the IMU+RGB configuration yields a markedly lower and fully concentrated RPE of 0.17% over a comparatively short path length (120 m). However, as this category comprises only one single study (as shown in Figure 17), no robust conclusion can be drawn from this observation alone, nor can a test of statistical significance be performed.

A detailed comparison of the positioning performance across different signal inputs for the multi sensor fusion based localisation system is presented in Figure 18. It is observed that IMU + RGB configuration achieves the lowest average RPE of 0.15%. This suggests that visual cues usually provide strong drift correction but can occasionally fail in challenging scenes. On the other hand, experiments combining IMU and UWB have the longest trajectories, with a median of 165 m. With only two papers reporting path length for their experiments, this configuration achieves an average RPE of 0.21%. In contrast, IMU + BLE configuration displays the most inconsistent performance, with RPE spanning from 0.38% to 3.25%. This indicates that BLE constraints can vary strongly in effectiveness across trajectories. IMU + WiFi configuration tends to sit between these extremes but still shows a broad error distribution, implying that fluctuating signal quality and environmental dependence can limit how steadily WiFi can suppress inertial drift. Although this configuration yields shorter typical path lengths, but the substantial variability in path length and RPE performance suggests the least reliable positioning performance among the sensor configurations examined. Statistical significance tests (i.e., MannWhitney U test) were conducted. The results indicate that the significance level between IMU + RGB and IMU + WiFi is 0.0499 (Mann-Whitney U test), whilst the significance level between IMU + BLE and IMU + RGB is 0.0485 (Mann-Whitney U test). These results suggest that the performance differences between IMU + RGB and the other two fusion strategies are statistically significant under the Mann-Whitney U testS.

A comparison of ML-based methods under different signal types, based on both RPE performance and testbed path length, is presented in Figure 19. As none of the included studies employing ML-based algorithms adopt RPE as a performance evaluation metric, the values reported here were computed manually by the review authors. When using IMU only, the reconstructed path length varies heavily, spanning between 60 and 800 m with a median value of 260 m. Despite this wide range of traversal distances, the IMU only configuration achieves the lowest average RPE of 0.14%. This indicates that ML based algorithms trained exclusively on inertial data exhibit superior relative accuracy when normalised against traversal distance, even across substantially longer trajectories. This pattern reflects a broader characteristic of ML based methods: when trained on inertial signals alone, the learned models can capture relative motion dynamics with considerable fidelity, maintaining proportionally low error growth as the path extends. By comparison, fusing IMU data with BLE compresses the path length distribution in the literature, which tightens to a range of 70160 m with a median of 120 m. However, the added complexity of BLE signal patterns increases the median RPE to 1.74%, more than an order of magnitude higher than that of the IMU only configuration. This trade-off highlights that, whilst supplementary wireless signals can provide spatial constraints intended to mitigate inertial drift, the heterogeneous and environment-dependent nature of BLE measurements introduces additional noise that ML models must learn to accommodate, thereby complicating the training process and potentially limiting generalisation over distance. The IMU + WiFi configuration occupies an intermediate position, with path lengths concentrated between 40 and 70 m and a derived RPE ranging from 0.21% to 3.41%. The breadth of this RPE range, coupled with the comparatively short trajectories evaluated, suggests

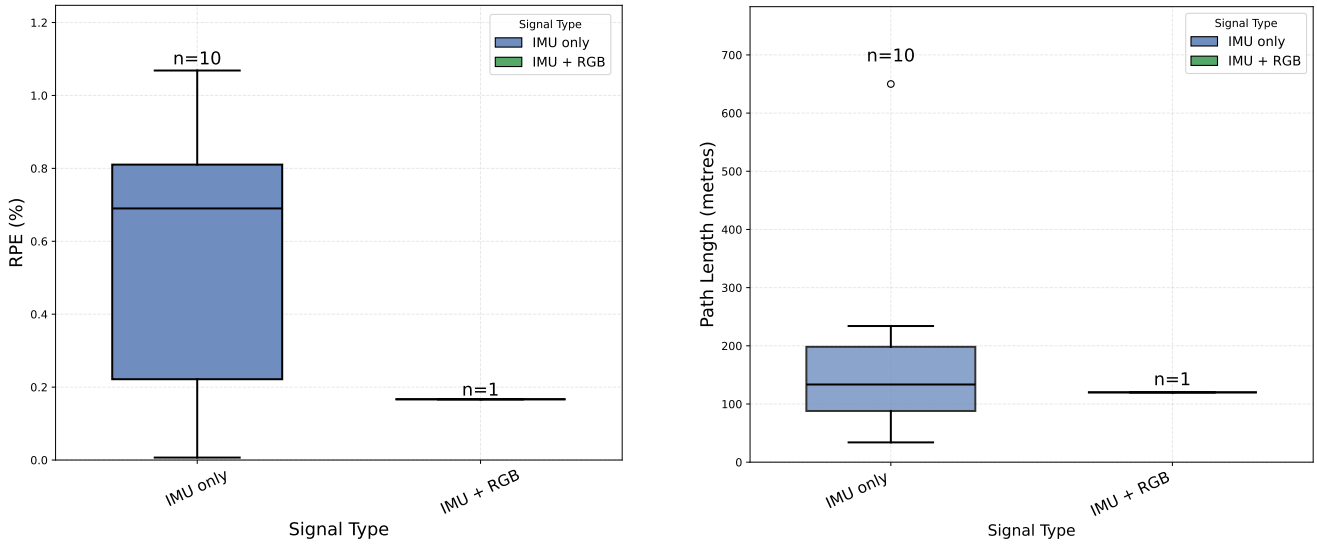

(a) RPE by signal type for CSEF studies.

(b) Path Length by signal type for CSEF studies.

FIGURE 17. Performance comparison of CSEF methods under different signal types (IMU-only and IMU + RGB) based on both (a) RPE and (b) testbed path length. The number above each box indicates the number of included studies (n). Please note that n varies across subfigures and categories, as not all studies reported sufficient information to calculate the corresponding metric. Outliers are marked as individual points. Statistical significance testing is not applicable for these results, as there is only 1 paper in the IMU+RGB group.

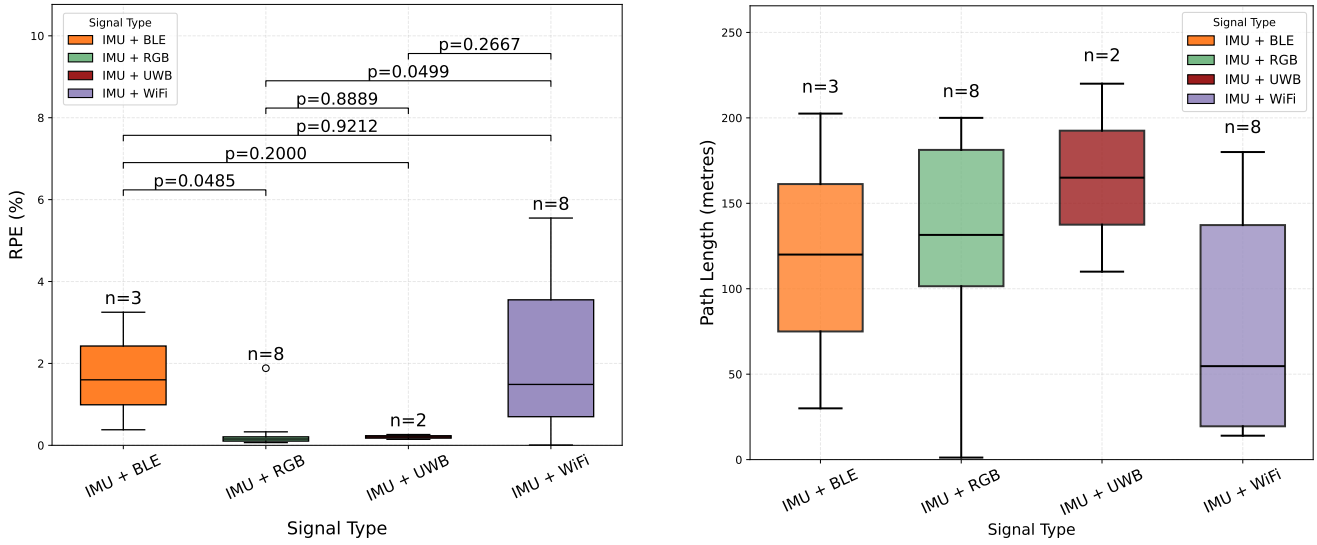

(a) RPE by signal type for Multi sensor fusion based algorithms.

(b) Path Length by signal type for Multi sensor fusion based algorithms.

FIGURE 18. Performance comparison of Multi sensor fusion methods under different signal types based on both (a) RPE and (b) testbed path length. The number above each box indicates the number of included studies (n). Please note that n varies across subfigures and categories, as not all studies reported sufficient information to calculate the corresponding metric. Outliers are marked as individual points. Statistical significance between different signal type groups is indicated by horizontal bars. The results indicate that the significance level between IMU + RGB and IMU + WiFi is 0.0499 (Mann-Whitney U test), whilst the significance level between IMU + BLE and IMU + RGB is 0.0485 (Mann-Whitney U test). No significant differences are found among the other compared pairs.

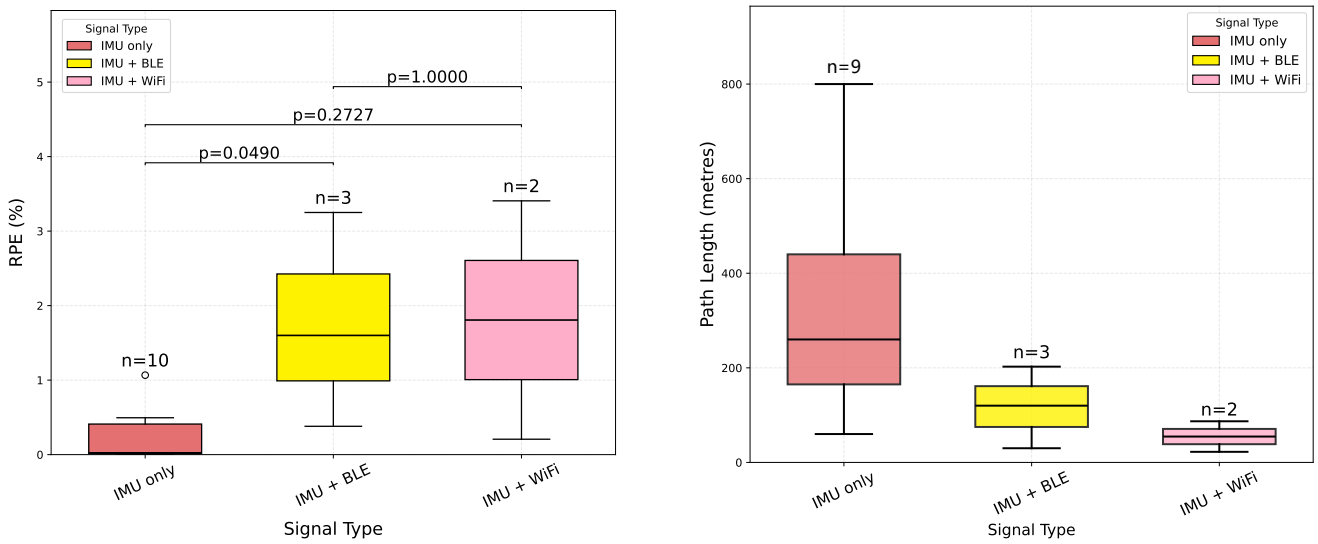

(a) RPE by signal type for ML based algorithms.

(b) Path Length by signal type for ML based algorithms.

FIGURE 19. Performance comparison of ML based methods under different signal types based on both (a) RPE and (b) testbed path length. The number above each box indicates the number of included studies (n). Please note that n varies across subfigures and categories, as not all studies reported sufficient information to calculate the corresponding metric. Outliers are marked as individual points. Statistical significance between different signal type groups is indicated by horizontal bars. Only the MannWhitney U test p-value for the comparison between IMU only and IMU+BLE was below 0.05 (0.0490). No significant differences are found among the other compared pairs.

less consistent behaviour across studies. However, the limited sample of only two papers in this category substantially constrains the generalisability of these findings. Statistical significance tests (i.e., MannWhitney U test) were conducted, and only the MannWhitney U test p-value for the comparison between IMU only and IMU+BLE was below 0.05 (0.0490). Taken together, these results underscore that the relative accuracy of ML based inertial navigation systems is heavily contingent upon sensor modality: different signal types not only alter the quality and diversity of training data available to the model, but also determine the extent to which learned representations can generalise across varying trajectory lengths.

Furthermore, three comparative analyses are conducted under identical signal input settings between ML algorithms and, CSEF and Multi sensor fusion algorithms, as shown in Figure 20. When comparing RPE performance across sensor configurations, several notable trends emerge. In IMU only settings, ML based approaches significantly outperform CSEF, achieving an average RPE of 0.14% compared with 0.58% a roughly fourfold improvement. This suggests that learned models are particularly adept at compensating for the inherent drift and noise in standalone inertial data. However, this advantage diminishes considerably once supplementary radio signals are introduced. For IMU + BLE configurations, Multi sensor fusion and ML based methods converge at similar level of RPE. In the case of IMU + WiFi, ML achieves an average RPE of 1.81%, compared to 2.12% for Multi sensor fusion. This is because data-driven methods are better equipped to mitigate WiFi-specific challenges such as multipath effects and coarser spatial resolution. Statistical significance tests (i.e., Mann-Whitney U test) were carried out for Figure 20. Only Figure 20 (a) demonstrates a statistical significance with p-values of 0.0247 (Mann-Whitney U test), indicating a significant difference between CSEF and ML based algorithms in IMU only studies. Taken together, these findings suggest that the corrective information provided by radio-based signals substantially overlaps with what ML models learn implicitly from inertial data alone. Overall, ML based methods perform equally well or better than CSEF and Multi sensor fusion across all signal configurations examined. However, it should be noted that the limited number of included studies reporting sufficient quantitative detail constrains the generalisability of these findings.

Across all methods, the scatter and fitted curves from Figure 21 indicate that average error generally increases as path length grows, meaning performance tends to worsen as trajectories become longer, although the scaling and stability vary by approach. For CSEF, the blue curve rises with path length and then levels off, which aligns with drift accumulating but being partly restrained by probabilistic corrections; nevertheless, several blue points at medium to long paths show large errors, suggesting occasional failures rather than uniformly stable behaviour. By comparison, the IMU based orange curve shows a shallow hump and then decreases, yet the orange points are widely spread at similar path lengths, so the apparent long-range improvement is more likely driven by sparse sampling and fit sensitivity than a dependable trend.

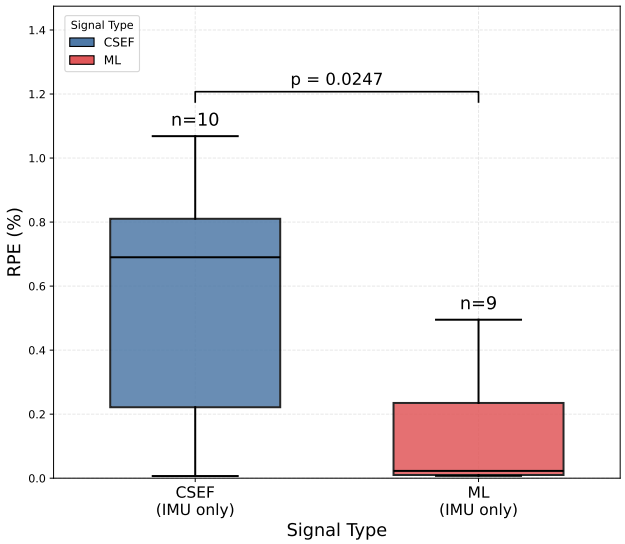

(a) RPE by positioning algorithm for IMU only studies.

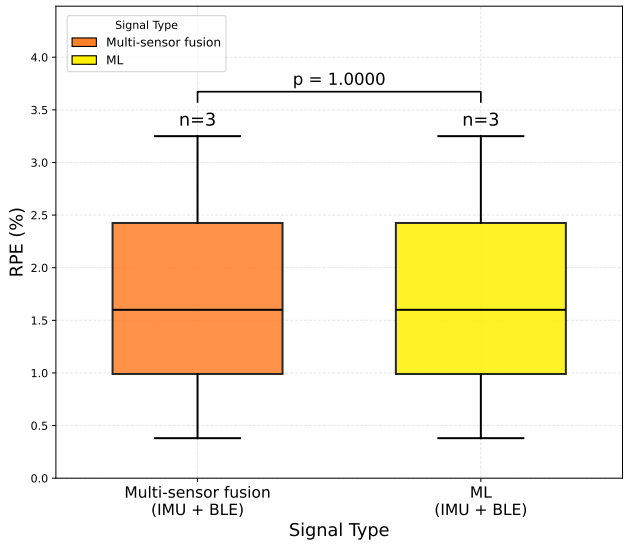

(b) RPE by positioning algorithm for IMU + BLE studies.

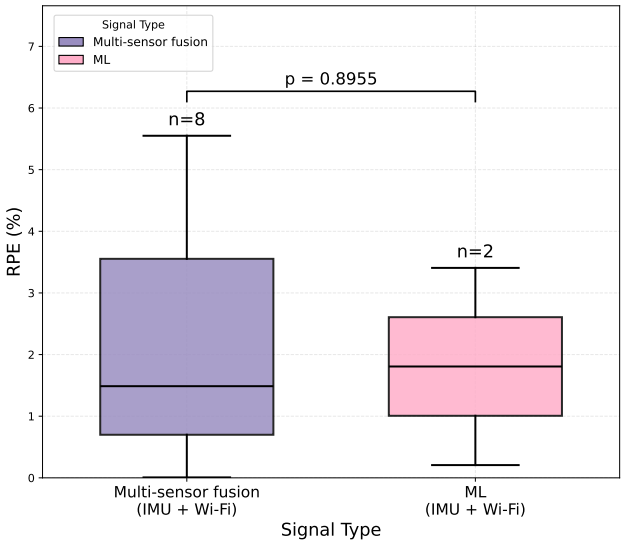

(c) RPE by positioning algorithm for IMU + WiFi studies.

FIGURE 20. The box plots show the three RPE comparisons: (a) the performance of CSEF and ML for IMU only studies, (b) the performance of Multi sensor fusion and ML algorithms for IMU + BLE studies, and (c) the performance of Multi sensor fusion and ML algorithms for IMU + WiFi studies. The number above each box indicates the number of included studies (n). Note that n varies across subfigures and categories, as not all studies reported sufficient information to compute every metric. Statistical significance between positioning algorithms groups is indicated by horizontal bars. The results indicate a statistical significance with p-values of 0.0247 (Mann-Whitney U test) between CSEF and ML methods for IMU only studies. No significant differences are found among the other compared pairs.

In contrast, the ML based green curve increases strongly and accelerates with distance, and the long-path green points include multiple high-error outliers, implying that these ML approaches, when examined through the lens of absolute error, appear more distance-sensitive and less consistent over long trajectories. This observed inconsistency, however, may be substantially attributed to a structural bias in the experimental literature itself: ML-based algorithms were almost always tested on longer trajectories. Finally, the multi-sensor fusion red points form the tightest low error cluster across the most densely populated mid range of path lengths, and the red curve stays comparatively low, indicating that additional modalities typically anchor the estimate and suppress drift; however, a notable red outlier shows that fusion can still break down under adverse sensing or calibration conditions.

In summary, combinations of IMU-based methods and classical stochastic frameworks remain the most prevalent in current research, benefiting from their mature theoretical foundations and computational efficiency. However, these approaches still face challenges related to data availability

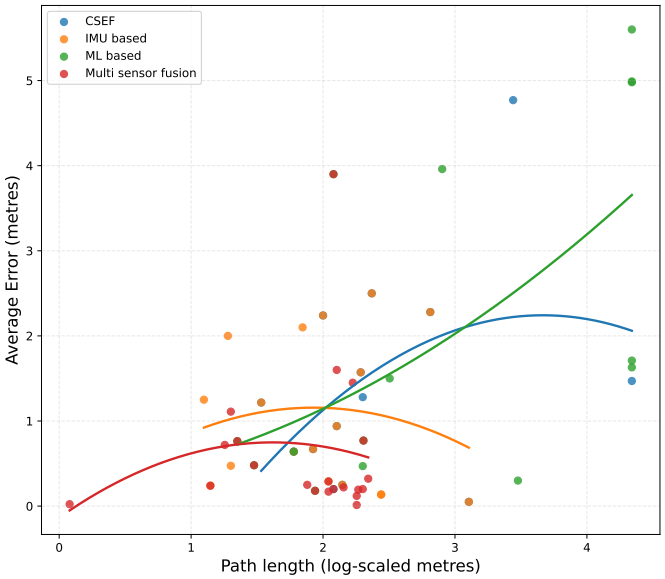

FIGURE 21. **Average error (m) as a function of path length (log-scaled metres) across CSEF, IMU-based, ML-based, and multi-sensor fusion algorithms. Individual results are shown as scatter points; fitted curves summarise overall trends, suggesting lower errors for multi-sensor fusion at comparable path lengths.**

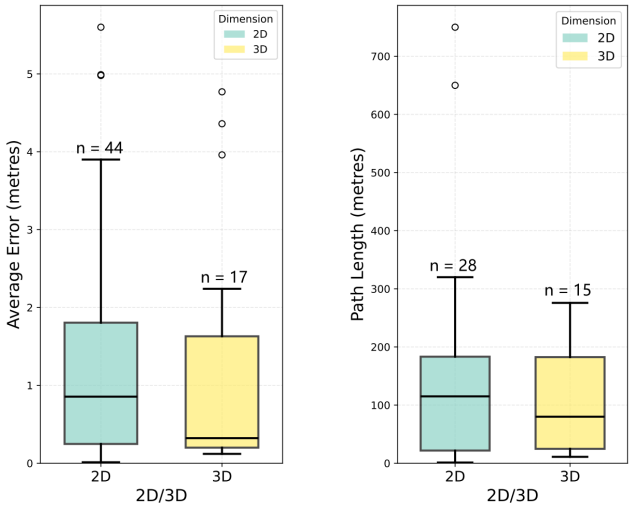

(a) Average Error by 2D/3D environment

(b) Path Length by 2D/3D environment

FIGURE 22. **A performance comparison of navigation systems in 2D and 3D environments, showing distributions of both average error (a) and path length (b). Because the dataset contained large inconsistencies, we removed observations whose path length was greater than 1000 prior to analysis. The box plots indicate lower median error values in 3D compared to 2D, while 2D environments exhibit greater variability in both error and path length. Additionally, path lengths tend to be longer and more widely distributed in 2D than in 3D, reflecting less constrained motion and more diverse navigation behaviors in planar environments.**

and real time performance requirements. Multi-sensor fusion algorithms, though capable of achieving higher accuracy through complementary information integration, remain relatively limited in deployment due to their increased complexity and computational demands. Notably, ML-based methods achieve the lowest relative pose error (0.35% average RPE), significantly outperforming IMU-based (1.22%) and CSEF (0.69%) approaches when error is normalised by distance travelled. Under matched IMU-only conditions, this advantage is statistically significant ($p = 0.0081$, Mann-Whitney U test). This suggests that ML-based algorithms are particularly effective at controlling per-unit-distance drift, and that the corrective information provided by radio-based signals substantially overlaps with what ML models learn implicitly from inertial data alone. However, the limited number of studies reporting sufficient quantitative detail constrains the generalisability of these findings. Nevertheless, classical frameworks continue to dominate current research, reflecting a preference for stable and reliable approaches that can be readily implemented in resource-constrained wearable devices. IMU-based algorithms thus remain the most widely adopted methods for wearable inertial navigation, offering a strong balance between practical deployability and computational feasibility across different application scenarios, although future research should further investigate the potential of ML-based methods as trajectory lengths and dataset availability continue to grow.

F. The impact of other factors

This section reviews the test environment settings used for evaluating algorithm performance in indoor positioning research. These settings are grouped into two types: planar tests (2D environments) and tests that include stairs, ramps, or height changes greater than one metre (3D environments). First, we describe the overall distribution of test setups reported in the literature, focusing on the criteria that distinguish 2D and 3D environments and the typical scenarios they represent. Based on this overview, we then discuss the key design elements, common experimental configurations, and evaluation goals associated with each type of test environment, and examine how factors such as environmental complexity, structural layout, and motion patterns influence positioning performance. Finally, through a comparative analysis, we summarise the different emphases and limitations of these two test settings when used to assess positioning algorithms.

Various 2D testing environments have been employed to validate pedestrian positioning algorithms under differing spatial constraints and trajectory complexities. For instance, school roads provided the setting for a complex path test spanning 740 m across an area of approximately 14,380 m^2 [69], where loosely coupled integration and automatic heading estimation substantially reduced rate errors. Conversely, more confined spaces have also been investigated: a small office room (5 m $\times$ 5 m) served as the testing

ground for straight line trials over 180 m [28], revealing cumulative errors that underscored algorithmic limitations in constrained environments, whilst a library setting (10 m × 15 m) accommodated circular path experiments of 50 m [94], with errors expressed as percentages to demonstrate the efficacy of low-cost foot-mounted IMUs in structured indoor spaces. Additional 2D evaluations have encompassed corridor environments featuring straight and turning trajectories [89], extended corridor tests [45], office-based loop paths [30], [100], [133], [136], school road straight paths [129], and corridor routes combining straight segments with turns [36], [135].

Otherwise, extending beyond planar motion, 3D testing environments have facilitated the assessment of positioning systems capable of handling elevation changes and multi-story structures. Laboratory-scale experiments have included a 56 m loop path within a 10 m × 18 m laboratory [83], which yielded low cumulative error and confirmed the suitability of inertial sensor networks for dynamic motion tracking, as well as an office-based loop test (183 m path length, 40 m × 60 m area) [42] that achieved an exceptionally low error rate of 0.08 %, thereby showcasing the high precision attainable through plane-feature-based SLAM in three-dimensional indoor mapping. Larger-scale trials have also been conducted, notably long-loop tests in mixed office road settings covering approximately 1, 900 m within an 86 m × 22 m testing area [73], where multi-sensor fusion effectively accommodated directional changes inherent in three-dimensional motion. Further 3D investigations encompassing slope and staircase paths [91], corridor environments with both straight and loop trajectories [29], [99], office settings combining straight paths with staircases [101], and corridor routes integrating stairs with turning segments [40], [102] have collectively demonstrated algorithmic adaptability to vertical displacement and architectural complexity through diverse error measures.

The box plots of ATE are shown in Figure 22. Although the average errors in 2D and 3D environments are relatively similar, the error variance is noticeably greater in 2D environments. This difference is closely related to the disparity in path lengths between the two settings: the mean path length in 2D environments is substantially longer (2823.34 m) than in 3D environments (109.29 m). Longer trajectories in 2D lead to increased accumulation of inertial errors and more diverse motion patterns, which in turn result in lower stability and higher variability in navigation performance. In contrast, the shorter paths typically observed in 3D environments limit error growth and contribute to more consistent performance.

G. Result summary

This review provides a comprehensive analysis of the key factors that influence the performance of wearable IMU based positioning systems (see Table 3). Prior studies show that system accuracy and robustness are not determined by a single factor. Instead, they result from the combined effects of IMU configuration, sensor placement on the body, multi-sensor fusion strategies, positioning algorithms, and the test environment. By reviewing and comparing these factors, we reveal the trade-offs among them and clarify their applicable boundaries.

Regarding IMU types, the choice of IMU degrees of freedom forms the foundation of system performance. The 6 DoF IMU is the most widely used option (57.1 %) due to its low cost, low computational load, and resistance to magnetic interference. It can achieve sub-meter accuracy in simple indoor settings. However, because it lacks an absolute heading reference, yaw drift accumulates over time, causing the average error to increase to 1.80 m in long-distance or unstructured environments. Adding a magnetometer to form a 9 DoF system provides heading information and reduces the average error by about 57 % to 0.77 m, especially in stable magnetic environments. But its performance depends heavily on magnetic conditions, and the hardware and calibration cost are higher. Systems that also include a barometer show clear advantages for tasks with significant vertical motion, such as climbing stairs, reducing the average error to 0.48 m. This highlights the strong link between sensor configuration and task requirements.

The placement of sensors on the body directly affects signal quality and system performance. Existing studies focus mainly on the hands (35.5 %) and feet (29.9 %), which show strong motion patterns. A clear conclusion emerges from the comparison: combining sensors from multiple body locations gives much better results than using a single location. upper body (0.64 m) and whole body (0.75 m) setups achieve higher accuracy and stability by using complementary information. In contrast, single-location settings show larger errors. Hand-mounted sensors perform worst (1.60 m) because daily hand activities introduce strong noise. Foot, lower body, and head placements show moderate errors. These findings show that using sensors placed at several anatomical locations is an effective way to reduce local motion disturbances and improve navigation robustness.

To suppress drift in pure inertial navigation, multi-sensor fusion has become the main strategy for performance improvement. Although pure IMU methods remain the majority (59.5 %) due to their simplicity, integrating additional sensing modalities leads to clear accuracy gains. IMU and UWB fusion offers the best and most stable performance because UWB provides accurate distance measurements. IMU and RGB-D fusion also reduces drift by adding visual constraints. Fusion with WiFi or BLE depends strongly on wireless signal quality and thus shows larger performance variation. These results confirm that the effectiveness of fusion depends on the reliability and accuracy of the auxiliary sensors in the target environment.

At the algorithm level, current research shows a preference for mature and deployable methods. IMU-based algorithms with techniques such as zero-velocity updates, together with classical stochastic estimation frameworks like Kalman fil-

TABLE 3. Performance parameters and best settings for drift performance in different configurations.

Parameters	High drift performance	Medium drift performance	Low drift performance	Best Setting
IMU configuration	6 DoF	9 DoF	6 / 9 DoF + barometer	6 / 9 DoF + barometer
Sensor placement	Head Only / Lower Body	Hand Only / Upper Body	Foot Only / Whole Body	Foot Only
Sensor fusion	IMU Only	IMU + WiFi / BLE	IMU + UWB / RGB-D	IMU + RGB-D
Algorithm complexity	IMU based algorithm / ML based algorithm	Classical Stochastic Estimation Frameworks	Multi-sensor based algorithm	Multi-sensor based algorithm
Test environment richness	2D environment	—	3D environment	3D environments

tering, are the most common choices. They offer a solid theoretical basis and good computational efficiency, and they achieve similar positioning performance. Although multi-sensor fusion algorithms can pursue higher accuracy by combining information, they also increase system complexity. ML-based methods achieve the lowest RPE of 0.35%, outperforming CSEF (0.69%), multi-sensor fusion (1.00%), and IMU-based methods (1.22%). This discrepancy arises because ML-based studies tend to be evaluated over considerably longer trajectories, during which absolute error naturally accumulates, whereas their per-unit-distance drift rate is relatively well controlled. These findings suggest that the effectiveness of ML-based approaches may have been underestimated by conventional ATE-based comparisons, and that further work is needed to improve their generalisation and computational efficiency for real-world deployment.

Test environments also have an important impact on performance evaluation. Comparing 2D planar environments with 3D environments involving vertical movement shows that the average errors of the two are similar, but error variation is much larger in 2D tests. This is partly because there are more studies on 2D scenarios, and partly because planar environments involve more diverse pedestrian behaviours such as frequent turns, stops, and irregular hand motions which pose additional challenges for inertial navigation and make the results less stable.

In summary, designing wearable inertial positioning systems requires careful balancing of performance, cost, system complexity, and environmental adaptability. In indoor areas with strong magnetic disturbances, 6 DoF systems remain a practical choice. In stable magnetic environments where heading accuracy is important, 9 DoF systems perform better. For multi-floor navigation, barometer fusion should be considered. For optimal performance, sensors should be placed at multiple body locations, and IMU fusion with UWB or IMU fusion with RGB-D fusion should be prioritised. Algorithm-wise, hybrid approaches combining IMU methods with classical estimation frameworks are currently the most practical. Future research should test these techniques in more dynamic and realistic environments and improve the efficiency and robustness of data-driven methods to support broader real-world deployment.

IV. Conclusion

This paper presents a comprehensive and systematic review of wearable inertial navigation systems for indoor positioning, analysing over 120 recent studies through a novel dual-classification framework that examines the field from two dimensions: sensor type and positioning algorithm. We introduce a unified taxonomy that categorises existing systems according to their positioning algorithms, identifying four principal categories: purely IMU-based algorithms, CSEF, Multi sensor fusion approaches, and ML based positioning methods. We further establish a comprehensive categorisation scheme for wearable device configurations based on both body-worn location and sensing modality, distinguishing six body placement categories and five sensor combination types. A detailed comparison table encompassing sensor placement, model and origin, trajectory characteristics, positioning algorithms, and performance metrics has been compiled, with missing information manually extracted where necessary to enable complete cross-study comparison.

Our systematic analysis reveals several important findings. IMU-only systems account for 59.5% of all reported implementations, reflecting their fundamental role in wearable navigation due to their low cost and hardware simplicity; however, their accuracy is often limited by error accumulation. In contrast, multi-sensor fusion approaches that integrate external sensors such as cameras, WiFi, Bluetooth, or UWB effectively reduce drift by providing absolute position references or environmental features, thereby achieving higher accuracy and robustness in complex indoor environments. Specifically, IMU + UWB systems achieve average errors as low as 0.31 m, IMU + RGB systems reach 0.41 m, and IMU + WiFi systems attain 1.19 m, compared with 1.92 m for pure IMU systems. Sensor placement on the body also exerts a major influence on navigation accuracy. Multi-location configurations significantly outperform single-location deployments by exploiting the complementary motion patterns of different body parts:

upper body systems achieve 0.64 m average error and whole-body configurations reach 0.75 m, whilst foot-only, hand-only, lower-body, and head-mounted systems exhibit errors ranging from 1.25 m to 1.60 m.

Algorithmically, CSEF algorithms such as Kalman filters and particle filters remain foundational because of their mature theory and computational efficiency, whilst machine learning-based methods show strong potential in error modelling and trajectory prediction. When evaluated using RPE to account for differences in trajectory length, ML-based methods achieve the best performance (0.35% average RPE), compared with CSEF (0.69%), Multi sensor fusion (1.00%), and IMU based methods (1.22%), indicating that per-unit-distance error accumulation is in fact better controlled by learned models. Nevertheless, ML performance remains constrained by the quality and size of training data, as well as by computational complexity in real-time applications.

Despite significant progress, several fundamental challenges continue to constrain advancement. Error accumulation through integration of inertial measurements remains the primary limitation, necessitating external corrections through sensor fusion or periodic re-initialisation. Environmental interference affects external sensors used for drift correction, with signal attenuation, multipath effects, and magnetic disturbances reducing reliability in complex indoor environments. The field also lacks unified performance evaluation metrics and benchmarking protocols, with studies reporting results using diverse error measures and testing environments that complicate cross-study comparison. Machine learning approaches are hampered by limited availability of large-scale, high-quality training datasets with accurate ground truth, whilst real time operation on resource-limited wearable devices restricts algorithmic complexity.

Several important areas require further research. Developing hybrid systems that combine traditional filtering methods with machine learning could improve accuracy whilst maintaining reliability. The RPE analysis presented in this review demonstrates that ML-based methods already achieve superior per-distance drift control; hybrid architectures that combine this strength with the absolute accuracy and computational efficiency of classical frameworks represent a particularly promising direction. Creating adaptive algorithms that adjust to changing conditions and user behaviour represents a key research direction. Finally, establishing standardised benchmarks with shared datasets incorporating both ATE and RPE as complementary metrics would help advance the field and enable fair comparison between different approaches.

In summary, by focusing on hybrid modelling, environmental adaptability, algorithm simplification, and multimodal sensor integration, future research can significantly enhance the accuracy, robustness, and scalability of wearable inertial navigation systems, accelerating their adoption across diverse applications such as daily life navigation, professional tracking, and human computer interaction.

REFERENCES

[1] D. Engelsman and I. Klein, "Information-aided inertial navigation: A review," *IEEE Transactions on Instrumentation and Measurement*, vol. 72, pp. 1–18, 2023.

[2] X. Feng, K. A. Nguyen, and Z. Luo, "Wifi access points line-of-sight detection for indoor positioning using the signal round trip time," *Remote Sensing*, vol. 14, no. 23, p. 6052, 2022.

[3] K. A. Nguyen, Z. Luo, G. Li, and C. Watkins, "A review of smartphones-based indoor positioning: Challenges and applications," *IET Cyber-Systems and Robotics*, vol. 3, no. 1, pp. 1–30, 2021.

[4] J. Chen, B. Zhou, S. Bao, X. Liu, Z. Gu, L. Li, Y. Zhao, J. Zhu, and Q. Li, "A data-driven inertial navigation/bluetooth fusion algorithm for indoor localization," *IEEE Sensors Journal*, vol. 22, no. 6, pp. 5288–5301, 2022.

[5] Y. You and C. Wu, "Hybrid indoor positioning system for pedestrians with swinging arms based on smartphone imu and rssi of ble," *IEEE Transactions on Instrumentation and Measurement*, vol. 70, pp. 1–15, 2021.

[6] G. Zizzo and L. Ren, "Position tracking during human walking using an integrated wearable sensing system," *Sensors*, vol. 17, no. 12, p. 2866, 2017.

[7] D. Feng, C. Wang, C. He, Y. Zhuang, and X.-G. Xia, "Kalman-filter-based integration of imu and uwb for high-accuracy indoor positioning and navigation," *IEEE Internet of Things Journal*, vol. 7, no. 4, pp. 3133–3146, 2020.

[8] X. Feng, K. A. Nguyen, and Z. Luo, "An analysis of the properties and the performance of wifi rtt for indoor positioning in non-line-of-sight environments," in *17th International Conference on Location Based Services*, 2022.

[9] P. Zhao, H. Zhang, G. Liu, X. Cui, and M. Lu, "A uwb-aoa/imu integrated navigation system for 6-dof indoor uav localization," *Drones*, vol. 9, no. 8, p. 546, 2025.

[10] L. Li, D. Zhao, and Y. Xia, "Indoor positioning systems based on a modified matrix-weighted fusion estimator with multipath and nlos mitigation," *IEEE Internet of Things Journal*, vol. 11, no. 24, pp. 40041–40050, 2024.

[11] S. Shin, Z. Li, and E. Halilaj, "Markerless motion tracking with noisy video and imu data," *IEEE Transactions on Biomedical Engineering*, vol. 70, no. 11, pp. 3082–3092, 2023.

[12] H. Zhang and C. Ye, "A visual positioning system for indoor blind navigation," in *2020 IEEE International Conference on Robotics and Automation (ICRA)*, pp. 9079–9085, IEEE, 2020.

[13] N. Hajati and A. Rezaeizadeh, "A wearable pedestrian localization and gait identification system using kalman filtered inertial data," *IEEE Transactions on Instrumentation and Measurement*, vol. 70, pp. 1–8, 2021.

[14] E. M. Diaz, S. Kaiser, and D. B. Ahmed, "Height error correction for shoe-mounted inertial sensors exploiting foot dynamics," *Sensors (Basel, Switzerland)*, vol. 18, no. 3, p. 888, 2018.

[15] X. Feng, K. A. Nguyen, and Z. Luo, "A survey of deep learning approaches for wifi-based indoor positioning," *Journal of Information and Telecommunication*, vol. 6, no. 2, pp. 163–216, 2022.

[16] A. M. Hasan, K. Samsudin, A. R. Ramli, R. Azmir, and S. Ismaeel, "A review of navigation systems (integration and algorithms)," *Australian journal of basic and applied sciences*, vol. 3, no. 2, pp. 943–959, 2009.

[17] P. S. Farahsari, A. Farahzadi, J. Rezazadeh, and A. Bagheri, "A survey on indoor positioning systems for iot-based applications," *IEEE Internet of Things Journal*, vol. 9, no. 10, pp. 7680–7699, 2022.

[18] G. G. Samatas and T. P. Pachidis, "Inertial measurement units (imus) in mobile robots over the last five years: A review," *Designs*, vol. 6, no. 1, p. 17, 2022.

[19] A. M. Sabatini, "Estimating three-dimensional orientation of human body parts by inertial/magnetic sensing," *Sensors*, vol. 11, no. 2, pp. 1489–1525, 2011.

[20] C. Gentner, R. Pöhlmann, M. Ulmschneider, T. Jost, and S. Zhang, "Positioning using terrestrial multipath signals and inertial sensors," *Mobile Information Systems*, vol. 2017, no. 1, p. 9170746, 2017.

[21] K. A. Nguyen and Z. Luo, "Reliable indoor location prediction using conformal prediction," *Annals of Mathematics and Artificial Intelligence*, vol. 74, no. 1, pp. 133–153, 2015.

[22] R. Gravina and G. Fortino, "Wearable body sensor networks: state-of-the-art and research directions," *IEEE Sensors Journal*, vol. 21, no. 11, pp. 12511–12522, 2020.

[23] D. Moher, A. Liberati, J. Tetzlaff, D. G. Altman, P. Group, *et al.*, "Preferred reporting items for systematic reviews and meta-analyses: the prisma statement," *International journal of surgery*, vol. 8, no. 5, pp. 336–341, 2010.

[24] K. A. Nguyen, Y. Wang, G. Li, Z. Luo, and C. Watkins, "Realtime tracking of passengers on the london underground transport by matching smartphone accelerometer footprints," *Sensors*, vol. 19, no. 19, p. 4184, 2019.

[25] I. Patel, M. Kulkarni, and N. Mehendale, "Review of sensor-driven assistive device technologies for enhancing navigation for the visually impaired," *Multimedia Tools and Applications*, vol. 83, no. 17, pp. 52171–52195, 2024.

[26] K. A. Nguyen and Z. Luo, "On assessing the positioning accuracy of google tango in challenging indoor environments," in *2017 international conference on indoor positioning and indoor navigation (IPIN)*, pp. 1–8, IEEE, 2017.

[27] M. H. Abidi, A. N. Siddiquee, H. Alkhalefah, and V. Srivastava, "A comprehensive review of navigation systems for visually impaired individuals," *Heliyon*, vol. 10, no. 11, 2024.

[28] S. A. Maghdid, H. S. Maghdid, S. R. HmaSalah, K. Z. Ghafoor, A. S. Sadiq, and S. Khan, "Indoor human tracking mechanism using integrated onboard smartphones wi-fi device and inertial sensors," *Telecommunication Systems*, vol. 71, no. 3, pp. 447–458, 2019.

[29] T. D. Vy, T. L. N. Nguyen, and Y. Shin, "Pedestrian indoor localization and tracking using hybrid wi-fi/pdr for iphones," in *2021 IEEE 93rd Vehicular Technology Conference (VTC2021-Spring)*, pp. 1–7, IEEE, 2021.

[30] A. Poulose and D. S. Han, "Indoor localization using pdr with wi-fi weighted path loss algorithm," in *2019 International Conference on Information and Communication Technology Convergence (ICTC)*, pp. 689–693, IEEE, 2019.

[31] M. Sun, Y. Wang, S. Xu, H. Qi, and X. Hu, "Indoor positioning tightly coupled wi-fi ftm ranging and pdr based on the extended kalman filter for smartphones," *IEEE Access*, vol. 8, pp. 49671–49684, 2020.

[32] X. Wang, Y. Zhuang, Z. Zhang, X. Cao, F. Qin, X. Yang, X. Sun, M. Shi, and Z. Wang, "Tightly coupled integration of pedestrian dead reckoning and bluetooth based on filter and optimizer," *IEEE Internet of Things Journal*, vol. 10, no. 8, pp. 7327–7342, 2023.

[33] X. Feng, K. A. Nguyen, and Z. Luo, "A survey on data augmentation for wifi fingerprinting indoor positioning," *IEEE Sensors Reviews*, 2025.

[34] F. Ye, R. Chen, G. Guo, X. Peng, Z. Liu, and L. Huang, "A low-cost single-anchor solution for indoor positioning using ble and inertial sensor data," *IEEE Access*, vol. 7, pp. 162439–162453, 2019.

[35] X. Feng, K. A. Nguyen, and Z. Luo, "A review of open access wifi fingerprinting datasets for indoor positioning," *IEEE Access*, 2024.

[36] Y. Kiarashi, C. Hedge, V. S. K. Madala, A. Nakum, R. Singh, R. Tweedy, G. D. Clifford, and H. Kwon, "Indoor localization using bluetooth and inertial motion sensors in distributed edge and cloud computing environment." prepublished, 2023.

[37] X. Feng, K. A. Nguyen, and Z. Luo, "A wi-fi rss-rtt indoor positioning model based on dynamic model switching algorithm," *IEEE Journal of Indoor and Seamless Positioning and Navigation*, vol. 2, pp. 151–165, 2024.

[38] K. Nguyen and Z. Luo, "Evaluation of bluetooth properties for indoor localisation," in *Progress in Location-Based Services*, pp. 127–149, Springer, 2013.

[39] M. Wang, L. Li, J. Liu, and R. Chen, "Neural network aided factor graph optimization for collaborative pedestrian navigation," *IEEE Transactions on Intelligent Transportation Systems*, vol. 25, no. 1, pp. 303–314, 2024.

[40] F. Jiang, D. Caruso, A. Dhekne, Q. Qu, J. J. Engel, and J. Dong, "Robust indoor localization with ranging-imu fusion," in *2024 IEEE International Conference on Robotics and Automation (ICRA)*, pp. 11963–11969, IEEE, 2024.

[41] K. A. Nguyen, Z. Luo, and C. Watkins, "Epidemic contact tracing with smartphone sensors," *Journal of Location Based Services*, vol. 14, no. 2, pp. 92–128, 2020.

[42] S. Karam, V. Lehtola, and G. Vosselman, "Simple loop closing for continuous 6dof lidar&imu graph slam with planar features for indoor environments," *ISPRS Journal of Photogrammetry and Remote Sensing*, vol. 181, pp. 413–426, 2021.

[43] H. Weinberg, "Using the adxl202 in pedometer and personal navigation applications," *Analog Devices AN-602 application note*, vol. 2, no. 2, pp. 1–6, 2002.

[44] K. A. Nguyen, C. Watkins, and Z. Luo, "Co-location epidemic tracking on london public transports using low power mobile magnetometer," in *2017 International Conference on Indoor Positioning and Indoor Navigation (IPIN)*, pp. 1–8, IEEE, 2017.

[45] D. B. Ahmed, E. M. Diaz, and J. A. Conejo Minguez, "Exploiting wearable devices for the calibration of inertial navigation systems," in *2017 International Conference on Indoor Positioning and Indoor Navigation (IPIN)*, pp. 1–5, IEEE, 2017.

[46] O. S. Eyobu, A. Poulose, and D. S. Han, "An accuracy generalization benchmark for wireless indoor localization based on imu sensor data," in *2018 IEEE 8th International Conference on Consumer Electronics - Berlin (ICCE-Berlin)*, pp. 1–3, 2018.

[47] K. A. Nguyen, "A performance guaranteed indoor positioning system using conformal prediction and the wifi signal strength," *Journal of Information and Telecommunication*, vol. 1, no. 1, pp. 41–65, 2017.

[48] D. Yan, C. Shi, and T. Li, "An improved pdr system with accurate heading and step length estimation using handheld smartphone," *The Journal of Navigation*, vol. 75, no. 1, pp. 141–159, 2022.

[49] K. A. Nguyen, R. N. Akram, K. Markantonakis, Z. Luo, and C. Watkins, "Location tracking using smartphone accelerometer and magnetometer traces," in *Proceedings of the 14th International Conference on Availability, Reliability and Security*, pp. 1–9, 2019.

[50] Z. Tian, Y. Zhang, M. Zhou, and Y. Liu, "Pedestrian dead reckoning for marg navigation using a smartphone," *EURASIP Journal on Advances in Signal Processing*, vol. 2014, no. 1, p. 65, 2014.

[51] I. Skog, P. Handel, J.-O. Nilsson, and J. Rantakokko, "Zero-velocity detectionan algorithm evaluation," *IEEE transactions on biomedical engineering*, vol. 57, no. 11, pp. 2657–2666, 2010.

[52] R. Collinson, "Navigation systems," in *Introduction to Avionics Systems*, pp. 193–236, Springer, 2023.

[53] S. Zhang, H. Gao, and F. Yang, "Research on wearable devices for pedestrian navigation based on the informer model zero-velocity update architecture," *Sensors*, vol. 25, no. 8, p. 2587, 2025.

[54] H. Lan, C. Yu, Y. Li, Y. Zhuang, and N. El-Sheimy, "An efficient method for evaluating the performance of integrated multiple pedestrian navigation systems," in *2015 International Conference on Indoor Positioning and Indoor Navigation (IPIN)*, pp. 1–6, IEEE, 2015.

[55] Y. Wang, H. Cheng, and M. Q.-H. Meng, "Pedestrian motion tracking by using inertial sensors on the smartphone," in *2020 IEEE/RSJ International Conference on Intelligent Robots and Systems (IROS)*, pp. 4426–4431, IEEE, 2020.

[56] Y. Ren, D. Zhu, K. Tong, L. Xv, Z. Wang, L. Kang, and J. Chai, "Pdc-har: Human activity recognition via multi-sensor wearable networks using two-channel convolutional neural networks," *Pervasive and Mobile Computing*, vol. 97, p. 101868, 2024.

[57] E. Foxlin and L. Naimark, "Vis-tracker: A wearable vision-inertial self-tracker," in *IEEE Virtual Reality, 2003. Proceedings.*, pp. 199–206, IEEE Comput. Soc, 2003.

[58] M. Faessler, F. Fontana, C. Forster, E. Mueggler, M. Pizzoli, and D. Scaramuzza, "Autonomous, vision-based flight and live dense 3d mapping with a quadrotor micro aerial vehicle," *Journal of Field Robotics*, vol. 33, no. 4, pp. 431–450, 2016.

[59] A. I. Mourikis and S. I. Roumeliotis, "A multi-state constraint kalman filter for vision-aided inertial navigation," in *Proceedings 2007 IEEE international conference on robotics and automation*, pp. 3565–3572, IEEE, 2007.

[60] S. Leutenegger, S. Lynen, M. Bosse, R. Siegwart, and P. Furgale, "Keyframe-based visual–inertial odometry using nonlinear optimization," *The International Journal of Robotics Research*, vol. 34, no. 3, pp. 314–334, 2015.

[61] Y. Wang, H. Cheng, A. Zhang, and M. Q.-H. Meng, "From imu measurement sequence to velocity estimate sequence: An effective and efficient data-driven inertial odometry approach," *IEEE Sensors Journal*, vol. 23, no. 15, pp. 17117–17126, 2023.

[62] C.-S. Jao, D. Wang, and A. M. Shkel, "Prio-imu: Prioritizable imu array for enhancing foot-mounted inertial navigation accuracy," in *2023 IEEE International Symposium on Inertial Sensors and Systems (INERTIAL)*, pp. 1–4, IEEE, 2023.

[63] H. Xu, F. Meng, H. Liu, H. Shao, and L. Sun, "An adaptive multisource data fusion indoor positioning method based on collaborative wi-fi fingerprinting and pdr techniques," *IEEE Sensors Journal*, vol. 24, no. 19, pp. 31481–31494, 2024.

[64] Y. Wang, H. Cheng, and M. Q.-H. Meng, "A2dio: Attention-driven deep inertial odometry for pedestrian localization based on 6d imu," in *2022 International Conference on Robotics and Automation (ICRA)*, pp. 819–825, IEEE, 2022.

[65] H. Yan, Q. Shan, and Y. Furukawa, "Ridi: Robust imu double integration," in *Computer Vision ECCV 2018* (V. Ferrari, M. Hebert, C. Sminchisescu, and Y. Weiss, eds.), vol. 11217, pp. 641–656, Springer International Publishing, 2018.

[66] S. Yang, L. Xing, W. Liu, W. Qian, W. Qian, H. Xue, and Y. Zhu, "Robust navigation method for wearable humanmachine interaction system based on deep learning," *IEEE Sensors Journal*, vol. 20, no. 24, pp. 14950–14957, 2020.

[67] A. Kumar, S. Pundlik, E. Peli, and G. Luo, "Comparison of visual slam and imu in tracking head movement outdoors," *Behavior Research Methods*, vol. 55, no. 6, pp. 2787–2799, 2022.

[68] D. B. Ahmed, L. E. Diez Blanco, and E. M. Diaz, "Performance comparison of wearable-based pedestrian navigation systems in large areas," in *2017 International Conference on Indoor Positioning and Indoor Navigation (IPIN)*, pp. 1–7, IEEE, 2017.

[69] D. Bousdar Ahmed and E. Munoz Diaz, "Loose coupling of wearable-based inss with automatic heading evaluation," *Sensors*, vol. 17, no. 11, p. 2534, 2017.

[70] D. G. Kottas and S. I. Roumeliotis, "An iterative kalman smoother for robust 3d localization on mobile and wearable devices," in *2015 IEEE International Conference on Robotics and Automation (ICRA)*, pp. 6336–6343, IEEE, 2015.

[71] J. Justa, V. mdl, and A. Hamek, "Deep learning methods for speed estimation of bipedal motion from wearable imu sensors," *Sensors*, vol. 22, no. 10, p. 3865, 2022.

[72] C. Li, Z. Su, C.-y. Fei, Q. Li, and L.-q. Zhang, "On a novel combination method for pedestrian multi-attitude solution with the wearable mems-imu," in *2017 36th Chinese Control Conference (CCC)*, pp. 5734–5740, 2017.

[73] X. Niu, T. Liu, J. Kuang, and Y. Li, "A novel position and orientation system for pedestrian indoor mobile mapping system," *IEEE Sensors Journal*, vol. 21, no. 2, pp. 2104–2114, 2021.

[74] Y.-L. Hsu, Y.-J. Chen, and S.-W. Shih, "A particle filter approach for pedestrian dead reckoning using wearable sensors," in *2016 10th International Conference on Innovative Mobile and Internet Services in Ubiquitous Computing (IMIS)*, pp. 26–32, IEEE, 2016.

[75] Y. C. Lai, C. C. Chang, C. M. Tsai, S. Y. Lin, and S. C. Huang, "Development of a pedestrian indoor navigation system based on multi-sensor fusion and fuzzy logic estimation algorithms," *The International Archives of the Photogrammetry, Remote Sensing and Spatial Information Sciences*, vol. XL-4/W5, pp. 81–86, 2015.

[76] X. Zhang, B. Li, S. L. Joseph, J. Xiao, Y. Sun, Y. Tian, J. P. Munoz, and C. Yi, "A slam based semantic indoor navigation system for visually impaired users," in *2015 IEEE International Conference on Systems, Man, and Cybernetics*, pp. 1458–1463, IEEE, 2015.

[77] H. Jia, B. Yu, H. Li, S. Pan, J. Li, X. Wang, and L. Huang, "The improved method for indoor 3d pedestrian positioning based on dual foot-mounted imu system," *Micromachines*, vol. 14, no. 12, p. 2192, 2023.

[78] J. Borenstein, L. Ojeda, and S. Kwanmuang, "Heuristic reduction of gyro drift in imu-based personnel tracking systems," in *Optics and Photonics in Global Homeland Security V and Biometric Technology for Human Identification VI* (C. S. Halvorson, . O. Southern, B. V. K. Vijaya Kumar, S. Prabhakar, and A. A. Ross, eds.), p. 73061H, 2009.

[79] J. Kuang, D. Xia, Y. Wang, X. Meng, and X. Niu, "A shin-mounted inertial navigation system for pedestrian walking and running gait," *IEEE Sensors Journal*, vol. 25, no. 6, pp. 9449–9458, 2025.

[80] A. Norrdine, Z. Kasmi, and J. Blankenbach, "Step detection for zupt-aided inertial pedestrian navigation system using foot-mounted permanent magnet," *IEEE Sensors Journal*, vol. 16, no. 17, pp. 6766–6773, 2016.

[81] L. Van Nguyen and H. M. La, "Real-time human foot motion localization algorithm with dynamic speed," *IEEE Transactions on Human-Machine Systems*, vol. 46, no. 6, pp. 822–833, 2016.

[82] S. Zihajehzadeh, Tien Jung Lee, Jung Keun Lee, R. Hoskinson, and E. J. Park, "Integration of mems inertial and pressure sensors for vertical trajectory determination," *IEEE Transactions on Instrumentation and Measurement*, vol. 64, no. 3, pp. 804–814, 2015.

[83] J. Li, X. Liu, Z. Wang, H. Zhao, T. Zhang, S. Qiu, X. Zhou, H. Cai, R. Ni, and A. Cangelosi, "Real-time human motion capture based on wearable inertial sensor networks," *IEEE Internet of Things Journal*, vol. 9, no. 11, pp. 8953–8966, 2022.

[84] Y. Suzuki, M. E. Hahn, and Y. Enomoto, "Estimation of foot trajectory and stride length during level ground running using foot-mounted inertial measurement units," *Sensors*, vol. 22, no. 19, p. 7129, 2022.

[85] X. Hou and J. Bergmann, "Hinnet + headslam: Robust inertial navigation with machine learning for long-term stable tracking," *IEEE Sensors Letters*, vol. 7, no. 8, pp. 1–4, 2023.

[86] H. Li, H. Liu, Z. Li, C. Li, Z. Meng, N. Gao, and Z. Zhang, "Adaptive threshold-based zupt for single imu-enabled wearable pedestrian localization," *IEEE Internet of Things Journal*, vol. 10, no. 13, pp. 11749–11760, 2023.

[87] L. Zhang, Y. Liu, and J. Sun, "A hybrid framework for mitigating heading drift for a wearable pedestrian navigation system through adaptive fusion of inertial and magnetic measurements," *Applied Sciences*, vol. 11, no. 4, p. 1902, 2021.

[88] G. Zizzo and L. Ren, "Position tracking during human motions using an integrated wearable sensing system," *Sensors*, vol. 17, no. 12, p. 2866, 2017.

[89] J. Windau and L. Itti, "Walking compass with head-mounted imu sensor," in *2016 IEEE International Conference on Robotics and Automation (ICRA)*, pp. 5542–5547, IEEE, 2016.

[90] Y. Wang, K. H. Fehr, and P. G. Adamczyk, "Impact-aware foot motion reconstruction and ramp/stair detection using one foot-mounted inertial measurement unit," *Sensors*, vol. 24, no. 5, p. 1480, 2024.

[91] J. Wang, X. Xu, Z. Yu, Z. Li, and S. Liu, "A novel suppression method of height drift for pedestrian navigation with a circular hypotheses on terrain slope," *IEEE Sensors Journal*, vol. 22, no. 12, pp. 12054–12063, 2022.

[92] M. Ren, K. Pan, Y. Liu, H. Guo, X. Zhang, and P. Wang, "A novel pedestrian navigation algorithm for a foot-mounted inertial-sensor-based system," *Sensors*, vol. 16, no. 1, p. 139, 2016.

[93] J.-O. Nilsson, I. Skog, and P. Handel, "Performance characterisation of foot-mounted zupt-aided inss and other related systems," in *2010 International Conference on Indoor Positioning and Indoor Navigation*, pp. 1–7, IEEE, 2010.

[94] L.-F. Shi, Y.-J. Dong, and Y. Shi, "Indoor pdr method based on foot-mounted low-cost immu," in *2022 IEEE International Conference on Networking, Sensing and Control (ICNSC)*, pp. 1–6, IEEE, 2022.

[95] A. Ahuja, A. Ferlini, and C. Mascolo, "Pilotear: Enabling in-ear inertial navigation," in *Adjunct Proceedings of the 2021 ACM International Joint Conference on Pervasive and Ubiquitous Computing and Proceedings of the 2021 ACM International Symposium on Wearable Computers*, pp. 139–145, ACM, 2021.

[96] M. Angermann, P. Robertson, T. Kemptner, and M. Khider, "A high precision reference data set for pedestrian navigation using foot-mounted inertial sensors," in *2010 International Conference on Indoor Positioning and Indoor Navigation*, pp. 1–6, IEEE, 2010.

[97] S. Godha and G. Lachapelle, "Foot mounted inertial system for pedestrian navigation," *Measurement Science and Technology*, vol. 19, no. 7, p. 075202, 2008.

[98] Z. Zhou, S. Yang, Z. Ni, W. Qian, C. Gu, and Z. Cao, "Pedestrian navigation method based on machine learning and gait feature assistance," *Sensors*, vol. 20, no. 5, p. 1530, 2020.

[99] Z. Wang, Z. Xiong, C. Shi, Q. Liu, R. Liu, and M. Xu, "An improved method for multi-motion mode recognition and navigation optimization for indoor pedestrians," *Guidance, Navigation and Control*, vol. 05, no. 03, pp. 327–344, 2025.

[100] A. R. Jimnez, F. Seco, F. Zampella, J. C. Prieto, and J. Guevara, "Indoor localization of persons in aal scenarios using an inertial measurement unit (imu) and the signal strength (ss) from rfid tags," in *Evaluating AAL Systems Through Competitive Benchmarking* (S. Chessa and S. Knauth, eds.), vol. 362, pp. 32–51, Springer Berlin Heidelberg, 2013.

[101] Y. Li, Z. Meng, N. Gao, and Z. Zhang, "Heading angle correction with building map model constraint for single imu-based pedestrian wearable localization," *IEEE Sensors Letters*, vol. 9, no. 10, pp. 1–4, 2025.

[102] W. Zhang, X. Li, D. Wei, X. Ji, and H. Yuan, "A foot-mounted pdr system based on imu/ekf+hmm+zupt+zaru+hdr+compass algorithm,"

in *2017 International Conference on Indoor Positioning and Indoor Navigation (IPIN)*, pp. 1–5, IEEE, 2017.

[103] J. Kawecki, P. Oleksy, and L. Januszkiewicz, "Inertial sensors integrated with clothing to localize people inside buildings," *International Journal of Electronics and Telecommunications*, pp. 53–58, 2020.

[104] F. Lin, Q. Cai, Y. Liu, Y. Chen, J. Huang, and H. Peng, "Pedestrian dead reckoning method based on array imu," *IEEE Sensors Journal*, vol. 24, no. 22, pp. 37753–37763, 2024.

[105] Y. Wang, H. Cheng, and M. Q.-H. Meng, "Inertial odometry using hybrid neural network with temporal attention for pedestrian localization," *IEEE Transactions on Instrumentation and Measurement*, vol. 71, pp. 1–10, 2022.

[106] Y. Wang, H. Cheng, C. Wang, and M. Q.-H. Meng, "Pose-invariant inertial odometry for pedestrian localization," *IEEE Transactions on Instrumentation and Measurement*, vol. 70, pp. 1–12, 2021.

[107] Y. Wang, H. Cheng, and M. Q.-H. Meng, "Fdio: Extended kalman filter-aided deep inertial odometry," in *2023 International Conference on Advanced Robotics and Mechatronics (ICARM)*, pp. 482–487, IEEE, 2023.

[108] T. Yoshida, K. Urano, S. Aoki, T. Yonezawa, and N. Kawaguchi, "Rgnet: Robust gravity estimation neural network for imu-based localization using smartphone," in *2021 Thirteenth International Conference on Mobile Computing and Ubiquitous Network (ICMU)*, pp. 1–8, IEEE, 2021.

[109] B. Zeinali, H. Zanddizari, and M. J. Chang, "Imunet: Efficient regression architecture for inertial imu navigation and positioning," *IEEE Transactions on Instrumentation and Measurement*, vol. 73, pp. 1–13, 2024.

[110] S. Herath, H. Yan, and Y. Furukawa, "Ronin: Robust neural inertial navigation in the wild: Benchmark, evaluations, & new methods," in *2020 IEEE International Conference on Robotics and Automation (ICRA)*, pp. 3146–3152, IEEE, 2020.

[111] K. Eckenhoff, P. Geneva, and G. Huang, "Mimc-vins: A versatile and resilient multi-imu multi-camera visual-inertial navigation system," *IEEE Transactions on Robotics*, vol. 37, no. 5, pp. 1360–1380, 2021.

[112] J. Kuang, D. Xia, T. Liu, Q. Chen, and X. Niu, "Shin-ins: A shin-mounted imu-based inertial navigation system for pedestrian," *IEEE Sensors Journal*, vol. 23, no. 21, pp. 25760–25769, 2023.

[113] Y. Wang, S. Askari, and A. M. Shkel, "Study on mounting position of imu for better accuracy of zupt-aided pedestrian inertial navigation," in *2019 IEEE International Symposium on Inertial Sensors and Systems (INERTIAL)*, pp. 1–4, IEEE, 2019.

[114] Y. Wang, A. Chernyshoff, and A. M. Shkel, "Study on estimation errors in zupt-aided pedestrian inertial navigation due to imu noises," *IEEE Transactions on Aerospace and Electronic Systems*, vol. 56, no. 3, pp. 2280–2291, 2020.

[115] F. Montorsi, F. Pancaldi, and G. M. Vitetta, "Design and implementation of an inertial navigation system for pedestrians based on a low-cost mems imu," in *2013 IEEE International Conference on Communications Workshops (ICC)*, pp. 57–61, IEEE, 2013.

[116] Facultyof Science and Technology, Universiti Sains Islam Malaysia (USIM), Bandar Baru Nilai, Nilai 71800, Negeri Sembilan, Malaysia, K. Abdulrahim, C. Hide, T. Moore, C. Hill, and Nottingham Geospatial Institute, University of Nottingham, NG7 2RD, Nottingham, UK, "Increased error observability of an inertial pedestrian navigation system by rotating imu," *Journal of Engineering and Technological Sciences*, vol. 46, no. 2, pp. 211–225, 2014.

[117] N. Mostofi, M. Elhabiby, and N. El-Sheimy, "Indoor localization and mapping using camera and inertial measurement unit (imu)," in *2014 IEEE/ION Position, Location and Navigation Symposium - PLANS 2014*, pp. 1329–1335, IEEE, 2014.

[118] Y. Shen, Y. Yao, C. Yang, and X. Xu, "Enhanced pedestrian navigation with wearable imu: Forwardbackward navigation and rts smoothing techniques," *Technologies*, vol. 13, no. 7, p. 296, 2025.

[119] G. He, M. Liu, X. Li, H. Chang, W. Yuan, and G. Yuan, "Improving the position accuracy of the zupt-aided pedestrian inertial navigation by using a differential layout mimu array," *IEEE Sensors Journal*, vol. 23, no. 19, pp. 23420–23430, 2023.

[120] B. van Ingen, "Indoor localization through pedestrian dead reckoning and activity recognition," *repository.tudelft.nl*, 2020.

[121] Z. Li, X. Xu, J. Wang, and C. Zhang, "Prior kinematic information fusion for pedestrian localization with toe-heel-shank mimus," *IEEE Transactions on Industrial Electronics*, vol. 70, no. 7, pp. 7498–7506, 2023.

[122] D. Caruso, A. Eudes, M. Sanfourche, D. Vissiere, and G. Le Besnerais, "Robust indoor/outdoor navigation through magneto-visual-inertial optimization-based estimation," in *2017 IEEE/RSJ International Conference on Intelligent Robots and Systems (IROS)*, pp. 4402–4409, IEEE, 2017.

[123] E. Pissaloux, Y. Chen, and R. Velazquez, "Image matching optimization via vision and inertial data fusion: Application to navigation of the visually impaired," *International Journal of Image and Graphics*, vol. 10, no. 04, pp. 545–558, 2010.

[124] X. Yi, Y. Zhou, M. Habermann, V. Golyanik, S. Pan, C. Theobalt, and F. Xu, "Egolocate: Real-time motion capture, localization, and mapping with sparse body-mounted sensors," *ACM Transactions on Graphics*, vol. 42, no. 4, pp. 1–17, 2023.

[125] Z. Xu, J. Wei, J. Zhu, and W. Yang, "A robust floor localization method using inertial and barometer measurements," in *2017 International Conference on Indoor Positioning and Indoor Navigation (IPIN)*, pp. 1–8, IEEE, 2017.

[126] A. Poulose, O. S. Eyobu, and D. S. Han, "A combined pdr and wi-fi trilateration algorithm for indoor localization," in *2019 International Conference on Artificial Intelligence in Information and Communication (ICAIIC)*, pp. 072–077, IEEE, 2019.

[127] A. Poulose, O. S. Eyobu, and D. S. Han, "An indoor position-estimation algorithm using smartphone imu sensor data," *IEEE Access*, vol. 7, pp. 11165–11177, 2019.

[128] J.-W. Kim and Y. Shin, "Deep learning-based multi-floor indoor localization using smartphone imu sensors with 3d location initialization," *IEEE Access*, vol. 13, pp. 101532–101544, 2025.

[129] W. Liu, Y. Xu, Z. Yin, J. Liu, R. Gao, Z. Shi, K. Liang, and Y. Huang, "Robust error state fir filter and its application in pedestrian tracking," *IEEE Access*, vol. 12, pp. 154010–154021, 2024.

[130] A. Achroufene, S. Melchane, and F. Ameziane, "Footstep detection using dempster-shafer theory," in *2024 2nd International Conference on Electrical Engineering and Automatic Control (ICEEAC)*, pp. 1–6, IEEE, 2024.

[131] Y. Yao, Y. Liu, Z. Zhou, and X. Xu, "A magnetic interference detection-based fusion heading estimation method for pedestrian dead reckoning positioning," *IEEE Sensors Journal*, vol. 23, no. 1, pp. 677–688, 2023.

[132] M. Xuan, Z. Ping, L. Haodong, and D. Zhihong, "Research on pedestrian inertial navigation assisted by geomagnetic matching positioning," in *2022 China Automation Congress (CAC)*, pp. 3065–3070, IEEE, 2022.

[133] D. Yan, C. Shi, T. Li, and Y. Li, "Flexpdr: Fully flexible pedestrian dead reckoning using online multimode recognition and time-series decomposition," *IEEE Internet of Things Journal*, vol. 9, no. 16, pp. 15240–15254, 2022.

[134] K. Li, Q. Gong, Y. Ren, Y. Li, Y. Han, C. Pang, and H. Kong, "Magnetic field positioning technology of indoor sports bodies," *IEEE Sensors Journal*, vol. 22, no. 1, pp. 219–228, 2022.

[135] X. Liu, B. Zhou, P. Huang, W. Xue, Q. Li, J. Zhu, and L. Qiu, "Kalman filter-based data fusion of wi-fi rtt and pdr for indoor localization," *IEEE Sensors Journal*, vol. 21, no. 6, pp. 8479–8490, 2021.

[136] K. Muthineni, A. Artemenko, J. Vidal, M. Njar, M. Catalan, and J. Paradells, "Deep learning-based uwb-imu data fusion for indoor positioning in industrial scenario," *IEEE Open Journal of Vehicular Technology*, vol. 6, pp. 1209–1221, 2025.

[137] A. RajKumar, F. Vulpi, S. R. Bethi, H. K. Wazir, P. Raghavan, and V. Kapila, "Wearable inertial sensors for range of motion assessment," *IEEE Sensors Journal*, vol. 20, no. 7, pp. 3777–3787, 2020.

[138] T. Antonakopoulos and D. Sikeridis, "An imu-based wearable presentation pointing device," *IEICE Proceedings Series*, vol. 24, no. A4-2, 2016.

[139] X. Chen, K. Zhang, H. Liu, Y. Leng, and C. Fu, "A probability distribution model-based approach for foot placement prediction in the early swing phase with a wearable imu sensor," *IEEE Transactions on Neural Systems and Rehabilitation Engineering*, vol. 29, pp. 2595–2604, 2021.

[140] K. Sartipi, R. C. DuToit, C. B. Cobar, and S. I. Roumeliotis, "Decentralized visual-inertial localization and mapping on mobile devices for augmented reality," in *2019 IEEE/RSJ International Conference on Intelligent Robots and Systems (IROS)*, pp. 2145–2152, IEEE, 2019.

[141] H. Shoushtari, F. Kassawat, and H. Sternberg, "Context aware transformer network and in-situ imu calibration for accurate positioning,"

in *2024 14th International Conference on Indoor Positioning and Indoor Navigation (IPIN)*, pp. 1–6, IEEE, 2024.
[142] Z. Huang, S. Poslad, and F. Gu, "Eniloc: Efficient neural inertial localization," *Available at SSRN 4814692*, 2024.
[143] Y. Xiong, S. Li, K. Zhao, Y. Chen, Y. Zhang, and C. Dong, "A pedestrian heading online compensation method research for a waist-worn indoor inertial navigation system," in *2019 Chinese Control Conference (CCC)*, pp. 3821–3826, IEEE, 2019.
[144] H. Zhang, L. Jin, and C. Ye, "An rgb-d camera based visual positioning system for assistive navigation by a robotic navigation aid," *IEEE/CAA Journal of Automatica Sinica*, vol. 8, no. 8, pp. 1389–1400, 2021.
[145] K. Naheem and M. S. Kim, "A low-cost foot-placed uwb and imu fusion-based indoor pedestrian tracking system for iot applications," *Sensors*, vol. 22, no. 21, p. 8160, 2022.
[146] P. Zhou, H. Wang, R. Gravina, and F. Sun, "Wio-ekf: Extended kalman filtering-based wi-fi and inertial odometry fusion method for indoor localization," *IEEE Internet of Things Journal*, vol. 11, no. 13, pp. 23592–23603, 2024.
[147] M. Basso, M. Galanti, G. Innocenti, and D. Miceli, "Pedestrian dead reckoning based on frequency self-synchronization and body kinematics," *IEEE Sensors Journal*, vol. 17, no. 2, pp. 534–545, 2017.
[148] X. Hou and J. Bergmann, "Rocip: Robust continuous inertial position tracking for complex actions emerging from the interaction of human actors and environment," *Applied Intelligence*, vol. 55, no. 7, p. 494, 2025.
[149] O. Dyhdalovych, A. Yaroshevych, O. Kapshii, I. Kravets, and O. Farenyuk, "Particle filter-based ble and imu fusion algorithm for indoor localization," *Telecommunication Systems*, vol. 88, no. 1, p. 9, 2025.
[150] J. Dong, M. Noreikis, Y. Xiao, and A. Yla-Jaaski, "Vinav: A vision-based indoor navigation system for smartphones," *IEEE Transactions on Mobile Computing*, vol. 18, no. 6, pp. 1461–1475, 2019.
[151] K. Eckenhoff, P. Geneva, and G. Huang, "Sensor-failure-resilient multi-imu visual-inertial navigation," in *2019 International Conference on Robotics and Automation (ICRA)*, pp. 3542–3548, IEEE, 2019.
[152] M. Fan, J. Li, and W. Wang, "An imu/uwb tightly coupled navigation algorithm to improve positioning accuracy under large-scale nlos conditions," *Measurement Science and Technology*, vol. 36, no. 4, p. 045105, 2025.
[153] G. Qiu, J. Yuan, L. Zhao, and M. Jiang, "Asynchronous hybrid indoor positioning system based on inertial navigation and pseudo-miller-coding aided visible light positioning," in *2021 7th International Conference on Computer and Communications (ICCC)*, pp. 366–371, IEEE, 2021.
[154] D. Feng, J. Peng, Y. Zhuang, C. Guo, T. Zhang, Y. Chu, X. Zhou, and X.-G. Xia, "An adaptive imu/uwb fusion method for nlos indoor positioning and navigation," *IEEE Internet of Things Journal*, vol. 10, no. 13, pp. 11414–11428, 2023.
[155] K. Ghanizadegan and H. A. Hashim, "Deepukf-vin: Adaptively-tuned deep unscented kalman filter for 3d visual-inertial navigation based on imu-vision-net," *Expert Systems with Applications*, vol. 271, p. 126656, 2025.
[156] F. Yang, L. Gou, and X. Cai, "Pedestrian positioning scheme based on the fusion of smartphone imu sensors and commercially surveillance video," *IEEE Sensors Journal*, vol. 22, no. 5, pp. 4697–4708, 2022.
[157] J. Li, C. Xiu, D. Yang, and F. Wang, "A novel two-stage imu/mag-aided uwb fusion algorithm for pedestrian localization in underground space," *IEEE Transactions on Instrumentation and Measurement*, vol. 74, pp. 1–16, 2025.
[158] L. Cheng, J. Song, and W. Zhao, "A hybrid ekf/wufir filter for indoor localization integrating ins and uwb data," *IEEE Transactions on Network Science and Engineering*, vol. 12, no. 3, pp. 2266–2276, 2025.
[159] X. Zhou, L. Chen, Y. Chen, H. Yin, X. Chen, and W. Wang, "Fusion of imu and probabilistic model for indoor localization based on bayesian framework," *IEEE Internet of Things Journal*, vol. 12, no. 11, pp. 17080–17094, 2025.